HEPATIC LESION DETECTABILITY ON DUAL ENERGY COMPUTED TOMOGRAPHY

IMAGING: PHANTOM STUDY

Miss Hataipat Jantawong

A  Dissertation Submitted in Partial Fulfillment of the Requirements

for the Degree of Doctor of Philosophy in Medical Physics

Department of Radiology

FACULTY OF MEDICINE

Chulalongkorn University

Academic Year 2021

การค้นหารอยโรคในตับจากภาพเอกซเรย์คอมพิวเตอร์ที่มีสองพลังงาน : การศึกษาในหุ่นจำลอง

น.ส.หทัยภัทร จันทวงษ์

| Thesis Title | HEPATIC LESION DETECTABILITY ON DUAL ENERGY COMPUTED TOMOGRAPHY IMAGING: PHANTOM STUDY |
|---|---|
| By | Miss Hataipat Jantawong |
| Field of Study | Medical Physics |
| Thesis Advisor | Associate Professor ANCHALI KRISANACHINDA, Ph.D. |

Accepted by the FACULTY OF MEDICINE, Chulalongkorn University in Partial Fulfillment of the Requirement for the Doctor of Philosophy

............................................. Dean of the FACULTY OF MEDICINE

(Associate Professor CHANCHAI SITTIPUNT, M.D.)

DISSERTATION COMMITTEE

............................................. Chairman

(Assistant Professor YOTHIN RAKVONGTHAI, Ph.D.)

............................................. Thesis Advisor

(Associate Professor ANCHALI KRISANACHINDA, Ph.D.)

............................................. Examiner

(Assistant Professor KITIWAT KHAMWAN, Ph.D.)

............................................. Examiner

(Assistant Professor TAWEAP SANGHANGTHUM, Ph.D.)

............................................. External Examiner

(Professor Kosuke Matsubara, Ph.D.)

หทัยภัทร จันทวงษ์ : การค้นหารอยโรคในตับจากภาพเอกซเรย์คอมพิวเตอร์ที่มีสองพลังงาน : การศึกษาในหุ่นจำลอง. ( HEPATIC LESION DETECTABILITY ON DUAL ENERGY COMPUTED TOMOGRAPHY IMAGING: PHANTOM STUDY) อ.ที่ปรึกษาหลัก : รศ. ดร.อัญชลี กฤษณจินดา

วัตถุประสงค์ของการศึกษานี้ เพื่อตรวจสอบความสามารถในการค้นหารอยโรคในตับจากภาพเอกซเรย์คอมพิวเตอร์ที่มีสองพลังงานโดยเป็นการศึกษาในหุ่นจำลองส่วนช่องท้องที่มีขนาดต่างๆกัน นำไปถ่ายภาพเอกซเรย์คอมพิวเตอร์ที่มีสองพลังงาน (Dual Energy Computed Tomography : DECT) และเพื่อศึกษาปัจจัยที่มีผลต่อการค้นหารอยโรคในตับจากภาพเอกซเรย์คอมพิวเตอร์ที่มีสองพลังงาน การศึกษานี้ใช้หุ่นจำลองตับมนุษย์ ร่วมกับการใส่วงแหวนขยายเพื่อเป็นการจำลองผู้ป่วยที่มีขนาดเล็ก กลาง และใหญ่ หุ่นจำลองจะถูกสแกนด้วย DECT โดยใช้ค่า kV คู่ 3 ค่า ได้แก่ 80/-,90/- และ 100/Sn150-kV ข้อมูลภาพที่เป็นภาพเสมือนพลังงานเดียว ที่พลังงาน 40-,50-,60- และ 70-keV ถูกสร้างขึ้นจากชุดข้อมูล DECT และนำไปใช้ประเมินคุณภาพของภาพด้วยการใช้ตัวชี้วัดคุณภาพของภาพ ได้แก่ ความละเอียด (Task Transfer Function :TTF), สัญญาณรบกวนภาพ (Noise Power Spectrum : NPS) และดัชนีความสามารถในการตรวจจับรอยโรค (Detectability index : d') สำหรับการวินิจฉัยเพื่อตรวจหารอยโรคตับที่มีขนาดเส้นผ่านศูนย์กลาง 15 มม. ซึ่งเป็นงานทางคลินิกในการตรวจหามะเร็งตับ (HCC) จากภาพถ่าย CT การศึกษานี้ยังมีการประเมินความแม่นยำของการหาปริมาณความเข้มข้นของไอโอดีนด้วยการใช้ฟังก์ชั่นของ DECT ซึ่งทำโดยใช้หุ่นจำลองตับและรอยโรคที่ออกแบบและสร้างด้วยเครื่องพิมพ์ 3 มิติ ผลการวิจัยพบว่า ความละเอียด (TTF) เพิ่มขึ้นเมื่อเพิ่มระดับพลังงานของภาพเสมือนพลังงานเดียว (Virtual Monoenergetic Image : VMI) จาก 40-70 keV โดยค่าสูงสุดของ TTF 50% ($f_{50}$) พบที่ 70 keV VMI นอกจากนี้ยังพบว่าขนาดสัญญาณรบกวนภาพ (NPS) เพิ่มขึ้นเมื่อเพิ่มขนาดหุ่นจำลอง, ลดพลังงาน VMI หรือ เมื่อ kV บนหลอดเอกซ์เรย์ A เพิ่มขึ้น ขณะที่ผลลัพธ์ของ d' แสดงให้เห็นว่าเมื่อขนาด หุ่นจำลองเพิ่มขึ้นและลดระดับพลังงานลง ทำให้ d' ลดลง ในส่วนของการศึกษาเรื่องการวัดค่าไอโอดีน พบว่าความเข้มข้นของไอโอดีนที่วัดได้ด้วย DECT มีความสัมพันธ์สูงกับความเข้มข้นที่แท้จริง โดยมีเปอร์เซ็นต์ของข้อผิดพลาดในการวัดปริมาณไอโอดีนสำหรับความเข้มข้นที่ 2.0-5.0 มก.ไอโอดีน/ซีซี อยู่ภายในช่วง ±20% โดยสรุปกรณีหุ่นจำลองขนาดเล็ก การสร้างภาพที่ 70keV-VMI ที่แสกนจาก 80/Sn150 kV ให้ d' สูงสุด สำหรับหุ่นจำลองขนาดกลางและขนาดใหญ่ d' สูงสุดอยู่ที่ ภาพ 70keV-VMI ที่แสกนด้วย 100/Sn150 kV ทั้งนี้ เปอร์เซ็นต์ของข้อผิดพลาดในการวัดปริมาณไอโอดีนในช่วง 2.0-5.0 มก.ไอโอดีน/ซีซี อยู่ภายใน ±20% ในทุกๆค่าของ kV คู่

| สาขาวิชา | ฟิสิกส์การแพทย์ | ลายมือชื่อนิสิต ................................................ |
|---|---|---|
| ปีการศึกษา | 2564 | ลายมือชื่อ อ.ที่ปรึกษาหลัก ............................. |

# # 5974766530 : MAJOR MEDICAL PHYSICS

KEYWORD: hepatic lesion detectability, Dual energy computed tomography, virtual monoenergetic image (VMI), task-based image quality, Noise power spectrum, iodine quantification, Hepatocellular carcinoma, 3D-printed phantom, Detectability index, task transfer function (TTF)

Hataipat Jantawong : HEPATIC LESION DETECTABILITY ON DUAL ENERGY COMPUTED TOMOGRAPHY IMAGING: PHANTOM STUDY. Advisor: Assoc. Prof. ANCHALI KRISANACHINDA, Ph.D.

The purpose of this study is to determine the hepatic lesion detectability in abdomen from various phantom sizes by dual-energy computed tomography (DECT) imaging and to investigate the factors affecting the detectability of hepatic lesion in abdomen by dual-energy CT in phantom study. The anthropomorphic liver with nodule inserted phantom with extension rings simulating the small, medium, and large patients were scanned under DECT acquisitions by varying three kVp combinations (80/-,90/-, and 100/Sn150-kVp). The series of 40-,50-,60-, and 70-keV VMI were generated from DECT data set. All images were used to assess the task-based image quality; task transfer function (TTF), noise power spectrum (NPS), and detectability index (d') with the diagnostic task to detect 15 mm diameter hyperattenuating hepatic lesion based on clinical task of hepatocellular carcinoma (HCC) detection in CT imaging. In addition, the accuracy of iodine quantification in DECT for various kVp combinations was performed by using the customized 3D- printed liver nodule phantom. The result showed that the TTF increased as increasing the VMI energy level from 40-70 keV and the maximum values of 50%TTF ($f_{50}$) was found at 70 keV VMI. The noise magnitude increased as increasing the phantom size and decreasing the VMI-energy and when the kV on x-ray tube A increased. The results of d' demonstrated that as increased phantom sizes and decreased the energy level , the d' decreased. The measured iodine concentrations with DECT were strongly related to the true concentrations with the percentages of iodine quantification error within ±20% for concentration at 2.0-5.0 mgI/cc in all kV combinations. In conclusion, for the small phantom, the imaging condition yields the highest d' was at the 70keV-VMI acquired with 80/Sn150 kV. For the medium and large phantom sizes, the highest d' was at the 70keV-VMI acquired by 100/Sn150 kV. The percentage of iodine quantification error in the range of 2.0-5.0 mgI/cc was within ±20% in all kV combination settings.

| Field of Study: | Medical Physics | Student's Signature ............................. |
|---|---|---|
| Academic Year: | 2021 | Advisor's Signature ............................. |

# ACKNOWLEDGEMENTS

# TABLE OF CONTENTS

จุฬาลงกรณ์มหาวิทยาลัย

CHULALONGKORN UNIVERSITY

# LIST OF TABLES

xi

# LIST OF FIGURES

Page

# LIST OF ABBREVIATIONS AND SYMBOLS

| | |
|---|---|
| ABS | Acrylonitrile butadiene styrene |
| AM | Additive manufacturing |
| ADMIRE | Advanced modeled iterative reconstruction |
| AFP | Alpha-fetoprotein |
| AASLD | American Association for the Study of Liver Diseases |
| AAPM | American Association of Physicists in Medicine |
| ACR | American College of Radiology |
| APASL | Asian Pacific Association for the Study of the Liver |
| AEC | Automatic exposure control |
| ATCM | Automatic tube current modulation |
| $f_{av}$ | Average spatial frequencies |
| CdTe | Cadmium-telluride |
| CZT | Cadmium-zinc-telluride |
| cm | Centimeter |
| cvs | Comma separated values |
| CT | Computed tomography |
| CNR | Contrast-to-noise ratio |
| CTR | CT number Ratio |
| cc | Cubic centimeter |
| °C | Degree Celsius |
| d' | Detectability index |
| DICOM | Digital Imaging and Communications in Medicine |
| DECT | Dual Energy Computed Tomography |
| DECT-IQ | Dual energy computed tomography-based iodine quantification |
| DEI | Dual-energy index |
| DER | Dual-energy ratio |
| DE-VM | Dual-energy virtual monochromatic |

| DLCT | Dual-layer computed tomography |
|------|-------------------------------|
| DSCT | Dual-source computed tomography |
| ESF | Edge spread function |
| Zeff | Effective atomic number |
| $\alpha_c$ | Energy-independent contributions of $(\mu/\rho)_{Compton}$ |
| $\alpha_p$ | Energy-independent contributions of $(\mu/\rho)_{Photoelectric}$ |
| EASL | European Association for the Study of the Liver |
| EORTC | European Organization for Research and Treatment of Cancer |
| FBP | Filtered back projection |
| FWHM | Full-width-at-half-maximum |
| FDM | Fused deposition modelling |
| FFF | Fused Filament Fabrication |
| $Gd_2O_2S$ | Gadolinium Oxysulfide |
| g | Gram |
| HBV | Hepatitis B virus |
| HCV | Hepatitis C virus |
| HCC | Hepatocellular carcinoma |
| $E_H$ | High Photon energy |
| HU | Hounsfield unit |
| IRB | Institutional review board |
| IHC | Intrahepatic cholangiocarcinoma |
| IR | Iterative reconstruction |
| keV | Kiloelectron-volt |
| kg | Kilogram |
| kV | kilovoltage |
| KVSCT | Kilovoltage-switching computed tomography |
| kW | Kilowatts |
| LCR | Light curing resin |
| LSF | Line spread function |

| | |
|---|---|
| μ | Linear attenuation coefficient |
| LBI | Linear blended image |
| $E_L$ | Low photon energy |
| MRI | Magnetic resonance imaging |
| μ/ρ | Mass attenuation coefficient |
| $f_C(E)$ | Mass attenuation functions due to the compton scatter |
| $f_P(E)$ | Mass attenuation functions due to the photoelectric effect |
| ρ | mass density |
| MDI | material decomposition images |
| MPa | Megapascal |
| mAs | Milliampere seconds |
| mg | Milligram |
| mgI | Milligram iodine |
| mGy | Milligray |
| mm | Millimeter |
| ms | Millisecond |
| MTF | Modulation Transfer Function |
| ns | Nanosecond |
| NCCN | National Comprehensive Cancer Network |
| NIST | National Institution of Standard and Technology |
| NET | Neuroendocrine tumor |
| NPS | Noise Power Spectrum |
| NPW | Non-prewhitening matched filter |
| NPWE | Non-prewhitening observer model with eye filter |
| OATP | Organic anionic transporting polypeptide |
| kVp | Peak kilovoltage |
| % | Percentage |
| E | Photon energy |
| PA | Polyamide 12 |

| PEEK | Polyether ether ketone |
| --- | --- |
| PLA | Polylactic acid |
| PET | Positron emission tomography |
| lbs. | Pound |
| QA | Quality Assurance |
| RSNA | Radiological Society of North America |
| RP | Rapid prototyping |
| ROI | Region of interest |
| s | Second |
| SPECT | Single photon emission computed tomography |
| SE-LTP | single-energy low tube potential |
| $f_{10}$ | Spatial frequencies at 10% Task Transfer Function |
| $f_{50}$ | Spatial frequencies at 50% Task Transfer Function |
| SFCT | Split filter computed tomography |
| SD | Standard deviation |
| STL | Standard Tessellation Language |
| Sn | Stannous |
| $W_{task}$ | Task function |
| TTF | Task Transfer Function |
| 3D | Three-dimensional |
| VMI | Virtual monoenergetic image |
| VNC | Virtual non contrast |
| V/m | Volt per meter |
| $CTDI_{vol}$ | Volumetric computed tomography dose index |
| WL | Window level |
| WW | Window width |
| WHO | World Health Organization |

# CHAPTER 1

# INTRODUCTION

Cancer is ranked as a leading cause of death and an important barrier to increasing life expectancy in every country of the world. According to estimates from the World Health Organization (WHO) in 2019, cancer is the first or second leading cause of death before the age of 70 years in 112 of 183 countries and ranks third or fourth in a further 23 countries. Cancer's rising prominence as a leading cause of death partly reflects marked declines in mortality rates of stroke and coronary heart disease, relative to cancer, in many countries.[1]
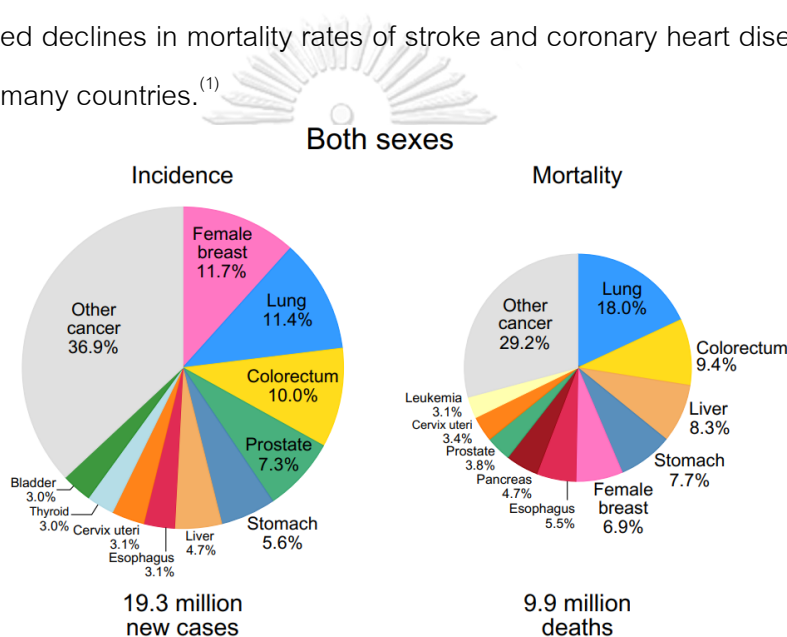


**Figure 1.1** Distribution of new cases and deaths for the top 10 most common cancers worldwide in 2020 for both sexes. Source: GLOBOCAN 2020.

Primary liver cancer is the sixth most-commonly diagnosed cancer and the third leading cause of cancer related death worldwide in 2020. Figure 1.1 shows distribution of new cases and deaths for the top 10 most common cancers worldwide in 2020 for both sexes where the area of the pie chart demonstrates the proportion of the total number of new cases or deaths; nonmelanoma skin cancers (excluding basal cell carcinoma for incidence) are included in the "other" , with approximately 906,000 new cases and 830,000 deaths (Table 1.1). The incidence of liver cancer varies widely by geographic

region, mainly due to the association of liver cancer with specific risk factors which differ in prevalence around the world.

Table 1.1 New cases and deaths for 36 cancers and all cancers combined in 2020. (1)

| CANCER SITE | NO. OF NEW CASES (% OF ALL SITES) | | NO. OF NEW DEATHS (% OF ALL SITES) | |
|---|---|---|---|---|
| Female breast | 2,261,419 | (11.7) | 684,996 | (6.9) |
| Lung | 2,206,771 | (11.4) | 1,796,144 | (18.0) |
| Prostate | 1,414,259 | (7.3) | 375,304 | (3.8) |
| Nonmelanoma of skin[a] | 1,198,073 | (6.2) | 63,731 | (0.6) |
| Colon | 1,148,515 | (6.0) | 576,858 | (5.8) |
| Stomach | 1,089,103 | (5.6) | 768,793 | (7.7) |
| Liver | 905,677 | (4.7) | 830,180 | (8.3) |
| Rectum | 732,210 | (3.8) | 339,022 | (3.4) |
| Cervix uteri | 604,127 | (3.1) | 341,831 | (3.4) |
| Esophagus | 604,100 | (3.1) | 544,076 | (5.5) |
| Thyroid | 586,202 | (3.0) | 43,646 | (0.4) |
| Bladder | 573,278 | (3.0) | 212,536 | (2.1) |
| Non-Hodgkin lymphoma | 544,352 | (2.8) | 259,793 | (2.6) |
| Pancreas | 495,773 | (2.6) | 466,003 | (4.7) |
| Leukemia | 474,519 | (2.5) | 311,594 | (3.1) |
| Kidney | 431,288 | (2.2) | 179,368 | (1.8) |
| Corpus uteri | 417,367 | (2.2) | 97,370 | (1.0) |
| Lip, oral cavity | 377,713 | (2.0) | 177,757 | (1.8) |
| Melanoma of skin | 324,635 | (1.7) | 57,043 | (0.6) |
| Ovary | 313,959 | (1.6) | 207,252 | (2.1) |
| Brain, nervous system | 308,102 | (1.6) | 251,329 | (2.5) |
| Larynx | 184,615 | (1.0) | 99,840 | (1.0) |
| Multiple myeloma | 176,404 | (0.9) | 117,077 | (1.2) |
| Nasopharynx | 133,354 | (0.7) | 80,008 | (0.8) |
| Gallbladder | 115,949 | (0.6) | 84,695 | (0.9) |
| Oropharynx | 98,412 | (0.5) | 48,143 | (0.5) |
| Hypopharynx | 84,254 | (0.4) | 38,599 | (0.4) |
| Hodgkin lymphoma | 83,087 | (0.4) | 23,376 | (0.2) |
| Testis | 74,458 | (0.4) | 9334 | (0.1) |
| Salivary glands | 53,583 | (0.3) | 22,778 | (0.2) |
| Anus | 50,865 | (0.3) | 19,293 | (0.2) |
| Vulva | 45,240 | (0.2) | 17,427 | (0.2) |
| Penis | 36,068 | (0.2) | 13,211 | (0.1) |
| Kaposi sarcoma | 34,270 | (0.2) | 15,086 | (0.2) |
| Mesothelioma | 30,870 | (0.2) | 26,278 | (0.3) |
| Vagina | 17,908 | (0.1) | 7995 | (0.1) |
| All sites excluding nonmelanoma skin | 18,094,716 | | 9,894,402 | |
| All sites | 19,292,789 | | 9,958,133 | |

[a]New cases exclude basal cell carcinoma, whereas deaths include all types of nonmelanoma skin cancer.
Source: GLOBOCAN 2020.

| Number of new cases in 2020, both sexes, all ages | Data source and methods |
|---|---|

**Incidence**
**Country-specific data source**: Bangkok Cancer Registry, Chiang Mai Cancer Registry, Chonburi Cancer Registry, Khon Kaen Cancer Registry, Lampang Cancer Registry, Lopburi Cancer Registry, Songkhla Cancer Registry, Surat Thani Cancer Registry
**Method**: Weighted/simple average of the most recent local rates applied to 2020 population

**Mortality**
**Country-specific data source**: National (WHO)
**Method**: Estimated from national incidence estimates by modelling, using incidence:mortality ratios derived from cancer registry data in neighbouring countries

**Prevalence**
Computed using sex-; site- and age-specific incidence to 1-;3- and 5-year prevalence ratios from Nordic countries for the period (2006-2015), and scaled using Human Development Index (HDI) ratios.

(A)

Liver 27 394 (14.4%)
Lung 23 713 (12.4%)
Breast 22 158 (11.6%)
Colorectum 21 103 (11.1%)
Cervix uteri 9 158 (4.8%)
Other cancers 87 110 (45.7%)

Incidence, Mortality and Prevalence by cancer site

| Cancer | New cases Number | Rank | (%) | Cum.risk | Deaths Number | Rank | (%) | Cum.risk | 5-year prevalence (all ages) Number | Prop. (per 100 000) |
|---|---|---|---|---|---|---|---|---|---|---|
| Liver | 27 394 | 1 | 14.4 | 2.50 | 26 704 | 1 | 21.4 | 2.44 | 26 606 | 38.12 |
| Lung | 23 713 | 2 | 12.4 | 2.14 | 20 395 | 2 | 16.3 | 1.80 | 25 164 | 36.05 |
| Breast | 22 158 | 3 | 11.6 | 4.12 | 8 266 | 3 | 6.6 | 1.39 | 76 440 | 213.32 |
| Colon | 10 864 | 4 | 5.7 | 0.92 | 6 039 | 4 | 4.8 | 0.38 | 26 907 | 38.55 |
| Rectum | 9 884 | 5 | 5.2 | 0.94 | 5 292 | 5 | 4.2 | 0.41 | 27 037 | 38.73 |
| Cervix uteri | 9 158 | 6 | 4.8 | 1.70 | 4 705 | 6 | 3.8 | 0.83 | 24 589 | 68.62 |
| Prostate | 8 630 | 7 | 4.5 | 1.56 | 3 837 | 8 | 3.1 | 0.31 | 30 537 | 89.90 |
| Non-Hodgkin lymphoma | 7 087 | 8 | 3.7 | 0.70 | 4 125 | 7 | 3.3 | 0.37 | 19 892 | 28.50 |
| Bladder | 5 021 | 9 | 2.6 | 0.34 | 3 203 | 12 | 2.6 | 0.13 | 13 805 | 19.78 |
| Lip, oral cavity | 4 770 | 10 | 2.5 | 0.45 | 2 545 | 15 | 2.0 | 0.21 | 12 759 | 18.28 |
| Leukaemia | 4 577 | 11 | 2.4 | 0.46 | 3 308 | 9 | 2.6 | 0.32 | 12 747 | 18.26 |
| Corpus uteri | 4 524 | 12 | 2.4 | 0.90 | 1 382 | 18 | 1.1 | 0.26 | 14 206 | 39.64 |
| Ovary | 4 475 | 13 | 2.3 | 0.84 | 2 941 | 14 | 2.4 | 0.54 | 11 843 | 33.05 |
| Stomach | 4 221 | 14 | 2.2 | 0.39 | 3 221 | 11 | 2.6 | 0.28 | 6 060 | 8.68 |
| Thyroid | 3 646 | 15 | 1.9 | 0.38 | 397 | 25 | 0.32 | 0.03 | 11 941 | 17.11 |
| Oesophagus | 3 447 | 16 | 1.8 | 0.34 | 3 176 | 13 | 2.5 | 0.31 | 3 698 | 5.30 |
| Pancreas | 3 335 | 17 | 1.7 | 0.25 | 3 306 | 10 | 2.6 | 0.25 | 2 397 | 3.43 |
| Brain, central nervous system | 2 734 | 18 | 1.4 | 0.27 | 2 310 | 16 | 1.8 | 0.22 | 7 239 | 10.37 |
| Nasopharynx | 2 316 | 19 | 1.2 | 0.24 | 1 482 | 17 | 1.2 | 0.15 | 6 848 | 9.81 |
| Kidney | 2 170 | 20 | 1.1 | 0.20 | 1 230 | 20 | 0.99 | 0.09 | 5 516 | 7.90 |
| Gallbladder | 1 883 | 21 | 0.99 | 0.17 | 1 322 | 19 | 1.1 | 0.12 | 2 169 | 3.11 |
| Larynx | 1 800 | 22 | 0.94 | 0.16 | 1 051 | 22 | 0.84 | 0.07 | 5 145 | 7.37 |
| Multiple myeloma | 1 411 | 23 | 0.74 | 0.13 | 1 222 | 21 | 0.98 | 0.11 | 3 296 | 4.72 |
| Oropharynx | 1 086 | 24 | 0.57 | 0.11 | 529 | 23 | 0.42 | 0.05 | 2 718 | 3.89 |
| Hypopharynx | 841 | 25 | 0.44 | 0.09 | 473 | 24 | 0.38 | 0.05 | 1 366 | 1.96 |
| Penis | 691 | 26 | 0.36 | 0.15 | 258 | 27 | 0.21 | 0.05 | 2 042 | 6.01 |
| Melanoma of skin | 607 | 27 | 0.32 | 0.06 | 309 | 26 | 0.25 | 0.03 | 1 774 | 2.54 |
| Salivary glands | 538 | 28 | 0.28 | 0.06 | 206 | 28 | 0.16 | 0.02 | 1 662 | 2.38 |
| Anus | 355 | 29 | 0.19 | 0.03 | 133 | 29 | 0.11 | 0.01 | 946 | 1.36 |
| Hodgkin lymphoma | 321 | 30 | 0.17 | 0.03 | 90 | 31 | 0.07 | 0.01 | 1 063 | 1.52 |
| Vulva | 258 | 31 | 0.14 | 0.04 | 90 | 30 | 0.07 | 0.01 | 776 | 2.17 |
| Testis | 254 | 32 | 0.13 | 0.05 | 56 | 33 | 0.04 | 0.01 | 918 | 2.70 |
| Vagina | 165 | 33 | 0.09 | 0.03 | 82 | 32 | 0.07 | 0.01 | 426 | 1.19 |
| Kaposi sarcoma | 78 | 34 | 0.04 | 0.01 | 36 | 34 | 0.03 | 0.00 | 218 | 0.31 |
| Mesothelioma | 40 | 35 | 0.02 | 0.00 | 34 | 35 | 0.03 | 0.00 | 49 | 0.07 |
| **All cancer sites** | 190 636 | - | - | 16.36 | 124 866 | - | - | 10.22 | 426 366 | 610.8 |

(B)

**Figure 1.2** Summary of cancer statistics in Thailand (2020). (A) Distribution of new cases for the most common cancers for both sexes and all ages. (B) Country-specific incidence, mortality, and prevalence by cancer sites for both sexes in 2020. Source: GLOBOCAN 2020.

According to the GLOBOCAN 2020, the incidence rate of liver cancer is the first-most common cancer in Thailand (Figure 1.2). The age-standardized incidence rate of hepatocellular carcinoma, HCC in both sexes is 22.6 per 100,000/year whereas the age-standardized incidence rates in men are 33.8 per 100,000/year and 12.9 per 100,000/year in men and in women, respectively. Moreover, the mortality rate of liver cancer is also the first most common cause of cancer death in Thailand. The age-standardized mortality rate

of HCC is 21.9 per 100 000/year. The age-standardized mortality rates in men are 33.0 per 100,000/year and 12.3 per 100,000/year in women, respectively. Therefore, the number of new cases of liver cancer in Thailand is 27,394 and the number of deaths is 26,704 which is No. 1 ranked cancer site in Thailand (Figure 1.2B.).

Primary liver cancer includes hepatocellular carcinoma (HCC) (comprising 75%-85% of cases) and intrahepatic cholangiocarcinoma (IHC) (10%-15%), as well as other rare types. The main risk factors for HCC are cirrhosis, chronic infection with hepatitis B virus (HBV) or hepatitis C virus (HCV), aflatoxin-contaminated foods, heavy alcohol intake, excess body weight, type 2 diabetes, and smoking.[2, 3] Even though there are many improvements in therapeutic options for HCC but the overall prognosis has remained unsatisfied with a 5-year survival rate below 20%.[4] This is because of the HCC is mostly asymptomatic therefore it is often detected at a late stage. The purpose of screening and surveillance is to detect a disease early in its course to offer a beneficial treatment and ultimately decrease mortality. Once symptoms develop, the disease is often advanced and not amenable to curative therapy via resection, transplantation, or percutaneous ablation. Therefore, HCC surveillance is widely adopted to at-risk individuals and is currently recommended by most professional societies; American Association for the Study of Liver Diseases (AASLD), European Association for the Study of the Liver (EASL), Asian Pacific Association for the Study of the Liver (APASL) and National Comprehensive Cancer Network (NCCN) (Table 2). Currently, despite new recommendations from AASLD, both serologic (alpha-fetoprotein: AFP) and ultrasound imaging methods are used in surveillance of HCC. Computed tomography (CT) scan and magnetic resonance imaging (MRI) are not recommended as the first line modality for the surveillance of HCC in patients with cirrhosis. However, CT or MRI is sometime utilized, in select patients with a high likelihood of having an inadequate visualization from ultrasound or if ultrasound is attempted but inadequate.

Table 1.2 Recommendations for HCC surveillance in high-risk patients. [5-8]

| American Association for the Study of Liver Diseases (AASLD) | European Association for the Study of the Liver (EASL) | Asian Pacific Association for the Study of the Liver (APASL) | National Comprehensive Cancer Network (NCCN) |
|---|---|---|---|
| Ultrasound every 6 months | Ultrasound and AFP every 6 months | Ultrasound and AFP every 6 months | Ultrasound and AFP every 6 months |

Recall policies include investigations and follow-up that determine whether an initial abnormality finding on surveillance is an HCC or not. The process starts with an abnormal result, i.e., any new nodule (not seen on a prior study) should be considered abnormal. Typically, abnormalities such as a lesion seen on ultrasound are followed up by a CT scan or MRI, and if the results are still equivocal, biopsy is recommended.

Accuracy of liver masses characterization is crucial to patient management, especially in patients with chronic liver disease. Furthermore, an assessment of treatment response is largely dependent upon optimal utilization of cross-sectional imaging. In current clinical practice, widespread use of imaging modalities including CT and MRI has led to an overall accurate detection and characterization of liver tumors. Several guidelines including the American Association for the Study of Liver Diseases (AASLD), the European Association for the Study of the Liver (EASL), the European Organization for Research and Treatment of Cancer (EORTC), the American College of Radiology (ACR), and the Liver Imaging Reporting and Data System (LI-RADS) recommended diagnostic evaluation of HCC based on the findings from multiphase CT and/ or MRI such as arterial hyperenhancement, venous washout, enhancing capsule, size, and threshold growth.

The multiphasic contrast-enhanced Computed Tomography (CT) is one of the most used imaging modalities for HCC diagnosis, with image acquisition at arterial (late arterial phase is preferred at approximately 35 s after injection), portal venous (at approximately 75 s after injection), and delayed phases. Pooled analysis study in assessing the diagnostic performance of contrast-enhanced CT demonstrated the overall sensitivity and specificity of 70-81% and 79-94% ,respectively for the diagnosis of liver tumor.[5] Even though MRI (especially gadoxetic acid–enhanced MRI) provides higher accuracy for detection of liver tumors, but the CT imaging has been widely used owing to

its availability, feasibility, lower cost and requires less expertise to perform and to interpret images.

The treatment for liver cancer is most effective when the tumor is small thus the detection of small hepatic lesion is essential for disease management.  For detection of liver tumor, tumor-to-liver contrast and lesion conspicuity on CT images is of primary importance. Therefore, the lower noise images and multiphase acquisition are required to detect subtle or small hepatic lesions, these potentially results to increase in radiation dose to the patients compare to the other body structures such as bone or lung CT imaging.

With a focus on lesion detection, the iterative reconstruction (IR) algorithms are gaining wide-scale clinical implementation, providing substantial noise reduction while maintaining the spatial resolution for visualization of fine details. However, they do so by creating unique image textures and properties that are different from those shown with traditional filtered back projection (FBP) algorithms.[6] Results from recent researchers suggested that iterative reconstruction (IR) algorithms may not significantly improve low contrast detectability of small lesion size (5 mm).[7, 8]

Dual-energy CT (DECT) was considered a promising development in CT that had a potential to improve lesion detection and characterization beyond the levels currently achieved by conventional single energy CT.[9, 10] Theoretically, a series of virtual monoenergetic images (VMIs) of various keV levels (40-190 keV) could be generated from material-decomposition images, which can be used to enhance pathology or reduce artifacts. The selected VM energy should target the diagnostic task. Typically, low-energy VMIs provide greater image contrast between adjacent structures but have more noise, especially in larger patients. On the other hand, high-energy VMIs provide less contrast but less noise. Recent studies have highlighted the potential benefits of dual-energy VMIs including improved image quality, increased contrast-to-noise ratio (CNR), improved lesion conspicuity and reduced beam hardening artifacts. By generating quantitative material decomposition images (MDIs), DECT has ability to  visualize any subtle enhancements lesion that can be utilized as an imaging biomarker for better assessment

of small tumors. Muenzel et al.[11] assessed the diagnostic performance of MDIs for detection of hypervascular liver tumors and showed a significantly higher liver-to-lesion and contrast-to-noise ratio for this method when compared with monoenergetic 65-keV images and contrast-enhanced MRI.[11] Investigators also revealed that DECT iodine quantification and material attenuation analysis had higher specificity (93%) in detection of small (< 2 cm) hypoattenuating liver tumors when compared with conventional measurements (70%).[11] Kaltenbach et al.(12) assessed the utilizing of iodine quantification to distinguish hepatic neuroendocrine tumor metastasis (NET) from HCCs by using normalized iodine uptake measures. The results showed the sensitivity and specificity of 100% and 90.2%, respectively.[12]

As mentioned above , there are many clinical studies have assessed the diagnostic performance in HCC detection from different synthetic images generated by dual energy acquisition in various DECT platforms. However, the results demonstrated the various outcomes due to the diversity clinical DECT protocol and practices implemented in each center and the different of DECT techniques available. Several phantom studies have assessed and compared the spectral performance of various DECT platform for different type of synthetic images in term of images quality and their ability to detect the subtle liver lesion in abdomen CT. However, the researcher used the different image quality evaluation methods and different image quality metrices this may lead to misunderstanding and confusion when scientific results are implemented in clinical practices.

# CHAPTER 2

# REVIEW OF RELATED LITERATURE

## 2.1 Theory

### 2.1.1 Hepatocellular carcinoma (HCC)

Hepatocellular carcinoma (HCC) is an epithelial tumor originating in the liver and composed of cells with similar characteristics as those of normal hepatocytes. It is the sixth most-commonly diagnosed cancer and the third leading cause of cancer related death worldwide in 2020. The highest incidence rates are found mainly in transitioning countries, with the disease being the most common cancer in 11 geographically diverse countries in Eastern Asia (Mongolia, which has rates far exceeding any other country), South-Eastern Asia (e.g., Thailand, Cambodia, and Viet Nam), and Northern and Western Africa (e.g., Egypt and Nigeria). Liver cancer is the leading cause of cancer related death in Mongolia, Thailand, Cambodia, Egypt, Guatemala among both men and women and in an additional 18 countries among men (Figure 2.1).

The most important clinical risk factor for HCC is cirrhosis, with approximately 80% of HCC cases developing in patients with a cirrhotic liver disease. The exact incidence depends on the cause of cirrhosis (highest incidence in patient infected with hepatitis C virus or hepatitis B virus), severity of cirrhosis (highest incidence in those with decompensated cirrhosis), geographic region (higher in Asia than in Europe or United States), and sex (higher in men than women). The individuals with multiple risk factors are higher risk as well as in those coinfected with human immunodeficiency virus. However, the HCC may be developed in non-cirrhotic patient, especially those with long-standing chronic liver inflammation from hepatitis B virus or hepatitis C virus infection or nonalcoholic steatohepatitis, but at a much lower rate than those with cirrhosis. Other risk factors for HCC include heavy alcohol consumption, tobacco smoking, obesity, diabetes, hereditary hemochromatosis, high dietary consumption of aflatoxins, and family history of HCC.
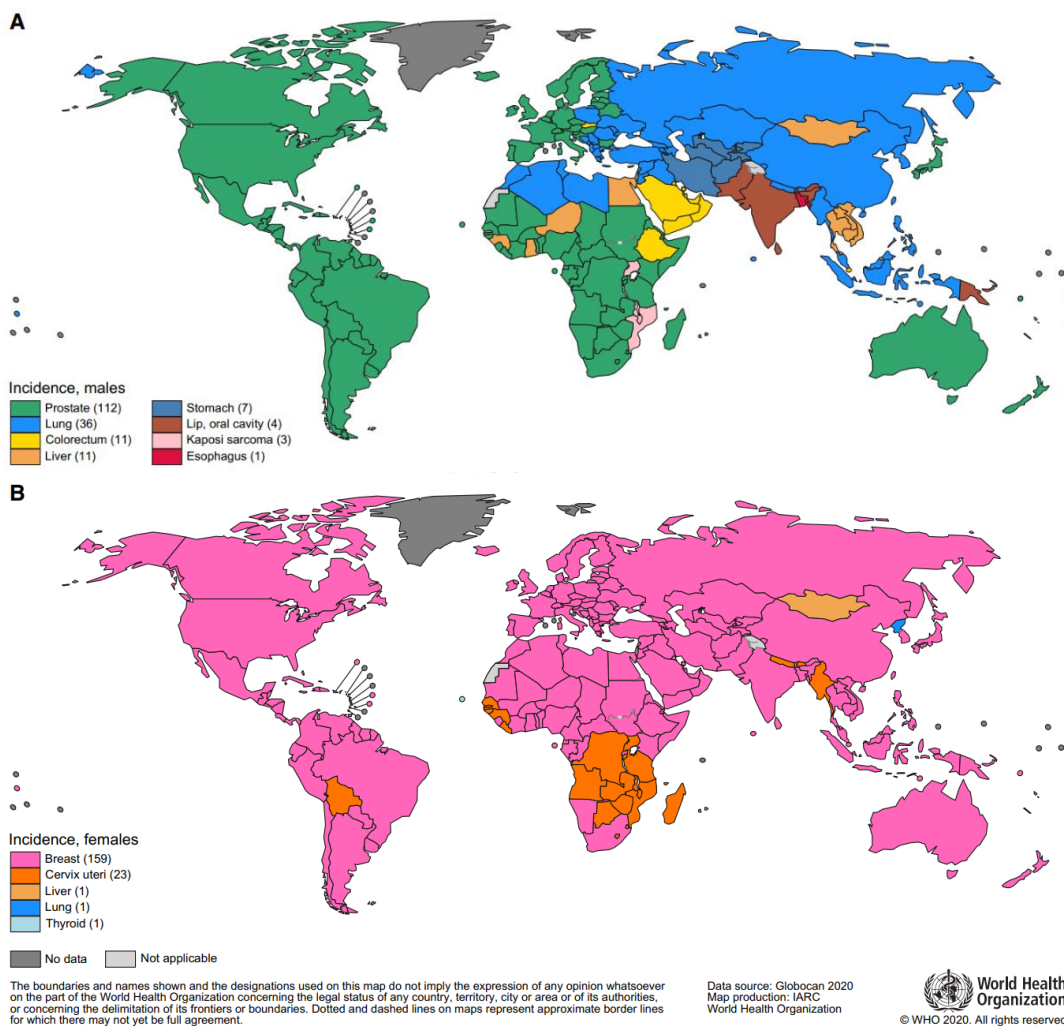
Figure 2.1 Most common type of cancer incidence in 2020 in each country among (A) Males and (B) Females. Source: GLOBOCAN 2020.[1]
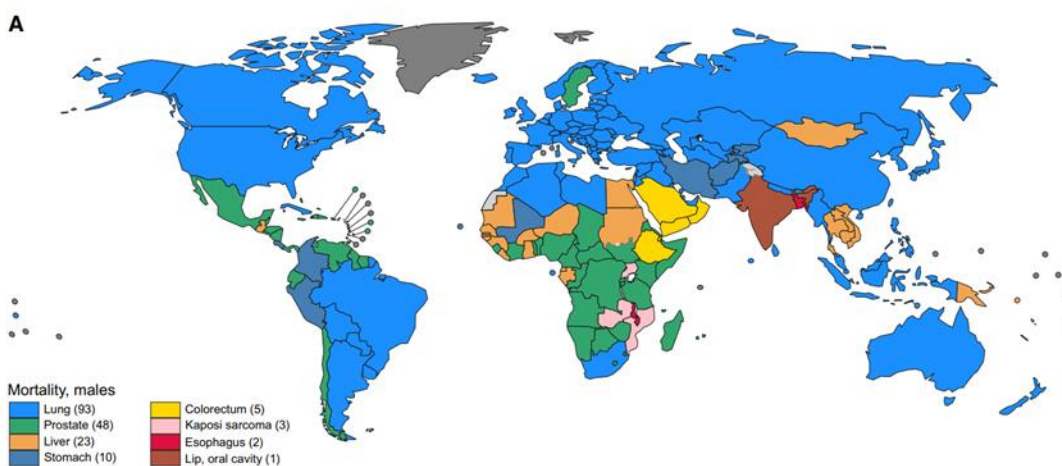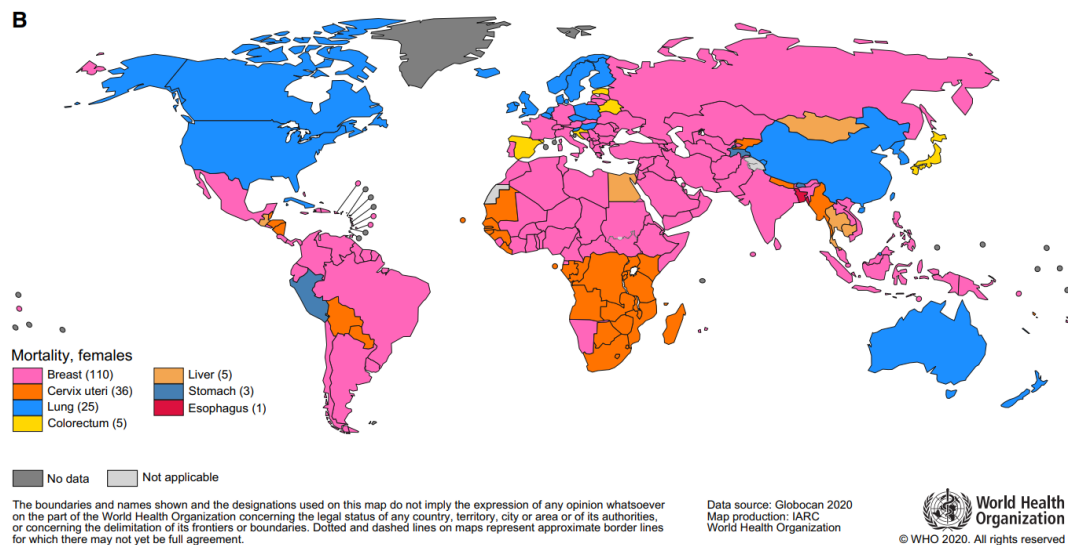
**Figure 2.2** Most common type of cancer mortality by country in 2020 among (A) Males and (B) Females. Source: GLOBOCAN 2020.[1]

The prognosis of HCC largely depends on the stage of detection. Patients who present with symptoms generally have a poor prognosis, as HCC usually does not produce obvious symptoms beyond those of the underlying liver disease until it has become incurable; in such patients, median survival is less than 1 year and the 5-year survival rate is less than 10%.[13] In comparison to patients in whom HCC is detected at an early stage, they may benefit from life-prolonging, potentially curative treatments.

The detection of HCC in early stage, therefore, is critical to improve the survival rate of affected patients. Therefore, professional societies have released clinical management guidelines that advocate surveillance of patients at risk due to cirrhosis or chronic viral hepatitis. While the surveillance strategies incorporated by the various guidelines differ, all current guidelines recommend ultrasonography (US) as the first line imaging test for surveillance, and two guidelines advocate the ancillary use of serum biomarkers. In general, neither computed tomography (CT) nor magnetic resonance (MR) imaging is recommended for surveillance, although three guidelines permit these modalities for surveillance of patients in whom US visualization is limited by obesity or other factors and for individuals at very high risk for HCC development. Once a surveillance test is positive (i.e., an abnormality is detected that may represent HCC), a more definite imaging examination is recommended for noninvasive diagnosis and

staging of HCC. The Figure 2.3 demonstrates the AASLD surveillance and diagnostic algorithm for recall after an abnormal screening ultrasound.
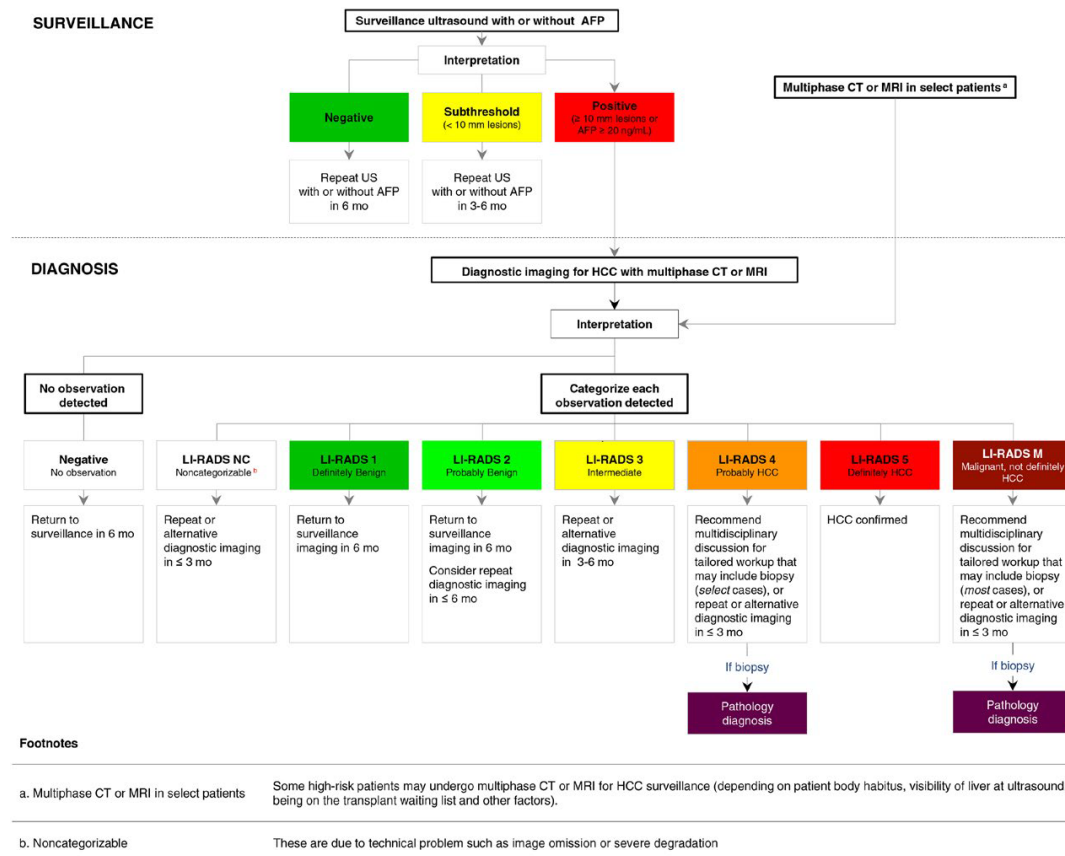


**Figure 2.3** AASLD surveillance and diagnostic algorithm.

Currently, all guidelines endorse multiphasic CT and MR imaging with extracellular contrast agents as a first-line imaging modalities for diagnosis and staging of HCC , although guidelines in Japan also advocate MR imaging with gadoxetate disodium (a hepatobiliary agent) as a second-line modality. Figure 2.4 shows multiphasic CT examinations of a 51-year-old-man with HCC performed with image acquisition of pre-contrast and dynamically post contrast agent administration scans with enhancing phases of late arterial, portal venous, and delayed phase. (a) There is no discernible lesion on pre-contrast CT image. (b) Late arterial phase image shows heterogeneously hyper-enhancing mass with mosaic architecture in segment VIII of the liver. Notice enhancement of hepatic artery and portal vein branches in late arterial phase. Hepatic veins are not enhanced. (c, d) Relative to liver, mass shows hypo-enhancement on (c) portal venous

and (d) 3-minute delayed phase images to become iso-attenuating with background parenchyma. Mass has capsule appearance in venous phases, shown to best advantage in delayed phase. Notice that hepatic veins are enhanced in portal venous and delayed phases. (e) Gross pathology photograph of resected specimen confirms progressed, encapsulated HCC with expansile growth pattern. Moreover, single-energy CT is more susceptible to beam hardening artifacts, especially in a large patient.
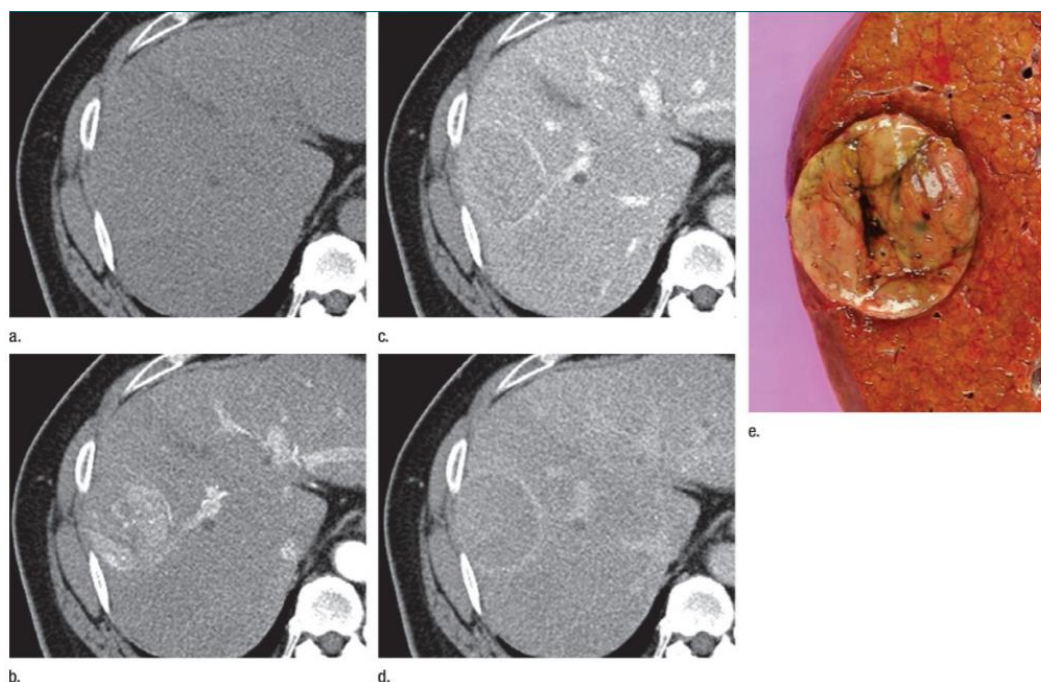


**Figure 2.4** Images in a 51-year-old man with HCC: multiphasic CT technique. (a) Pre-contrast CT image, (b) Late hepatic arterial phase image, (c) Portal venous, (d) 3-minute delayed phase images and (e) Gross pathology photograph of resected specimen confirms progressed, encapsulated HCC.[14]

### 2.1.1.1 HCC development, growth, and spread

Hepatocarcinogenesis, the gradual transformation of nonmalignant liver cells into HCC, is a complex, multistep process characterized at the molecular and cellular level by the progressive accumulation of epigenetic and genetic alterations and at the histologic level by the emergence and progression of successively more advanced precancerous, early cancerous, and overtly malignantly lesions.

Pathologically, multistep hepatocarcinogenesis is characterized by progressive dedifferentiation of phenotypically abnormal nodular lesions (Figure 2.5). The evolution is driven by the repeated development and expansion of successively less differentiated clonal populations, often presenting as sub nodules within parent nodules. Over time, the less differentiated populations grow and completely replace the more differentiated surrounding tissues. Repeated cycles of clonal development and expansion eventually produce lesions with malignant phenotype. The process represents a biologic continuum but is arbitrarily divided into discrete steps for simplicity, clinical utility, and investigation. Importantly, the process may occur simultaneously at different rates in different parts of the liver (multicentric hepatocarcinogenesis). It should be emphasized that although most HCCs probably evolve from histologically abnormal precursor lesions, it is possible that many HCCs, especially those arising in noncirrhotic livers, may develop from transformed malignant cells without transitioning through histologically definable intermediate steps. The development of HCC without identifiable histologic precursors is termed "de novo hepatocarcinogenesis".

Figure 2.5 is schematic drawing illustrates typical changes in intra-nodular hemodynamics and Organic anionic transporting polypeptide (OATP) expression during multistep hepatocarcinogenesis. As shown, multistep hepatocarcinogenesis is characterized by successive selection and expansion of less-differentiated sub-nodules within more well differentiated parent nodules. The sub-nodules grow and eventually replace (blue arrows) the parent nodules. Progressed HCCs show expansible growth (red arrows) and characteristically are encapsulated with fibrous septa. Earlier nodules lack these structures and show replacing growth. During hepatocarcinogenesis, the density of portal triads diminishes while the density of unpaired arteries increases. The net effect is that intra-nodular arterial supply diminishes initially and then increases (bottom graph); progressed HCCs typically show arterial hypervascularity compared with background liver, while earlier nodules typically do not. OATP expression usually diminishes progressively (top graph); progressed HCCs, early HCCs, many high-grade dysplastic nodules, and some low-grade dysplastic nodules show OATP under expression

compared with background liver. The shaded area in each graph represents the window of opportunity to detect nodules at different stages of tumor development based on net arterial flow or OATP expression; window of opportunity is larger and begins at earlier stages for OATP expression. Note that illustrations and graphs reflect typical changes in hemodynamics and OATP expression. Not all nodules exhibit the illustrated characteristics. Also note that during tumor development some stages may be skipped and not all HCCs arise from histologically definable precursor lesions.(Illustration by Matt Skalski, MD; copyright 2014, Radiological Society of North America : RSNA.)
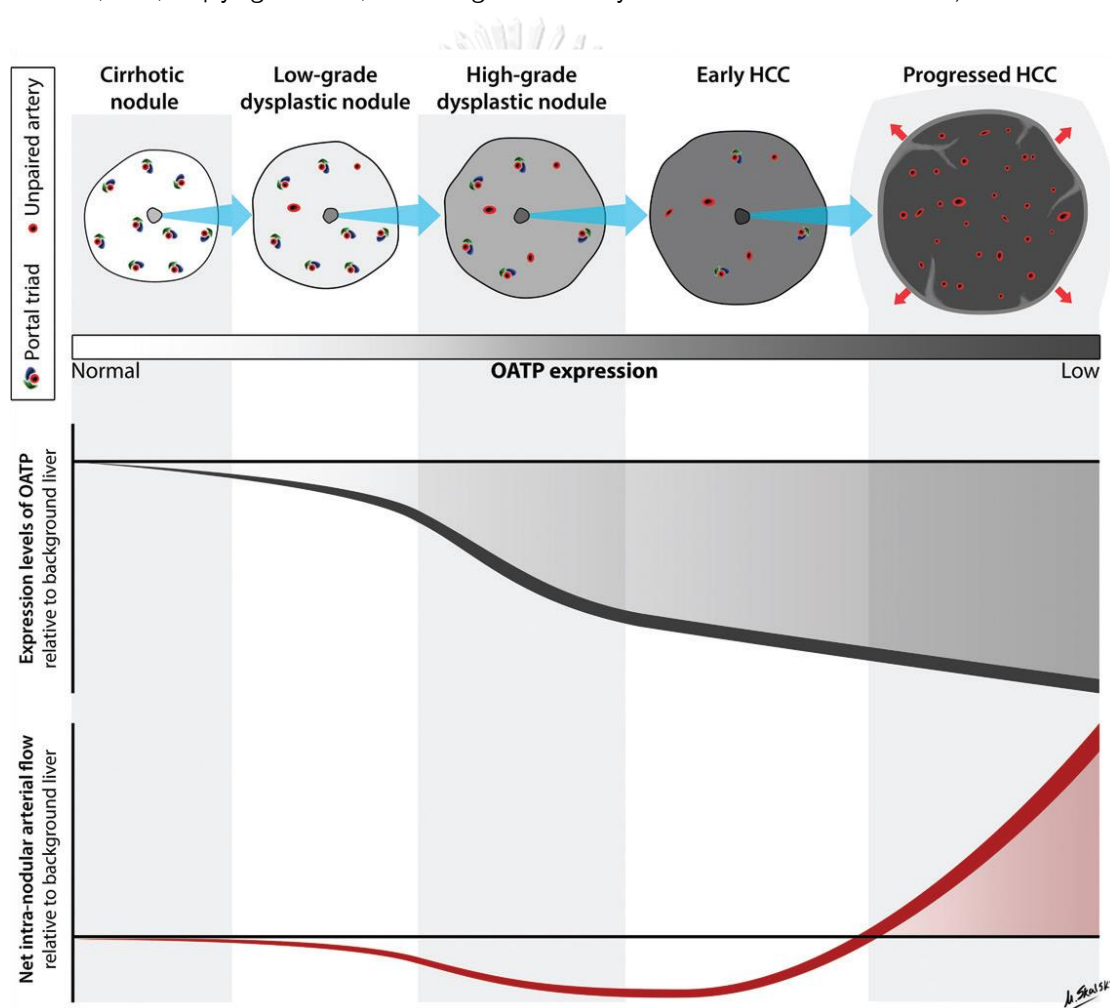


**Figure 2.5** Hemodynamic and Organic anionic transporting polypeptide (OATP) expression changes during multistep hepatocarcinogenesis.[14]

*Cirrhotic nodules*—Cirrhotic nodules, also known as cirrhosis-associated regenerative nodules, are innumerable well-defined rounded regions of the cirrhotic

parenchyma surrounded by scar tissue and typically measuring 1-15 mm in diameter. Cirrhotic nodules larger than 1 cm are called "large cirrhotic nodules" or "large regenerative nodules." Grossly and microscopically, cirrhotic nodules are indistinguishable from other cirrhotic nodules in other words, all cirrhotic nodules in a given liver resemble each other and no cirrhotic nodule stands out as being distinctive from the others. Cirrhotic nodules lack clonal features histologically, and the cells are phenotypically normal. For these reasons, cirrhotic nodules usually are considered "benign." The "benignity" of cirrhotic nodules is not unqualified, however. Based on molecular analyses, many cirrhotic nodules are clonal expansions of genomically aberrant cells, and hepatocytes within cirrhotic nodules may develop dysplastic features and thus give rise to dysplastic foci and nodules. As discussed below, most cirrhotic nodules are not discernible as individual lesions at in vivo imaging.

*Dysplastic foci*—Dysplastic foci are microscopic lesions, arbitrarily less than 1 mm in diameter, composed of hepatocytes with precancerous features such as small cell change arising within cirrhotic nodules or, if the liver is noncirrhotic, within single lobules. These lesions are identified incidentally at histologic evaluation and not detectable by means of in vivo imaging. As it is not possible to detect or follow them in vivo, their natural history is poorly understood. It is presumed that dysplastic foci may expand to become dysplastic nodules.

*Dysplastic nodules*.—Dysplastic nodules are nodular lesions, usually 1–1.5 cm in diameter, that differ in both macroscopic (size, color, or consistency) and microscopic appearance from background parenchyma . They are observed in up to 25% of cirrhotic livers but occasionally are detected in noncirrhotic livers and often are multiple. Dysplastic nodules are classified as low grade or high grade, depending on the presence of cytologic and architectural atypia.

Histologically, low-grade dysplastic nodules resemble cirrhotic nodules. The hepatocytes show no cytologic atypia, and neither expansile sub nodules nor architectural alterations beyond those of cirrhotic nodules are observed. Findings that if present

distinguish low-grade dysplastic nodules from cirrhotic nodules include unpaired arteries and clonelike populations (aggregates of cells with greater copper, iron, or fat accumulation than background liver). High grade dysplastic nodules resemble well differentiated HCCs. The cells show cellular atypia, although the atypia is insufficient to establish a diagnosis of HCC and may exhibit clonelike features. Architectural alterations, including arrangement of hepatocytes in thin trabeculae and pseudo-glands, may be present. Expansile sub nodules with varying degrees of atypia may be observed.

Clinically, low-grade dysplastic nodules are considered preneoplastic lesions with slightly elevated risk of malignant transformation, while high-grade dysplastic nodules are considered advanced precursors of HCC with high risk of transformation. Some high-grade dysplastic nodules contain one or more sub nodules of well-differentiated or moderately differentiated HCC ("nodule-in-nodule" configuration); these are appropriately categorized as "HCC arising in high-grade dysplastic nodule". The CT and MR imaging have limited ability to identify and characterize dysplastic nodules.

*Early HCCs*— Early HCCs are an incipient stage of HCC development, analogous to "carcinoma in situ" or "microinvasive carcinoma" of other organs. Unlike overt progressed HCC, which displaces or destroys the liver parenchyma, early HCCs grow by gradually replacing the parenchyma; as the cells spread, they surround neighboring portal tracts and central veins but do not displace or completely destroy these structures. Early HCCs typically measure 1–1.5 cm in diameter and rarely exceed 2 cm. Macroscopically, most early HCCs are vaguely nodular with indistinct margins and without a tumor capsule. Due to their small size and macroscopic appearance, these lesions frequently are termed "vaguely nodular small HCCs" or "small HCCs with indistinct margins.". The lesions are indistinguishable from high-grade dysplastic nodule at gross pathologic examination. Histologically, early HCCs consist of small, well-differentiated neoplastic cells arranged in irregular but thin trabeculae or pseudoglands. Thus, the microscopic appearance closely resembles that of high-grade dysplastic nodules.

The key distinguishing feature, present in early HCCs but not in high-grade dysplastic nodule, is stromal invasion, defined as infiltration of tumor cells into the fibrous

tissue surrounding portal tracts retained within the nodule or into the stromal fibrous tissue surrounding the nodule. While stromal invasion is characteristic, vascular invasion is not observed, and intrahepatic metastasis is exceedingly rare. Early HCCs are considered precursors of progressed HCCs, although the rate at which they transform to progressed HCC has not been defined. Moreover, some progressed HCCs probably do not develop from early HCCs but rather arise as expansile sub nodules within high-grade dysplastic nodules without transitioning through a vaguely nodular morphology. The conventional CT and MR imaging have limited sensitivity for the detection of early HCCs, but hepatobiliary phase MR imaging shows promise for this purpose.

*Progressed HCCs*— Progressed HCCs are overtly malignant lesions with the ability to invade vessels and metastasize. Macroscopic and histologic features are variable, depending in part on lesion size. Progressed HCCs smaller than 2 cm are distinctly nodular with well-defined margins; synonymous terms include "small and progressed HCCs" and "small distinctly nodular HCCs." Unlike early HCCs, small and progressed HCCs grow by expanding into and compressing the adjacent parenchyma. Characteristically, they are surrounded by a tumor capsule and contain internal fibrous septa. Histologically, about 80% of small and progressed HCCs are moderately differentiated; the remaining 20% consist of both well-differentiated and moderately differentiated components. Architectural abnormalities include thickened plates more than three cells wide and arrangement of hepatocytes in trabecular/platelike, pseudoglandular/acinar, or solid/compact patterns. A significant proportion of small and progressed HCCs are associated with vascular invasion and intrahepatic metastasis. HCCs exceeding 2 cm in diameter are known as "large HCCs." Compared with small and progressed HCCs, large HCCs tend to have higher histologic grade, more aggressive biologic behavior, and higher frequency of vascular invasion and metastasis. For these reasons, it is clinically important to develop imaging techniques that can be used to accurately diagnose small HCCs prior to their growth beyond 2 cm. Macroscopically, most large HCCs are expansile tumors with nodular morphology and surrounded by tumor capsules. Mosaic architecture is characteristic, defined by the presence of multiple

internal tumor nodules separated by fibrous septations and areas of hemorrhage, necrosis, and occasionally fatty metamorphosis. Histologically, the internal tumor nodules may differ in grade, microscopic architectural pattern, and cytologic type. Molecularly, they may differ in epigenetic and genetic abnormalities. At least some of these nodules appear to arise through clonal divergence from common precursor clonal populations. About 5% of large HCCs have an infiltrative rather than an expansile growth pattern; these cancers usually are composed of poorly differentiated or undifferentiated cancer cells that spread into the surrounding sinusoids and cell plates, causing the tumor boundary to be ill defined.

*Multifocal HCC*—In more than one-third of patients, HCC is multifocal, defined by the presence of tumor nodules unmistakably separated by intervening nonneoplastic parenchyma. Multifocality may be due to synchronous development of multiple, independent liver tumors (multicentric hepatocarcinogenesis) or intrahepatic metastases from a primary tumor. In the former case, the tumors may vary in histologic grade and other features; in the latter case, all the tumors are progressed lesions with advanced tumor grade. The prognosis of patients with multifocal HCC due to intrahepatic metastasis tends to be worse than in those with multicentric development of independent tumors. Patients with HCC also are at high risk for future development of new tumors. Due to the high frequency with which multiple tumors may develop, patients with HCC sometimes cannot be cured by means of surgical resection or ablation; as long as the cancer has not spread outside the liver, hepatic transplantation may provide more prolonged survival.

### 2.1.1.2 Key alteration during Hepatocarcinogenesis

Numerous pathophysiologic alterations accompany hepatocarcinogenesis, as summarized in Table 2.1.

**Table 2.1** Key Alterations during Hepatocarcinogenesis and their Imaging Implications.

| Alteration | Description | CT and MR Imaging Implications |
| --- | --- | --- |
| Angiogenesis | Unpaired (nontriadal) arteries progressively increase during hepatocarcinogenesis | Low-grade dysplastic nodules usually have similar arterial and portal venous flow as cirrhotic nodules. Hence, these nodules usually show iso enhancement relative to background liver in the vascular imaging phases. High-grade dysplastic nodules and early HCCs usually have diminished arterial and portal venous flow. Hence these nodules are usually hypo |

| | | |
|---|---|---|
| | | enhanced relative to background liver in the arterial and portal venous phases Moderately differentiated, progressed HCCs usually have elevated arterial flow with reduced or absent portal venous flow. Hence these nodules are typically hyper enhanced in the arterial phase and, although the mechanisms are not fully understood, appear to washout in portal venous and delayed phases. |
| Reduction in portal tracts | Portal tracts (which contain portal veins and nontumoral hepatic arteries) progressively diminish during hepato-carcinogenesis | Same as for angiogenesis above |
| Venous drainage | Venous drainage evolves from hepatic veins (cirrhotic nodules, dysplastic nodules, early HCCs) to sinusoids (progressed HCCs without fibrous capsules) to portal veins (progressed HCCs with fibrous capsules) | Hypervascular progressed HCCs may be associated with perinodular corona enhancement in late hepatic arterial or early portal venous phase; this is attributed to passage of contrast material from tumor through draining sinusoids and portal venules into surrounding sinusoids. Early HCCs, being drained by hepatic veins, are not associated with corona enhancement. Progressed HCCs tend to invade draining sinusoids and portal venules, leading to intrahepatic metastases. These metastases often manifest as perilesional satellite nodules in the parenchyma receiving venous drainage from the primary tumor. |
| Tumor capsule and fibrous septa formation | Progressed HCCs frequently have tumor capsules and fibrous septa. These structures are not observed in cirrhotic nodules, dysplastic nodules, or early HCCs. | The imaging detection of a tumor capsule is strongly suggestive of progressed HCC. |
| Fat content | Fat may accumulate within hepatocytes during the early phases of hepatocarcino-genesis dysplasia and early HCC). With progression to overt HCC, fat usually regresses. | In a patient with cirrhosis or other risk factors for HCC, a fatty nodule is likely to be a dysplastic nodule or an early HCC. Caveat: some progressed HCCs also may be fatty. |
| Iron content | Iron may accumulate within hepatocytes during the dysplastic phases of hepatocarcinogenesis. With progression to HCC, iron usually regresses. | In a patient with cirrhosis or other risk factors for HCC, a siderotic nodule is likely to be a dysplastic nodule and unlikely to be HCC. The development of an iron-free subnodule within a siderotic nodule, however, suggests incident HCC. |
| OATP transporters | OATP expression declines during hepatocarcinogenesis: expression levels are high in cirrhotic nodules and lowgrade dysplastic nodules and lower in many high-grade dysplastic nodules, early HCCs, and progressed HCCs | In a patient with cirrhosis or other risk factors for HCC, a solid nodule that is hypointense on hepatobiliary phase T1-weighted MR images after administration of a hepatobiliary agent is likely to be a high-grade dysplastic nodule or HCC. The differential diagnosis includes iron-rich low-grade dysplastic nodule and small intrahepatic cholangiocarcinoma. Pitfalls: hemangiomas and nodular or confluent areas of fibrosis typically appear hypointense in the hepatobiliary phase and may be mistaken for HCC. |

*Angiogenesis,* the formation and development of blood vessels, progresses during hepatocarcinogenesis. Histologically, angiogenesis is characterized by the presence of unpaired (or nontriadal) arteries and sinusoidal capillarization Unpaired arteries are isolated arteries unaccompanied by bile ducts or portal veins. These abnormal arteries are absent in cirrhotic nodules, are sometimes present in small numbers

in low-grade dysplastic nodules and are present with increasing size and number in high-grade dysplastic nodules, early HCCs, and progressed HCCs (Figure 2.5).

Physiologically, the diminution in portal tracts causes a gradual reduction in arterial and portal venous flow to the nodule, while the formation of unpaired neo-arteries increases arterial flow. The balance is such that in the early phases of hepatocarcinogenesis, there is a net decrease in intramodular arterial flow and preservation of portal venous flow, while in the later phases, portal blood flow declines and eventually becomes absent while net arterial flow increases (Figure 2.5). Thus, low-grade dysplastic nodules usually have a preserved vascular profile similar to that of background cirrhotic nodules; high grade dysplastic nodules and early HCCs tend to have diminished arterial and portal venous flow; and moderately differentiated, progressed HCCs usually have elevated arterial flow with reduced or absent portal venous flow.

*Venous drainage* evolves during hepatocarcinogenesis from hepatic veins (cirrhotic nodules, dysplastic nodules, early HCCs) to sinusoids (progressed HCCs without fibrous capsules) to portal veins (progressed HCCs with fibrous capsules). The transition to portal venous drainage may explain in part the predilection of HCC to invade into and disseminate via portal compared with hepatic veins. The metastases resulting from vascular invasion often manifest as satellite nodules within the venous drainage area of the primary tumor. The evolution in venous drainage also may explain the phenomenon of corona enhancement. The corona enhancement is an imaging feature of hypervascular, progressed HCC. It refers to enhancement of the peritumoral parenchyma that begins a few seconds after enhancement of the tumor itself. It is attributed to passage of contrast material from the tumor through the draining sinusoids and portal venules into the surrounding parenchymal sinusoids, with which the drainage vessels communicate. Early

HCCs drain via hepatic veins, not sinusoids or portal venules, and hence do not manifest corona enhancement.

*Tumor capsules and fibrous septa* are other features that develop during hepatocarcinogenesis. These structures are not observed in cirrhotic nodules, dysplastic nodules, or early HCCs but are characteristic of nodular progressed HCC, being observed in about 70% of these lesions. The capsule surrounds the tumor and consists of two layers. The inner layer is composed of tight, relatively pure fibrous tissue containing thin, slit-like vascular channels. The outer layer is composed of looser fibrovascular tissue containing portal venules, newly formed bile ducts, and prominent sinusoids. The tight inner layer is thought to acts as a physical barrier that confines cells within the tumor margin, while the narrow transcapsular vascular channels may block tumor cells that have accessed the vascular lumen from embolizing downstream. It should be emphasized, however, that capsule formation is a feature of advanced HCC; thus, while HCCs with intact capsules have a more favorable prognosis than HCCs of similar size and grade without capsules or with disrupted capsules, they have a worse prognosis than early HCCs, which are unencapsulated.

*Fat Content*—During the early phases of hepatocarcinogenesis, hepatocytes may accumulate fat, and low-grade dysplastic nodules, high-grade dysplastic nodules, and early HCCs may become more steatotic, either focally within clonal-like subnodules or diffusely than background liver. The frequency of diffuse intranodular steatosis increases from low-grade dysplastic nodule to high-grade dysplastic nodule and then to early HCC, with 40% of early HCCs being diffusely steatotic. The frequency of diffuse steatosis peaks in early HCCs about 1.5 cm in diameter and declines with increasing tumor size and grade. Thus, diffuse fatty change is uncommon in HCCs larger than 3 cm and in progressed HCCs; it usually is not observed in poorly differentiated HCC.

*Iron Content*— In cirrhotic livers without diffuse iron deposition, iron may accumulate preferentially in low-grade dysplastic nodules and some high-grade dysplastic nodules. These iron-rich nodules commonly are described as "siderotic nodules." The iron accumulation by these nodules is thought to reflect clonal expansion

of hepatocytes with iron avidity. With further dedifferentiation, hepatocytes become "resistant" to iron accumulation, and most high-grade dysplastic nodules, early HCCs, and progressed HCCs are iron free, including high-grade dysplastic foci and subnodules of HCC developing within otherwise siderotic precursor nodules. Thus, in diffusely iron-overloaded livers, a solid nodule free of iron is likely to be dysplastic or malignant.

OATP Transporters—Organic anionic transporting polypeptides (OATP) are a family of proteins expressed in hepatocytes along the basolateral (sinusoidal) membrane and involved in transport of bile salts. Emerging evidence suggests that the expression of these transporters diminishes during hepatocarcinogenesis: Expression levels are high in cirrhotic nodules and low-grade dysplastic nodules and lower in many high-grade dysplastic nodules, early HCCs, and progressed HCCs. Importantly, this suggests that OATP8 expression level decreases during hepatocarcinogenesis prior to reduction in portal venous flow and prior to complete neo-arterialization and to elevation of arterial flow (Figure 2.5), with important implications for imaging-based detection of HCC using hepatobiliary agents.

### 2.1.2 Dual Energy Computed Tomography (DECT)

#### 2.1.2.1 History of DECT

First attempts to use spectral information in computed tomography date back to the late 1970s.[15-18] At that time, two separate scans were acquired and either projection data or reconstructed data were postprocessed. However, the lacking stability of the CT density values, the long scan times which often caused patient motion between scans, the limited spatial resolution, and the difficulty of postprocessing were the main reasons why the method never achieved broad clinical acceptance.[19] With the necessity to acquire both scans separately, the use of contrast material and its differentiation by dual-energy or spectral analysis was impossible. Since 2006, dual energy CT has experienced a revival and success in clinical application. The main reason was the introduction of dual-source CT that made it possible to acquire two spiral scans simultaneously with different X-ray spectra by running the two X-ray sources at different tube voltages.[20, 21] Currently, there are several technical approaches to dual energy CT.

### 2.1.2.2 Clinical motivation of DECT[22)]

CT scanners form images of a material's linear attenuation coefficient, normalized by that of water and displayed in units called Hounsfield Units (HU).

$$\text{CT number (HU)} = 1000 \times \frac{\mu_{(material)} - \mu_{(water)}}{\mu_{(water)}} \quad (2.1)$$

where $\mu_{(material)}$ is the linear attenuation coefficient of material and $\mu_{(water)}$ is the x-ray attenuation coefficient of water.

The linear attenuation coefficient of a tissue depends on its chemical composition (effective atomic number, $Z_{eff}$), mass density ($\rho$), and the effective energy of the x-ray beam. The mass attenuation coefficient is defined as the linear attenuation coefficient of a material divided by its mass density and is dependent only on the material's chemical composition and effective x-ray energy. Generally, higher atomic number and higher mass density lead to higher measured CT numbers at a given x-ray energy. It is possible for two different materials to have the same CT numbers if one has a higher effective atomic number but the other has a higher mass density. However, while the effect of mass density on CT numbers is independent of energy, the effect of effective atomic number varies significantly with photon energy. Thus, if measurements are made at multiple energies, it is possible to decouple the influence of mass density and chemical composition on the CT number.

For materials with the same effective atomic number as water, the CT number is independent of energy and quantitatively should reflect the density difference between the material and water. This is because CT numbers are defined with respect to the attenuation of water for a given x-ray spectrum. For any other material, the CT number will be energy dependent, making the physical interpretation of the CT number at a single energy ambiguous, as it could be caused by a density or chemical composition difference. If one wants to extrapolate the measured CT number to calculate the attenuation coefficient of the material at another energy, for example to use for attenuation correction in Single photon emission computed tomography (SPECT) or positron emission tomography (PET) or for dosimetry in radiation therapy, assumptions regarding material composition would need to be made, potentially leading to erroneous results.

Dual energy CT can decompose the measured attenuation into quantities that, unlike CT numbers, are independent of the x-ray energy. For example, materials with a higher effective atomic number than water will have increased CT numbers at lower energies. Conversely, materials with a lower effective atomic number than water will have lower CT numbers at lower energies. This behavior is expected for materials with low to moderate atomic number (e.g., <50) in the diagnostic CT energy range (>30 keV). Higher atomic number materials can have their K absorption edge (K-edge) within the measured spectrum, and the discontinuity in their attenuation coefficient at the K-edge can allow very specific measurement of their concentration.

The same physical principle that causes the meaning of CT numbers at a single energy to be ambiguous also causes beam hardening artifacts. CT systems use polychromatic x-ray beams, and the photons at the various energies experience energy dependent attenuation. Calibration of attenuation with a single material allows correction for beam hardening as long as the attenuation was caused by materials of similar atomic number. When that is not the case (e.g., regions containing both soft tissue and bone), this correction is inadequate, and artifacts can result. Dual energy CT can better account for the polychromatic spectrum, allowing for improved beam-hardening correction.

Therefore, the motivation for dual energy CT includes: (a) characterization of fundamental physical quantities that determine photon attenuation (mass or electron density and effective atomic number), (b) separation of materials that may have the same CT number at a single energy, (c) improvement in quantitative accuracy, (d) extrapolation of photon attenuation to other energies (e.g., for attenuation correction of radionuclide images or radiotherapy treatment planning), (e) quantification of contrast agent concentration, perhaps even for multiple agents simultaneously, (f) characterization of materials for diagnostic specificity or image segmentation, (g) accurate correction of beam-hardening effects, and (h) increased conspicuity of iodinated contrast agent.

*2.1.2.3 Physical Principle of Dual Energy CT*

*2.1.2.3.A. Dependence of x-ray attenuation on Z, density, and x-ray energy*

Dual Energy CT relies on the fact that x-ray attenuation characteristics are energy- and material-dependent. Without the energy-dependency, attenuation data collected with different energy spectra would not provide additional information. Without the material-dependency, different types of materials could not be differentiated.

There are three types of interactions of x-ray photons with matter in the diagnostic energy range: photoelectric effect, Compton, and coherent scatter. The total mass attenuation coefficient, $(\mu/\rho)_{total}$, of a material is expressed as the summation of the mass attenuation coefficients of these interactions:

$$\left(\frac{\mu}{\rho}\right)_{Total} = \left(\frac{\mu}{\rho}\right)_{Photoelectric} + \left(\frac{\mu}{\rho}\right)_{Compton} + \left(\frac{\mu}{\rho}\right)_{Coherent} \tag{2.2}$$

The three mass attenuation coefficients have different dependencies on the input x-ray photon energy. In Fig 2.2 $\left(\frac{\mu}{\rho}\right)_{Photoelectric}$, $\left(\frac{\mu}{\rho}\right)_{Compton}$, and $\left(\frac{\mu}{\rho}\right)_{Coherent}$ for muscle tissue and cortical bone are plotted individually.
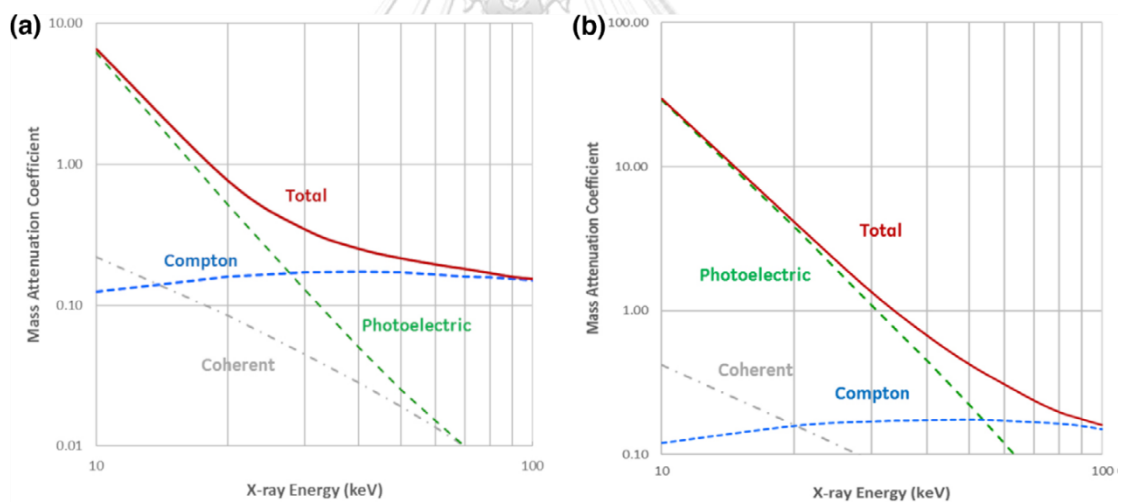


Figure 2.6 Mass attenuation coefficients for muscle (a) and cortical bone (b). Note the log-log scale and that the range of attenuation values on the y-axis differs between muscle and cortical bone.

The graph is on a log-log scale for better visualization of the full dynamic range of these coefficients. Examining the mass attenuation coefficients of muscle (Figure 2.6(a)), the following observations can be made. First, the contribution of coherent scatter is relatively small compared to either the photoelectric effect or Compton scatter in the x-ray energy range of CT. Consequently, this type of interaction is typically ignored in the

discussion of dual energy CT; only photoelectric effect and Compton scatter are considered in the theoretical derivation of dual energy CT material decomposition. It is also observed that the photoelectric effect depends strongly on x-ray energy, and at the low energy range, this interaction dominates. As the x-ray energy increases, the contribution of the photoelectric effect reduces quickly. The energy dependence of compton scatter over the x-ray energy range used in CT is much weaker. Thus, as the x-ray energy increases and the photoelectric interaction decreases, compton scatter becomes the dominating interaction. Dual energy CT takes advantage of these characteristics to perform material differentiation and decomposition.

The observations made regarding muscle also hold in the case of cortical bone (Figure 2.6(b)). In addition, there is in general a strong dependency of mass attenuation coefficients on material (or effective atomic number, $Z_{eff}$). In comparing the attenuation characteristics of muscle and cortical bone, note the difference in the vertical scale between two graphs.

### 2.1.2.3.B. Requirement for multiple unique energy measurements

To demonstrate the requirement for multiple unique energy measurements, the following example is provided. First, a tissue characterization phantom (Model 467, Gammex, Middleton, WI, USA) with a 10 mg/cc iodine/solid-water insert was placed at the 12 o'clock position and a 50 mg/cc calcium/solid-water insert was placed at the 6 o'clock position (Figure 2.7(a)). The phantom was scanned with 140 kV; the reconstructed image is shown in (Figure 2.7(b)). Visually, the two inserts are indistinguishable. Without prior knowledge, one would draw the erroneous conclusion that both inserts are made of the same material. This demonstrates that by relying solely on a single energy image, it is not always possible to separate two different materials. Given the energy-dependent nature of x-ray attenuation, when the same phantom is scanned with 80 kV, the CT numbers of the inserts are very different, as shown in Figure 2.7(c). By examining the same object with two different energies, one can differentiate materials that might otherwise look identical.

*2.1.2.3.C. Intuitive description of material decomposition*

By scanning an object at two tube potentials (different energy spectra), one can differentiate materials having different effective atomic numbers. For better visualization of this concept, consider a coordinate system with the reconstructed CT numbers measured from images acquired with two different energy spectra as the x- and y-axis, and each material plotted in this two-dimensional space. For example, the reconstructed iodine inserts with 10 mg/cc concentration scanned under 80 kV has a CT number of 400 HU and under 140 kV a CT number of 194 HU. 10 mg/cc iodine, therefore, has a characteristic coordinate of (400, 194) in the 80- and 140 kV space (dual energy space). If a mixture made exclusively of iodine and a water-equivalent material is scanned with 80 and 140 kV and has CT numbers that land on the same coordinate, one can assert, with relative confidence, that the iodine/water mixture has a concentration of 10mg/cc. If an unknown material scanned with 80 kV and 140 kV has CT numbers that land on the same coordinate, one can assert that the unknown material has the same attenuation characteristics at all x-ray energies as iodine with 10 mg/cc concentration.
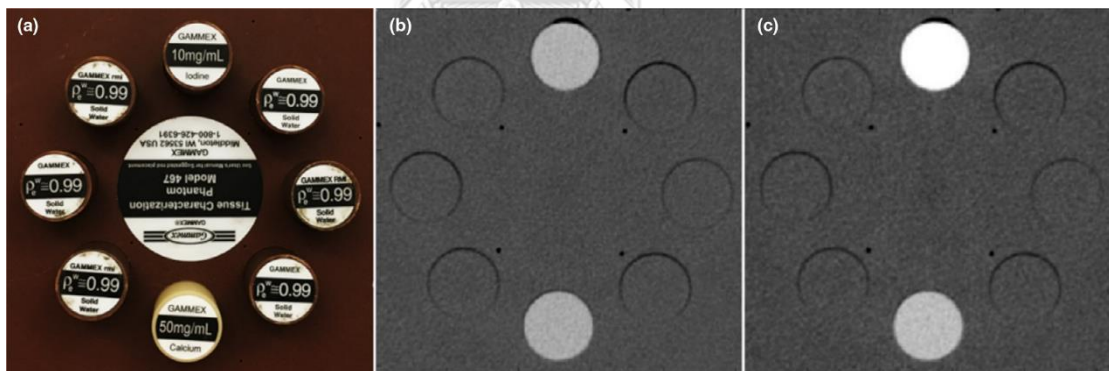


Figure 2.7 Intuitive explanation of material differentiation with dual-energy computed tomography (WW = 500, WL = 100). (a) Model 467 Gammex phantom built from their "Solid Water®" plastic-like material. (b) 140 kV image. (c) 80 kV image. Courtesy of Jiang Hsieh, PhD, GE Healthcare Technologies.

To determine whether the same material (e.g., iodine), but having different concentrations, can produce a well-recognized "signature" in this space to allow easy identification of the material, one could scan iodine inserts of different concentrations (2, 2.5, 7.5, 10, 15, and 20 mg/cc) and plot the results in the dual-energy space with the low-

kV data on the y-axis and the high-kV data *on the x-axis.*[23] as shown in Figure 2.8. These points form a straight line intersecting the origin when the background is water equivalent. Similarly, calcium inserts with different concentrations also form a straight line. However, the slopes of these lines are different. Therefore, by looking at the slope of the line formed by the measured CT numbers in the dual-energy space, one can characterize the material of interest. The slope of a line in this coordinate system is frequently referred to as the CT number ratio (CTR). When iodine is mixed not with water but with blood, as in clinical practice, the line will not intersect the origin; however, the slope of the line will be similar.
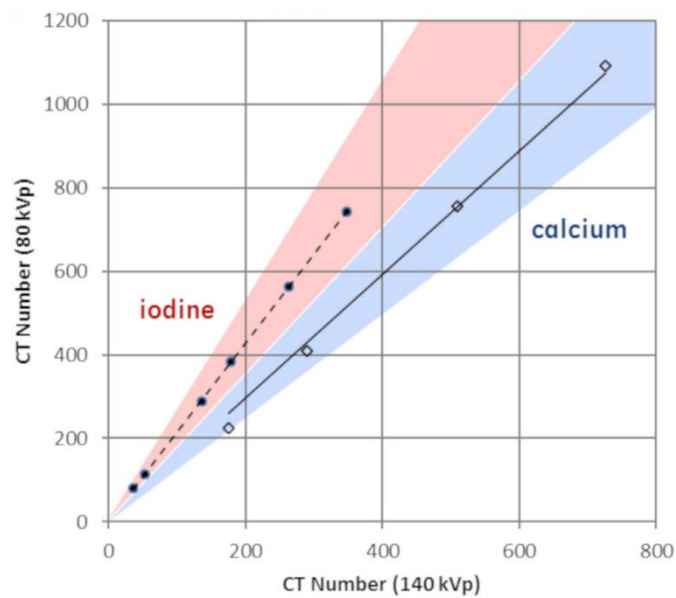


**Figure 2.8** Computed tomography number measurements of different concentrations of iodine/solid-water and calcium/solid-water inserts. Courtesy of Jiang Hsieh, PhD, GE Healthcare Technologies.

To differentiate iodine from calcium, a small zone is placed around each material's line so that any point that falls inside the zone will be classified as the same material, since noise and other nonideal properties of CT systems will produce variations in the measured CT values. An example of this is shown in Figure 2.8 (light blue zone for calcium and light orange zone for iodine). Without a priori information (e.g., system bias), a centerline is typically used to separate the two zones.

*2.1.2.3.D. Mathematical description of material decomposition*

The fundamental mathematical formulation can be traced back to 1976, with many subsequent developments having taken place since. Recalling the earlier discussion, the total mass attenuation coefficient of a particular material, $(\mu/\rho)_{total,}$ can be considered to be the linear combination of the two primary mechanisms for x-ray attenuation in the diagnostic imaging energy range: photoelectric effect and Compton scatter. Both effects are functions of the x-ray photon energy E. If we denote the mass attenuation functions due to the photoelectric effect and Compton scatter by $f_P(E)$ and $f_C(E)$ respectively, the total mass attenuation coefficient can be described as:

$$\left(\frac{\mu}{\rho}\right)(E) = \alpha_p f_p(E) + \alpha_c f_c(E) \tag{2.3}$$

where $\alpha_p$ and $\alpha_c$ represent the energy-independent contributions of $\left(\frac{\mu}{\rho}\right)_{Photoelectric}$ and $\left(\frac{\mu}{\rho}\right)_{Compton}$, respectively, to the total attenuation. Ignoring the K-edge, by $f_P(E)$ and $f_C(E)$ are known based on x-ray physics. To determine $\alpha_p$ and $\alpha_c$ we need two measurements at two different photon energies: $E_L$ (low energy) and $E_H$ (high energy):

$$\left(\frac{\mu}{\rho}\right)(E_L) = \alpha_p f_p(E_L) + \alpha_c f_c(E_L)$$

and

$$\left(\frac{\mu}{\rho}\right)(E_H) = \alpha_p f_p(E_H) + \alpha_c f_c(E_H) \tag{2.4}$$

Given two measurements and two unknowns, we can solve for $\alpha_p$ and $\alpha_c$. Each material-of-interest is now uniquely represented by $(\alpha_p, \alpha_c)$ with the photoelectric and Compton effects as the basis by which to characterize a material. If the material's K-edge has a significant contribution to the measurements, the K-edge effect needs to be included in the model and additional equations (and measurements) may be needed to solve for the unknowns.

The parametric fit model described above is known to have limited accuracy in describing real materials due to the fact that molecular interactions are ignored. It can be shown that accuracy improves by instead using attenuation functions of real materials. From a routine clinical practice point of view, decomposition into physical interaction representations photoelectric and Compton effects does not provide a direct linkage to human anatomy, pathology, or physiology, making it difficult for a radiologist to interpret

the resulting images. Since one objective of dual energy CT is to provide an easy way for radiologists to identify different materials, it is more convenient to use known-material attenuation functions as the basis of representation. For example, if water and iodine-attenuation are used as the basis functions, other materials are then represented as a mixture or linear combination of these two materials. This approach is often called material decomposition.

To accomplish this, we need to replace the photoelectric and Compton functions, $f_P(E)$ and $f_C(E)$, by the mass attenuation functions of basis materials A and B, $(\mu/\rho)_A(E)$ and $(\mu/\rho)_A(E)$ From Eq. (2.3), the two sets of functions are related by

$$\left(\frac{\mu}{\rho}\right)_A(E) = \alpha_{A,p} f_p(E) + \alpha_{A,c} f_c(E)$$

and

$$\left(\frac{\mu}{\rho}\right)_B(E) = \alpha_{B,p} f_p(E) + \alpha_{B,c} f_c(E) \qquad (2.5)$$

where $\alpha_{A,p}, \alpha_{A,c}, \alpha_{B,p}$ and $\alpha_{B,c}$ represent the contributions of the photoelectric and Compton effects for materials A and B respectively. Solving $f_P(E)$ and $f_C(E)$ for and substituting back into Eq. (2.3), we obtain:

$$\left(\frac{\mu}{\rho}\right)(E) = \frac{\alpha_p \alpha_{B,c} - \alpha_c \alpha_{B,p}}{\alpha_{A,p} \alpha_{B,c} - \alpha_{B,p} \alpha_{A,c}} \left(\frac{\mu}{\rho}\right)_A(E) + \frac{\alpha_c \alpha_{A,p} - \alpha_p \alpha_{A,c}}{\alpha_{A,p} \alpha_{B,c} - \alpha_{B,p} \alpha_{A,c}} \left(\frac{\mu}{\rho}\right)_B(E)$$

$$= \beta_A \left(\frac{\mu}{\rho}\right)_A(E) + \beta_B \left(\frac{\mu}{\rho}\right)_B(E) \qquad (2.6)$$

$\beta_A$ and $\beta_B$ are energy independent, indicating that these coefficients are valid for all energies above the K-edge of both materials (note that the K-edge effect is ignored in the formulation of $f_P$ and $f_C$). Equation (2.6) shows that the mass attenuation coefficient of a material can be represented as the linear combination of the mass attenuation coefficients of materials A and B. Materials A and B are often called the basis materials and are selected such that their effective atomic numbers $Z_{eff}$ are sufficiently different to ensure different mass attenuation characteristics.

For illustration, consider a simple example of using two materials (water and iodine) to represent the attenuation characteristics of a third material (calcium). Figure 2.9 plots the mass attenuation coefficients of three materials: water (green), calcium (red), iodine (blue), based on the National Institution of Standard and Technology (NIST) data.[24]

The three curves look significantly different in terms of their shapes, especially with the K edges of the iodine and calcium. However, if we ignore the low-energy portion (orange shaded area of E $\leq$ 33.2 keV), the three curves are quite similar. In fact, the mass attenuation coefficient of calcium can be approximated by a linear combination of the mass attenuation coefficients of iodine and water (gray dotted line) :

$$\left(\frac{\mu}{\rho}\right)_{calcium} \approx 0.835 \left(\frac{\mu}{\rho}\right)_{water} + 0.064 \left(\frac{\mu}{\rho}\right)_{iodine} \qquad (2.7)$$
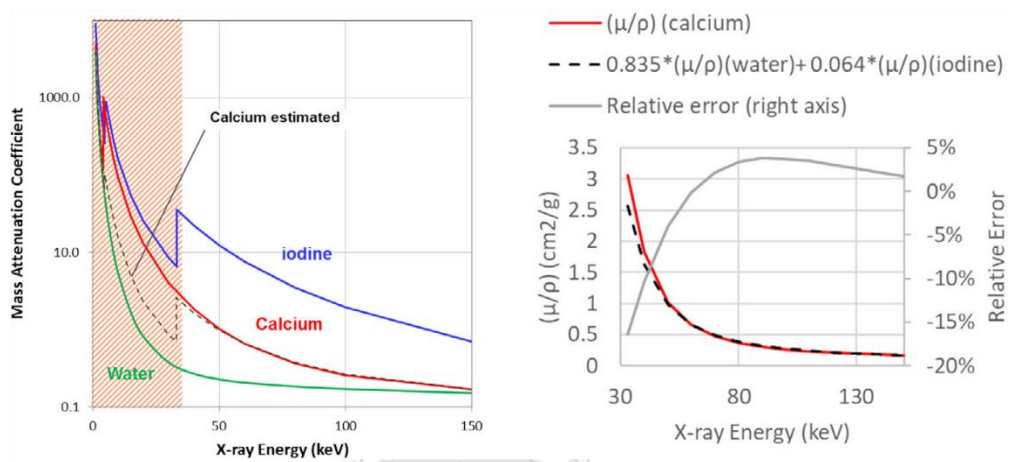


Figure 2.9 (Left) Mass attenuation coefficients of water, calcium, iodine, and the estimated mass attenuation coefficient of calcium using a linear combination of iodine and water. (Right) Mass attenuation curves of calcium, the estimated mass attenuation coefficient of calcium using a linear combination of iodine and water and water and their relative errors in the energy range of 33.2 to 150 keV.

Over the energy range of 33.2 keV < E $\leq$ 150 keV, the measured and fitted calcium mass attenuation curves overlap nicely. A significant difference does exist for the energy range below the K-edge of iodine. However, most low-energy x-ray photons are removed from the beam by the pre-patient filtration and the patient's body prior to reaching the CT detector, hence, the error caused by ignoring these low-energy photons are small.

Multiplying both sides of Eq. (2.6) by the mass density $\rho$ yields

$$\mu(E_j) = \beta_A \left(\frac{\mu}{\rho}\right)_A (E_j)\rho + \beta_B \left(\frac{\mu}{\rho}\right)_B (E_j)\rho, \qquad j = L, H$$
$$= \left(\frac{\mu}{\rho}\right)_A (E_j)\rho_A + \left(\frac{\mu}{\rho}\right)_B (E_j)\rho_B, \qquad j = L, H \qquad (2.8)$$

After acquiring two sets of data, one using a high-energy spectrum $E_H$ and one using a low-energy spectrum $E_L$, and reconstructing two images from these data sets, solving Eq. 2.8 on a pixel-by-pixel basis yields images of the mass densities of materials A and B. This process is often called image-space material decomposition since the entire process is carried out using reconstructed images.

The underlying assumption is that the reconstructed high and low-energy images are accurate and are free of confounding effects, such as beam-hardening. Since such assumption is often violated, image-space decomposition algorithms require that beam hardening and other sources of bias be carefully addressed during image reconstruction.

### 2.1.2.4 Synthetic Images from Dual energy CT

### 2.1.2.4.A. Virtual monoenergetic images (VMIs)

The results of material decomposition include energy-independent information that can be used to generate synthetic monoenergetic images, which are also referred to as virtual monoenergetic images or virtual mono-chromatic images. These images emulate the appearance of a CT study performed with a true monoenergetic photon source, for example, a synchrotron x-ray source. In principle, virtual monoenergetic images can be generated at any energy, but due to image quality limitations and other practical considerations, most dual energy CT platforms provide virtual monoenergetic images in the range 40 to 200 keV. Virtual monoenergetic images are available on all commercially available dual-energy CT platforms.

Virtual monoenergetic images are calculated by first determining the mass densities of materials A and B, using Eq. (2.8). The virtual monoenergetic image at energy $E_m$ is generated by

$$\mu(E_m) = \left(\frac{\mu}{\rho}\right)_A (E_m)\rho_A + \left(\frac{\mu}{\rho}\right)_B (E_m)\rho_B, \tag{2.9}$$

where $(\mu/\rho)_{A,B}(E_m)$ is the mass attenuation coefficient for the basis materials A and B at energy $E_m$.

It has also been demonstrated that the monoenergetic image can be generated by the weighted sum of the low- and high-energy images, that is,

$$CT(E_m) = w(E_m)CT^L + (1 + w(E_m))CT^H, \tag{2.10}$$

where "CT" is the CT number in the low (L) energy or high (H) energy image, and $w(E_m)$ is a weighting factor that depends on the desired monoenergetic energy $(E_m)$ and the effective energies of the low- and high-energy acquisitions.

Similarly, for material decomposition using the photoelectric and Compton Effect contributions, the virtual monoenergetic images can be generated by

$$\mu(E_m) = \left(\rho_p\right)f_p(E_m) + \left(\rho_c\right)f_c(E_m), \qquad (2.11)$$

where $f_p(E)$ and $f_c(E)$ are the functions describing the photoelectric and Compton mass attenuation coefficients, respectively, and $\rho_p$ and $\rho_c$ are the associated mass densities determined by the material decomposition.

Projection space decomposition generates the sinogram of basis functions, for example, the sinogram of $\rho_A$ and $\rho_B$ in Eq. (2.8), or the sinograms of $\rho_p$ and $\rho_c$ in Eq. 2.11). One can reconstruct the sinograms to create basis-material mass density images ($\rho_A$ and $\rho_B$, or $\rho_p$ and $\rho_c$) and then convert them to virtual monoenergetic images in a manner similar to the image-space method discussed above, that is, Eq. (2.9) or (2.11). Alternatively, the sinogram of the basis functions can be directly converted to the sinogram of a virtual monoenergetic image at energy $E_m$ using

$$P(\mu(E_m)) = P(\rho_A)\left(\frac{\mu}{\rho}\right)_A(E_m) + P(\rho_B)\left(\frac{\mu}{\rho}\right)_B(E_m), \qquad (2.12)$$

where $P\big(\mu(E_m)\big)$ is the sinogram of the virtual monoenergetic image; the virtual monoenergetic image is then created via CT reconstruction.

Virtual monoenergetic images provide the most accurate CT numbers at the different virtual energy levels only for the two basis materials (e.g., water and iodine, or water and bone), other materials may have with less accurate CT numbers. Virtual monoenergetic images usually have different image noise levels at different energies. A low-keV virtual monoenergetic image, for example, 50 keV, has dramatically increased noise compared with at higher energy levels, which can mitigate the benefit of increased iodine contrast in the low-keV image. CT manufacturers and investigators are continuing to develop improved algorithms to overcome this problem and make the noise more constant across the entire energy range.

*2.1.2.4.B. Material-specific or material-removed images*

The results of material decomposition, for example, $\rho_A$ and $\rho_B$ in Eq. (2.8), is a material-specific image that can be presented as the distribution map of each material's mass density. The correct unit for the pixel values corresponding to mass density is mg/cc. However, using reasonable assumptions regarding material type and measurement energy spectra, some manufacturers convert the density information into CT numbers, in Hounsfield units, by multiplying the calculated mass density by the estimated mass attenuation coefficient to determine the estimated linear attenuation coefficient, and then converting that into Hounsfield units. This serves two purposes. First, Hounsfield units are more familiar to the majority of clinical users and second, PACs systems frequently misinterpret density information and display the pixel values in Hounsfield units.

Depending on the clinical task, a variety of materials can be selected to generate material-specific or material-removed images. Common materials used are iodine and water, and their material-specific images are often referred to as iodine or water maps, respectively. Other commonly available image pairs include calcium and water images. Some manufacturers refer to images where iodine or calcium signal has been removed as virtual non contrast or virtual non calcium images, respectively.

In principle, dual-energy CT generates material-specific image pairs because two separate measurements, i.e., at low and high energies, are acquired, which is equivalent to solving for two unknowns using two equations. When there are more than two materials in the region of interest, either additional information is required, or assumptions have to be made to solve the equations. Three material decomposition algorithms often have an assumption of volume or mass conservation, that is

$$f_1 + f_2 + f_3 = 1 \tag{2.13}$$

where $f_1$, $f_2$ and $f_3$ are the volume or mass fractions of the three components. Based on volume conservation, the concept of the material decomposition can be intuitively explained as a geometric illustration in Figure 2.10. Points $\mu_1$, $\mu_2$, and $\mu_3$ locate the three basis materials in this space. A1, A2, and A3 are the areas of the triangles. The unknown

material $\mu$ lies inside the triangle ($\mu_1$, $\mu_2$, and $\mu_3$) with volume fractions of ($f_1$, $f_2$, $f_3$), so = Ai / (A1 + A2 + A3), i = 1, 2, 3.
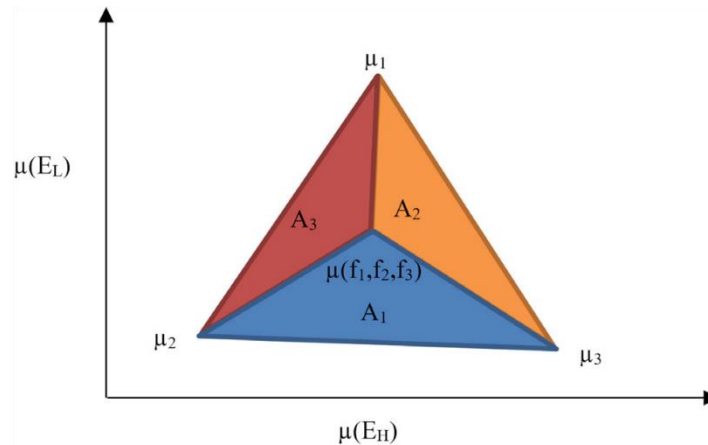


Figure 2.10 Geometric explanation of three material decomposition based on volume conservation. The horizontal axis and vertical axis are the linear attenuation coefficients in the high- and low-energy images, respectively.

Understanding the nature of the decomposed image is essential to the correct interpretation of material-decomposed images. This is particularly important since the naming conventions in commercial systems for material-specific or material-removed images imply something that is not physically accurate, namely that "iodine images" contain only iodine signal and "water" or "soft-tissue images" contain only water or soft tissue. In patients (unlike in simple iodine and water phantoms), when measured attenuation data have been decomposed into only two basis images (e.g., iodine and water), the resultant signal in a given voxel will contain signal from materials other than the iodine and water basis materials (e.g. fat or bone) that are physically present in that voxel. A common misconception is that measurements of iodine concentration in the iodine image are equal to the actual physical mass density (i.e., concentration) of iodine. Instead, all materials present, except those having attenuation properties equivalent to water, will contribute some signal to the iodine map. Likewise, all materials present, except those having attenuation properties equivalent to iodine, will contribute some signal to the water map.

Understanding this principle explains why bone is visible in the "iodine map," and why the CT number of fat in the water or soft-tissue image (commercially referred to as a "virtual non contrast (VNC)" image) is different than in a conventional true non contrast image. For a water-iodine decomposition, the presence of bone or fat violates the assumption that only water and iodine are present in the image, neither of which are equivalent to bone or fat in terms of attenuation properties as energy is varied. Thus, bone or fat attenuation is represented partially in the "iodine-removed" or VNC image and the remaining component of bone or fat attenuation is represented in the "water-removed" image. Hence, bone will appear in both the "iodine image" and the "water or soft-tissue image." Also, since the VNC image accounts for only a portion of the fat attenuation, fat in a VNC image will have a different CT number than fat in a true non contrast CT image. Of note, the decomposition may generate negative mass density values for fat, which although reasonable from a mathematical perspective, may be difficult to explain to clinical users. Thus, some CT manufacturers choose to set negative fat mass density values to zero.

### 2.1.2.5 Technical Implementation of Dual Energy CT

### 2.1.2.5.A. Detector-based methods

2.1.2.5.A.1. Dual-layer detectors

*Description of technology:* Acquisition of two spectrally distinct data sets can be achieved using a single x-ray source and two layers of energy-integrating scintillator detectors. The thickness and material of each layer determines the energy separation and relative noise of the recorded low- and high-energy datasets. In a commercially available system (IQon, Philips Healthcare, Cleveland, Ohio, USA), the x-ray tube generates a polychromatic beam with a maximum photon energy equal to the peak tube potential selected by the user. Low-energy photons from the generated x-ray spectrum are selectively absorbed by the top low-density garnet scintillator layer, while high-energy photons pass through the top layer and are absorbed by the bottom Gadolinium Oxysulfide ($G_2O_2S$) layer (Figure 2.11).

Conventional CT data are also available from every scan by adding the low- and high-energy data together and reconstructing using standard techniques such as iterative reconstruction or filtered back-projection. The resulting images are conventional single-energy CT images, matching those obtained from conventional CT scanner operated with a single x-ray tube, single tube potential, and single-layer detector.

Ideally aligned low- and high-energy data are available from every scan performed at 120 or 140 kV. Intrinsic registration of spectral data allows projection domain decomposition. Reconstruction of basis pairs is performed with a dedicated spectral algorithm. Material characterization and decomposition is performed using basis images to create various spectral image types (Figure 2.11).
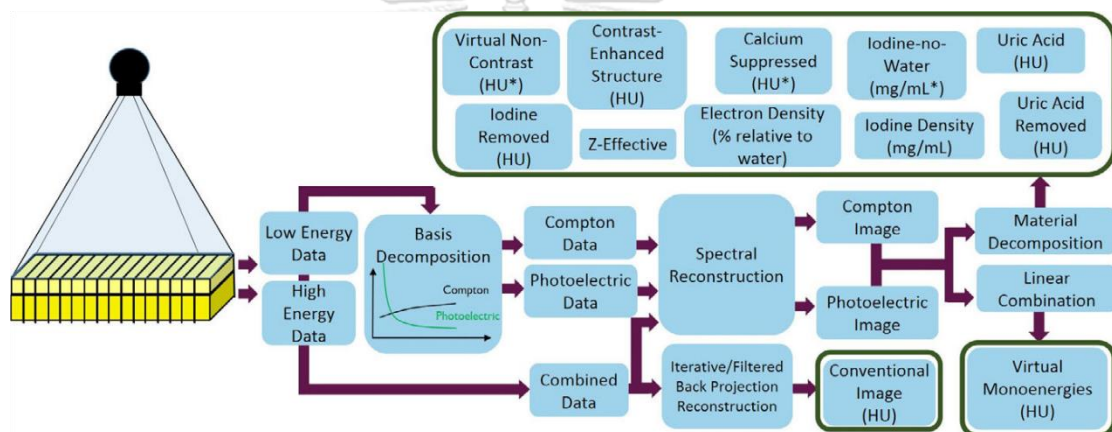


**Figure 2.11** Illustration of acquisition and reconstruction workflow for dual-layer detectors technology.

Diagram in Figure 2.11 shows simultaneous acquisition of low and high energy x-ray spectra data allows for projection-based spectral decomposition of the data into individual basis components with differing energy dependencies, specifically photoelectric effect, and Compton scatter components. After decomposition, the data are reconstructed to obtain basis pair images. The photoelectric and Compton basis pair images can then be processed to obtain several types of spectral images, including both attenuation-based and on attenuation-based images. Low- and high-energy data can also be combined to create conventional (e.g., 120 kV) images. Asterisk (*) indicates that original pixel values may be modified significantly in some areas due to suppression of a particular material.

*Strengths:* One of the strengths of dual-layer detector technology is the absence of special protocols for dual-energy scanning. Routine scan protocols can be used "as is" without increasing dose or changing workflow. Both conventional and dual-energy data are available from every 120 and 140 kV scan and the need for dual-energy derived images does not have to be identified a priori. This can be particularly helpful for salvaging studies with suboptimal contrast enhancement, reducing artifacts on conventional images that obscure the region of interest, and improving lesion visualization and characterization, including incidentally discovered lesions.

Energy separation at the detector level yields low- and high energy datasets that are spatially and temporally aligned, permitting projection space decomposition. A benefit of projection space decomposition is the intrinsic reduction in beam hardening artifacts. This registration of spectral data also allows the identification and removal of anti-correlated noise in basis material raw data sets, facilitating noise suppression while preserving signal. Decreased noise in virtual monoenergetic images compared to conventional images created from the same data has been achieved using dual-layer technology.

Another strength of dual-layer detector technology is that it imposes no constraints on data acquisition related to field of- view, gantry rotation time, or the utilization of dose saving tools such as tube current modulation. Additionally, the thickness and material of each detector layer can be chosen to provide low- and high-energy data with matching noise levels across typical patient sizes. This criterion is commonly used to balance the noise levels between the two data sets, as this provides a reasonable approach that is relatively robust for multiple applications. Moreover, the dual-layer solution is free from additional problems such as patient-induced cross scatter found in the dual-source approach and the reduction in spatial resolution due to the view interpolation required in the tube potential switching approach.

*Limitations:* The use of dual-layer detector technology with a single x-ray source has some limitations for dual energy CT. Because the energy separation of spectral data sets is limited by the fixed detector design, only scans performed at a tube potential of

120 or 140 kV may be used for spectral analysis. Routine scans can be performed at 80 or 100 kV, but only a conventional data set is available for reconstruction. The spectral separation with dual-layer detectors is worse than with approaches using two different tube potential settings and filtration of one of the beams, which in principle will require a higher radiation dose to the patient to achieve an equivalent CNR in spectral images. This is somewhat mitigated by the removal of anti-correlated noise during material decomposition in projection space.

Another limitation of dual-layer detectors is the doubling of electronic noise since each reading is based on two channels of data. The detector design and operating parameters of the electronics help to minimize the impact of electronic noise. The electronic noise contribution typically remains below the quantum noise contribution such that the latter typically defines the limits of low dose scans. Finally, detector crosstalk between layers can occur, whereby photon interactions in one detector pixel result in scattered photons that interact in a different pixel.

### 2.1.2.5.A.2. Energy resolving, photon counting CT

*Description of technology:* Energy integration versus photon counting: The solid-state scintillation detectors used in today's medical CT systems convert x-rays into visible light, which is detected by photodiodes coupled to the scintillators. The intensity of the light produced per absorbed x-ray quantum and, as a consequence, the electrical signal produced per absorbed x-ray quantum, are proportional to the x-ray energy $E$. The signal $S_{int}$ in the energy integration detector is the integral of the signal from all absorbed x-ray flux $N(E)$ over all energies $E$, with a weighting factor proportional to $E$.

$$S_{int} \approx \int_0^\infty E \cdot N(E) dE \qquad (2.14)$$

Solid-state scintillation detectors do not provide energy-resolved signals. Low-energy x-ray quanta, which carry most of the low-contrast information about an object, particularly iodine containing tissues, are therefore given less weight than are high-energy quanta in the integrated signal.

Photon-counting detectors based on semiconductors such as cadmium-telluride (CdTe) or cadmium-zinc-telluride (CZT) directly convert the x-rays into an electrical signal.

The absorbed x-rays create electron-hole pairs that are separated in a strong electric field (voltage ~ $10^6$ V/m) between the cathode and pixelated anode electrodes on top and at the bottom of the detector, respectively (Figure 2.12). The moving electrons induce short voltage pulses, with pulse-heights approximately proportional to the x-ray energies $E$, which are individually counted as soon as they exceed a given energy threshold.

In a basic operation mode, with just one energy threshold $E_1$, all x-ray quanta above this threshold energy are counted with the same weight, resulting in a detector signal.

$$S_{count} \approx \int_{E_1}^{\infty} 1 \cdot N(E)dE \qquad (2.15)$$

The absence of the down-weighting of the signal from low-energy x-ray quanta can improve the CNR of the resultant images, in particular in CT scans using an iodinated contrast agent. Since only signals above the energy threshold are detected, low level electronic noise below the threshold does not affect the count rates in photon counting detectors. This is a major difference from conventional energy-integrating detectors, resulting in less image noise and the potential for dose reduction in scans of obese patients or in scans acquired at very low radiation dose.

As illustrated in Figure 2.12, different energy thresholds allow for the discrimination of photon energy. Photon counting detectors can simultaneously provide CT data with different lower energy thresholds $E_1$, $E_2$, to provide spectrally resolved measurements. Physically, the thresholds are realized by different voltages that are fed into pulse-height comparator circuits. The pulse heights obtained from the detector are nearly proportional to the energies of the detected x-ray photons. Up to six different threshold values have so far been used in prototype settings.

*Strengths:* By implementing two or more energy thresholds for data read-out, photon counting detectors can provide spectral (dual- or multi-energy) data using standard CT scanners without modifications other than the detector type. Spectral information is available in any scan, with no limitations in the choice of scan parameters such as tube potential, gantry rotation time or pitch, or in the use of anatomical tube current modulation to adapt the radiation dose to the patient's anatomy. The inherent

spatial and temporal alignment of the CT data at different energy levels benefits scans of moving organs, such as the heart, and enables the use of projection-based material decomposition. There is no additional scattered radiation that needs to be taken care of, such as the cross-scatter in dual source CT. With photon counting detectors, spectral data are routinely acquired, with the images at the lowest energy threshold used for standard diagnosis (similar to today's single energy CT images), and spectral information retrospectively available if clinically needed.
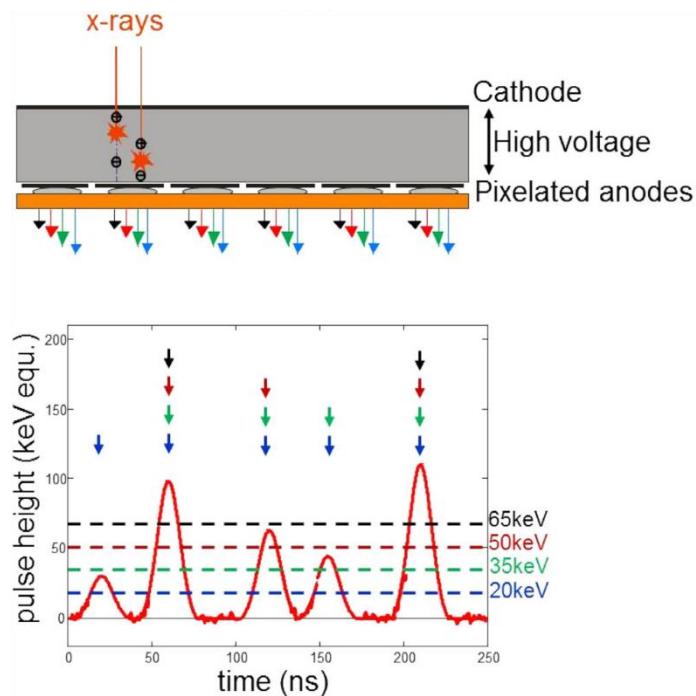


Figure 2.12 Schematic drawing of a direct-converting photon counting detector (top) and the x-ray photons are counted in the respective energy bins as soon as they exceed the corresponding energy thresholds (bottom).

A technique referred to as K-edge imaging can be used to decompose materials into more than two basis materials (where one undergoes primarily Compton scattering interactions and the other undergoes primarily photoelectric interactions). Specifically, higher atomic number materials that have K-edges within the diagnostic CT energy range can be used as additional basis materials because their absorption edge discontinuities differentiate these materials from linear combinations of non-K-edge materials.

*Limitations:* main limitation of photon counting detectors today is the finite pulse-width of the detected x-ray pulses, which currently have a full-width-at-half-maximum (FWHM) of 10 ns and more. This leads to pulse pile-up at high x-ray flux values, as is common in medical CT. Pulse pile-up results in overlapping low-energy pulses being incorrectly registered as a fewer number of high-energy pulses, or several overlapping pulses being counted as only one pulse. As a consequence, photon counting detectors can saturate at high x-ray flux values, leading to significant quantum losses and increased image noise.

Another problem is count-rate drift. Non-homogeneously distributed crystal defects in the sensor material can cause trapping of electrons and holes, a build-up of space charges, and a modification of the electric field distribution. This changes the characteristics of the signal pulses in the individual detector elements and may lead to severe ring artifacts in images at higher flux values. Significant progress has been made in reducing count-rate drift to acceptable levels.

The spectral separation of photon counting detectors is affected by unavoidable physical effects, such as signal splitting at pixel borders (charge sharing) or energy loss of the x-ray quanta due to K-escape. K-escape occurs due to preferential absorption of photon energies near the K-edge(s) of the detector material and the consequential release of characteristic x-rays. Charge sharing and K-escape events lead to a double counting of x-ray quanta at the wrong energies and therefore to a reduction in spectral separation.

### 2.1.2.5.B. Source-based methods

*2.1.2.5.B.1 Consecutive volume or helical acquisitions with different tube potentials per rotation*

*Description of technology*: Wide-volume dual-energy imaging using two consecutive acquisitions takes advantage of the extended z-axis coverage available in a single axial rotation with wide-area detectors, such as the 16-cm Aquilion ONE detector introduced by Toshiba Medical Systems in 2009. In standard imaging applications, a 16-cm detector provides isotropic volume coverage of entire organs or regions of interest in a single 0.275 s gantry rotation. For dual-energy applications, full organ coverage using

two gantry rotations at the same location, each at a different tube potential value, allows for projection space alignment and projection data-based material decomposition. When longer scan lengths are required, two helical scans performed with the identical trajectory may also be used. The noise level of the low- and high-energy acquisitions are controlled independently by adjusting the tube current value when the tube potentials are switched.

*Strengths:* A strength of the wide-area detector, two consecutive rotations approach to dual-energy CT is alignment of the projection space data, provided that there is no patient motion between the two gantry rotations. In addition, this approach lets the user take advantage of the automatic exposure control (AEC) system to adapt the tube current according to patient attenuation. This allows the image noise level to be matched between the low- and high-energy data acquisitions. Finally, this approach has stable tube potential values over the duration of the acquisition.

*Limitations:* The main limitation of the two consecutive acquisition approach to dual energy is motion misregistration and temporal alignment, as it can take as long as 500 milliseconds to switch from one tube potential to another between acquisitions. This limits its use in patients who move between acquisitions, in anatomic regions that undergo significant movement between acquisitions, such as in cardiac applications, or for tissues with rapid changes in contrast concentrations.

*2.1.2.5.B.2 Acquisitions with rapid tube potential switching*

*Description of technology:* The collection of low- and high-energy data sets by rapidly switching the tube potential back and forth between the low and high settings is often referred to as fast-kV switching. The switching of the tube potential enables the acquisition of data from two different energy spectra that are closely aligned temporally and spatially. The first commercial scanner for routine clinical imaging using fast-kV switching was introduced by GE Healthcare in 2008 (Discovery CT750 HDTM). In fast kV switching, the x-ray tube potential is switched on a view-to-view basis. The acquired projection dataset is an interleaved sinogram, as shown in Figure 2.13. Due to the temporal offset of the low- and high-energy projections, data interpolation is used to achieve data consistency between the low- and high energy projections so that

projection-space material decomposition can be performed. To maintain spatial resolution and reduce view-aliasing artifacts, the number of views collected per gantry rotation is more than doubled compared to a single tube potential scan. At a typical clinical rotation speed, the tube potentials, and therefore the output x-ray spectra, are changed within a fraction of a millisecond between 80 and 140 kV.

When more than two thousand views are collected per gantry rotation, the angular difference between adjacent 80- and 140-kV projections is smaller than 0.18°. This ensures that the neighboring views collected with different tube potentials correspond to the same patient anatomy viewed at nearly the same orientation. The adjacent views are also collected within a fraction of a millisecond to ensure that patient anatomy is minimally changed due to patient motion. These two properties allow the material decomposition to be carried out in the projection-space.

The image generation process is as follows. The original interleaved 80- and 140-kV projections are sorted into two sinograms: 80 and 140 kV. Projection-space material decomposition is carried out and water (iodine)- and iodine (water)- density projections are generated. (On the GE system, the first material listed is the basis material being displayed and the material listed within the parenthesis is the other basis material used for the two-material decomposition). Tomographic reconstruction is then applied to these projections to produce water (iodine)- and iodine (water)-density images. Other images, such as virtual monoenergetic images, different basis-material pairs, or effective atomic number images can be calculated from the water and iodine pair. The entire process is pictorially depicted in Figure 2.13.
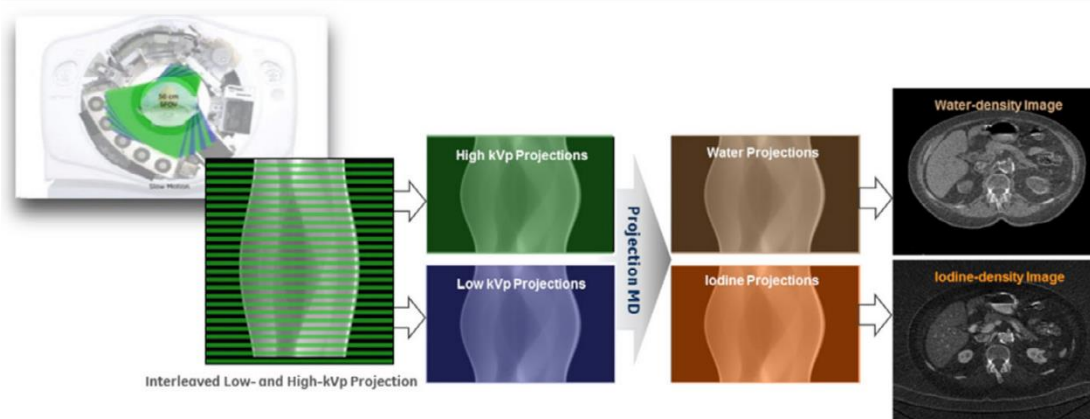
**Figure 2.13** Illustration of fast kV switching, material decomposition and image reconstruction process.

Strengths: Since projection-space material decomposition is used in fast-kV switching, beam-hardening induced artifacts can be significantly reduced, which is important for accurate dual-energy material quantitation. Furthermore, the fast-kV switching technique results in nearly simultaneous acquisition of the low- and high-energy projections, ensuring that motion-related issues are minimized. Since both sets of projections are acquired with the same detector used for routine CT imaging, the entire 50 cm field-of-view is covered (this is true for any detector-based methods if the detector(s) cover a 50 cm field-of-view). Finally, the ability to independently adjust the measured low- and high-energy flux based on the integration time for each energy's projections enables optimization of the system noise performance by taking into consideration the difference in patient attenuation characteristics between the two tube potentials.

Limitations: In the current commercial implementation of the fast kV switching, the x-ray tube current cannot be changed dynamically during data acquisition. Hence, tube current modulation is not possible, which decreases the dose efficiency of the examination and limits the ability of the system to adapt to regions of increased patient attenuation. However, this is mainly due to hardware limitations on the existing system and is not a fundamental limitation of the fast kV switching technology.

Both the finite switching time between the low and high tube potential settings and the finite detector temporal response introduce signal contamination between the low and

high-energy measurements, which reduces the accuracy of material quantitation and increases noise in images based on material decomposition. This contamination worsens as gantry rotation time is decreased, so the system software currently prevents the use of gantry rotation times of less than approximately 500 ms, which may limit the quality of cardiac examinations.

Additionally, because a single x-ray tube is used to collect all projection data and only a very short time exists between the acquisition of the low and high energy projections, further optimization of spectral separation by adding prefiltration to the high-energy beam would be difficult to achieve in practice, as it would require a system to move the filter into and out of the beam at extremely high rates and in a manner that was perfectly synchronized with the kV switching. Therefore, the energy separation for kV switching is worse than that of the dual-source approach, which allows the use of different beam filtration for the x-ray tube operating at the lower tube potential and the x-ray tube operating at the higher tube potential.

*2.1.2.5.B.3. Beam filtration techniques*

*Description of technology:* In 1980, a simple technique for obtaining dual-energy information from a standard CT acquisition was described. The authors proposed to filter the two halves of the x-ray fan beam differently and use a 360° scan to obtain complete projection data for both spectra. This method has been implemented in a commercial CT scanner (SOMATOM Edge and SOMATOM go. All, Siemens Healthcare GmbH, Forchheim, Germany). The x-ray beam, however, is now split in the longitudinal direction and not in the fan beam direction. This is possible because of the multirow detector geometry, which was not available in 1980. Two different prefilters in the tube collimator housing are used to split the beam (Fig. 2.10). One half of the multirow detector in the scan direction sees an x-ray beam filtered with 0.6 mm tin; compared to the standard 120 kV spectrum, the mean energy of this prefiltered spectrum is increased. The other half of the detector sees an x-ray beam filtered with a thin gold filter; as a consequence of the K-edge of gold at 80.7 keV, the mean energy of this spectrum is decreased with respect to

a conventional 120 kV spectrum. The total attenuation of the prefilters is adjusted to balance the radiation dose of the low- and high-energy portions of the beam.

The CT system may be operated in a spiral (helical) scan mode with a gantry rotation time as fast as 0.28 s and with pitch values up to 0.5 (referring to the full z-width of the detector). In this manner, each half of the detector along the z axis acquires a complete spiral dataset, and both low- and high-energy images can be reconstructed at any z-position as an input into image-based material decomposition techniques.
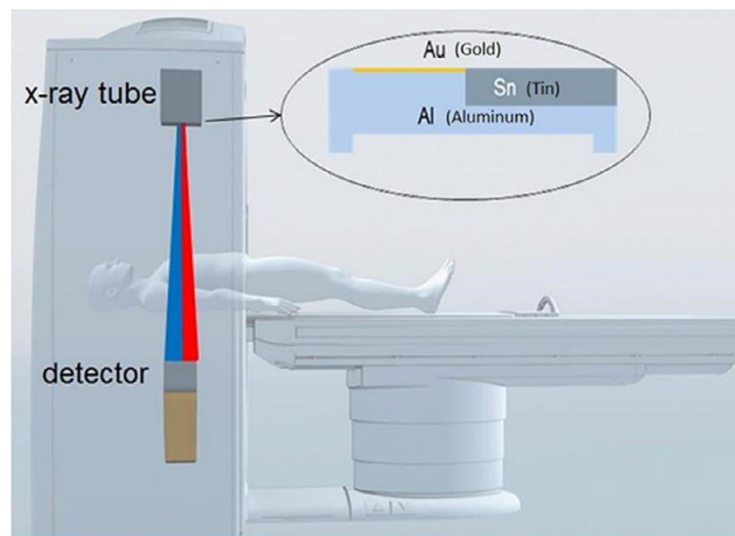


Figure 2.14 Principle of a dual-energy computed tomography acquisition technique that uses a beam filter in the tube collimator housing to split the x-ray beam in the longitudinal direction.

*Strengths:* Beam filtration techniques enable dual-energy scans with standard CT systems, with only small modifications of the tube collimator. No special tube or generator requirements are necessary. The dual-energy information is obtained over the full 50 cm diameter scan field of view and the radiation dose to the patient can be optimized by means of anatomical tube current modulation. A mixed image (a weighted average of low- and high-energy images that simulates a standard 120-kV image) dataset is the primary output of the acquisition. This enables routine dual-energy CT scanning while providing data similar to conventional imaging protocols. Compared with single-energy CT, similar image noise in the mixed images was demonstrated at 17% lower radiation dose.

*Limitations:* The spectral separation with beam filtration techniques is not as good as when two different tube potential settings are used. Furthermore, a powerful x-ray tube is required because the prefiltration absorbs a significant portion of the x-ray flux, in turn limiting the use of this technique to nonobese patients. The maximum spiral pitch of 0.5 somewhat limits maximum volume coverage speed, albeit the use of 0.28 or 0.3 s rotation times can usually compensate for this limitation. Finally, scattered photons from the low-energy spectrum can be detected and counted as originating from the high-energy spectrum, and vice-versa.

*2.1.2.5.B.4. Dual-source acquisitions*

*Description of technology:* A dual-source CT (DSCT) is a CT system with two measurements systems, i.e., two x-ray tubes and two corresponding detectors, offset within the gantry at an angle of about 90°. Both measurement systems acquire scan data simultaneously at the same anatomical level of the patient (same z-position) (Fig. 2.11). Dual energy data can be acquired by simultaneously operating both x-ray tubes at different tube potential settings, for example, 80 and 140 kV.
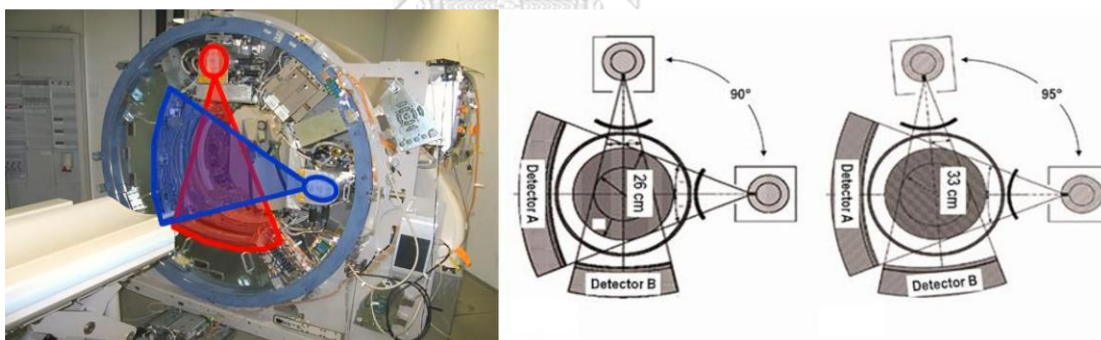


**Figure 2.15** Open gantry of a 1st generation dual source computed tomography (CT) left). Schematic drawing of the tube-detector configuration of a 1st generation dual-source CT (DSCT) (center) and a 2nd generation DSCT (right), which has an increased scan field of view for detector B (right).

In 2006, the first DSCT was commercially introduced (SOMATOM Definition, Siemens Healthcare GmbH, Forchheim, Germany). Its two acquisition systems, A and B, were mounted onto the rotating gantry with an angular offset of exactly 90°, this was changed to an angular offset of 95° for the 2nd and 3rd generation DSCT systems (Fig. 13).

Detector A covers the full scan field of view of 50 cm diameter, while detector B is restricted to a smaller field of view of 26 cm (1$^{st}$ generation), 33 cm (2$^{nd}$ generation), or 35.6 cm (3$^{rd}$ generation), as a consequence of space limitations on the gantry.

*Strengths:* With DSCT systems, the scan parameters (e.g., tube current and potential) can be individually adjusted for both measurement systems, resulting in a balanced radiation dose distribution between the low- and the high-energy scans. A wide range of routine scan protocols is available, with no restrictions in the choice of scan parameters such as gantry rotation time. Use of anatomical tube current modulation allows adaptation of the radiation dose to the patient's anatomy. Mixed images (a weighted average of low- and high-energy images) are routinely available, allowing dual-energy CT scans to be performed in routine clinical practice similar to conventional imaging protocols, with dual-energy information available when needed.

DSCT systems have the further ability to optimize spectral separation by introducing additional prefiltration into the high-energy beam, e.g., by means of a filter that can be moved into the beam when needed and moved out for nondual- energy applications. Dual-energy CT image quality and quantitative accuracy increases with better separation of the energy spectra. Energy separation results in increased image noise in basis-material decomposition, which has to be compensated for by increased radiation dose. The 2$^{nd}$ generation DSCT is equipped with a 0.4 mm thick tin (Sn) filter to shift the mean energy of the 140 kV spectrum from 86 to 97 keV (after 20 cm water), as illustrated in Figure 2.16. The mean energy of the 80 kV spectrum is 60 keV. The 3$^{rd}$ generation DSCT provides a 150 kV x-ray tube potential with more aggressive tin prefiltration (0.6 mm) to shift the mean energy of the 150 kV spectrum to 107 keV (Figure 2.12). As additional benefits, the tin filter narrows the high energy spectrum, resulting in better dose efficiency and less beam hardening artifacts.

CTR can be used to quantify the performance of a dual energy CT acquisition technique with regard to energy separation and material differentiation capability. The CTR for iodine, a commonly used basis material for material decomposition in contrast-enhanced CT scans, increases from ~2 using the 80/140 kV x-ray tube potential

combination to ~3.4 using the 80/150 kV with 0.6 mm tin prefiltration x-ray tube potential combination (measured using a 20 cm water phantom). A larger CTR value results in better-conditioned equations for basis-material differentiation and leads to less image noise in the material-specific images. Alternative metrics to indicate the material differentiation capability of a dual-energy CT system include dual-energy index (DEI), dual-energy ratio (DER), and LAR, some of which take into account the effect of the background material, can be found in the literature.
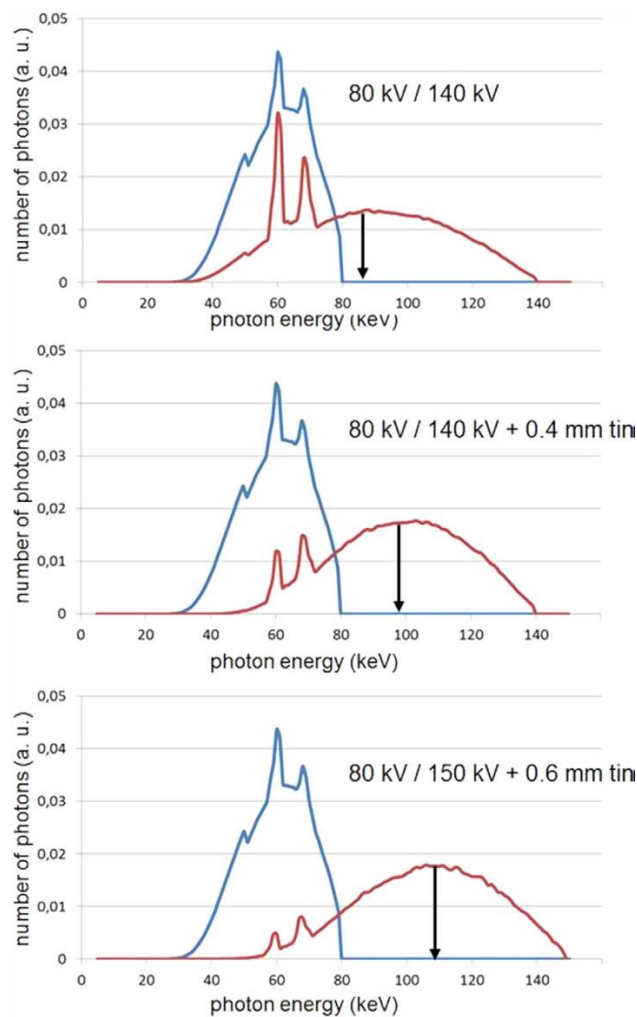


**Figure 2.16** Typical 80 and 140 kV spectra (after 20 cm water), normalized to equal areas under the curves (top). 80 kV spectrum and 140 kV spectrum with additional 0.4 mm tin prefiltration (center), and 80 kV spectrum and 150 kV spectrum with additional 0.6 mm tin prefiltration (bottom).

*Limitations:* Dual-energy evaluations with DSCT are restricted to the smaller central scan field of view of the smaller detector B. Mixed images, however, are obtained over the full 50 cm scan field of view.

Projection-based dual energy algorithms cannot be used with DSCT because the low- and high-energy projections are not simultaneously acquired at the same z-position. Dual energy algorithms are therefore image based. While there exists a theoretical advantage to projection-based algorithm, image-based methods have been shown to be practically equivalent for certain clinical tasks. One prerequisite is the validity of the thin absorber model. With water and iodine as basis materials, the maximum x-ray attenuation of the iodine along any measured ray path must be small enough to assume a linear contribution to the total attenuation. This holds for iodine samples with integrated attenuation up to ~5000 HU•cm in water and is violated only in clinical situations where extremely high local concentrations of iodine are present, such as in CT nephrographic50 or cardiac studies. As a second pre-requisite, the CT number of water and the CT numbers of small iodine samples should be independent of their position within the scanned object. To create these conditions, DSCT scanners are equipped with optimized bowtie filters to obtain adequate beam hardening. The patient, however, must be centered within the scan field of view.

Finally, cross-scattered radiation, i.e., scattered radiation originating from tube A and detected by detector B, and vice versa, has to be carefully corrected for to avoid distortions of CT numbers by cupping or streaking artifacts. This can be done either by measurement of cross-scattered radiation or by model-based approaches.

### 2.1.3 Image quality assessment in CT.[25]

The rapid development and complexity of new x-ray computed tomography (CT) technologies, the increased utilization of CT, and the need for evidence-based optimization of image quality with respect to radiation and contrast media dose call for an updated approach to evaluating the performance of CT systems. In light of the availability and increasing clinical use of new CT technologies, it is particularly important to assess

image quality using task-specific metrics that are more relevant to predicting the performance of a CT system and protocols for clinical imaging tasks.

### 2.1.3.A. Task Transfer Function (TTF)

When the imaging system is known to behave nonlinearly (e.g., in the case of iterative reconstruction), a measured modulation transfer function (MTF) may not represent the imaging system's response to an arbitrary input object (as would be the case for a truly linear system). In this scenario, the system resolution becomes dependent on the object contrast and background noise level. Therefore, the MTF is not general but rather "task-specific" and is denoted as a TTF. A TTF is measured in identical fashion as an MTF. However, when reporting a TTF, the background noise (pixel standard deviation, SD), object's contrast, and object's radial location should be included. Denoting the MTF as the TTF emphasizes that the system resolution is influenced by those factors. This emphasis becomes important when computing task-based performance or when comparing resolution between different imaging systems or conditions. Traditionally, an MTF is measured using high-contrast objects, while a TTF should be measured for objects of a contrast that represents the imaging task under study.

The technique for estimating both the in-plane and z-direction TTF from the CT ACR 464 phantom is illustrated in Figure 2.17. The in-plane TTF is measured based on a circular region of interest (ROI) around one of the rods in module 1. From this ROI, it is possible to identify the center of the rod, and then calculate the distance of each pixel in the ROI from the center. The plot of HU values vs. distance makes up the edge spread function (ESF) (bottom left). The data points in the raw noisy ESF (blue dots) are binned and averaged to achieve a smooth ESF (red line). The derivative of the smooth ESF is estimated to get a line spread function, which is then Fourier transformed to get the task transfer function (bottom right). The TTF curves can be summarized by the spatial frequencies at which the TTF reaches 50% and 10%, denoted as $f_{50}$ and $f_{10}$, respectively. Various free software resources are available to assist with these analyses.

In this method,[26-28] a circular ROI with a radius about twice that of the phantom rod is roughly centered about the rod. The exact center location of the rod is estimated in

each image by finding the maximum of the cross-correlation between the image data and an idealized image of the phantom rod at upsampled resolution (to allow higher precision in center identification).
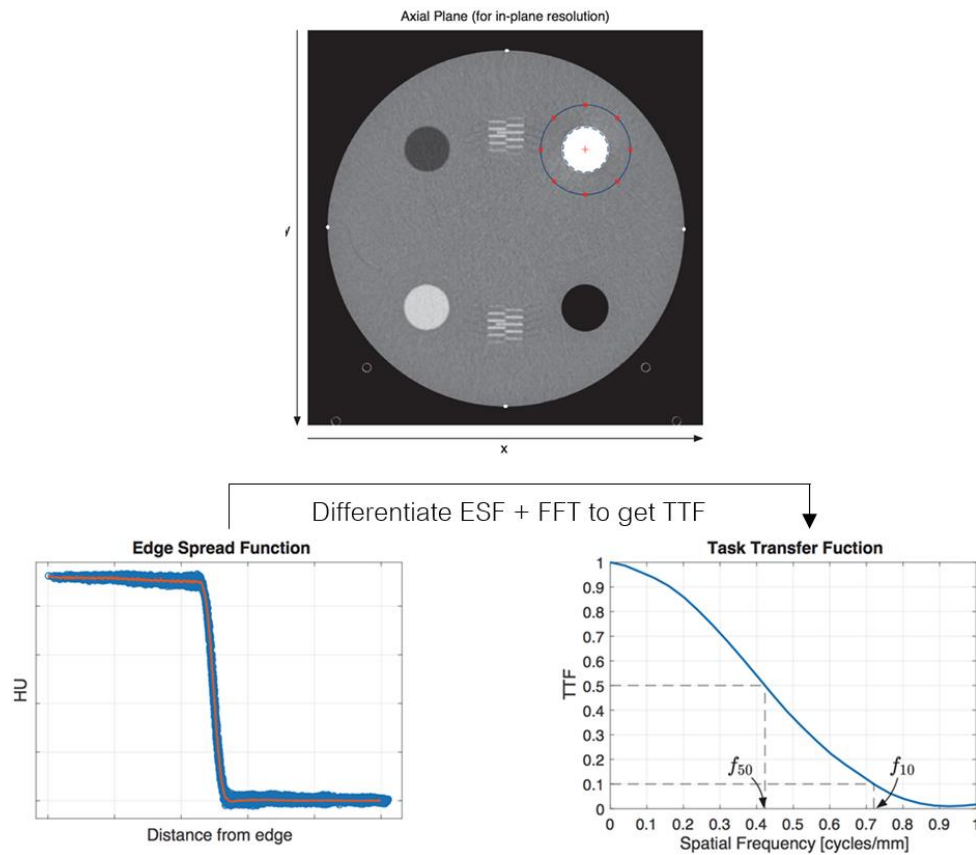


Figure 2.17 The technique for estimating both the in-plane and z-direction TTF from the CT ACR 464 phantom.

The precise center location of the rod is estimated for each image, and each pixel's radial distance from the center is calculated. An ESF is then generated by binning and averaging pixel CT numbers as a function of radial distance. Radial bin widths of $1/10^{th}$ the image pixel size are recommended. The derivative of the ESF is taken to yield the LSF. The TTF is finally computed as the magnitude of discrete Fourier transform of the LSF (normalized by the DC component). Once the TTF is computed, the 50% and 10% frequencies ($f_{50}$ and $f_{10}$) can be determined and used to summarize the system resolution under the given acquisition/reconstruction conditions. It is also important to report the contrast and noise conditions under which the TTF was measured.

*2.1.3.B. Noise Power Spectrum (NPS)*

To characterize noise and noise texture of the CT system under reference conditions and establish baseline values for targeted imaging conditions with methods applicable to both linear and nonlinear reconstruction algorithms.

- Noise magnitude: standard deviation (SD) of pixel values

- Noise texture: visual impression of the image noise (e.g., fine or coarse). CT images have a distinct noise texture as a result of the noise correlations introduced in the image reconstruction process. The noise texture has a large impact on the perceived quality of a CT image and can be quantitatively characterized by the noise autocorrelation or the noise power spectrum.

- Noise Power Spectrum (NPS): Fourier transform of the noise autocorrelation, describing the distribution of noise variance in terms of spatial frequencies. Noise stationarity is assumed for computation of the NPS from the noise autocorrelation.
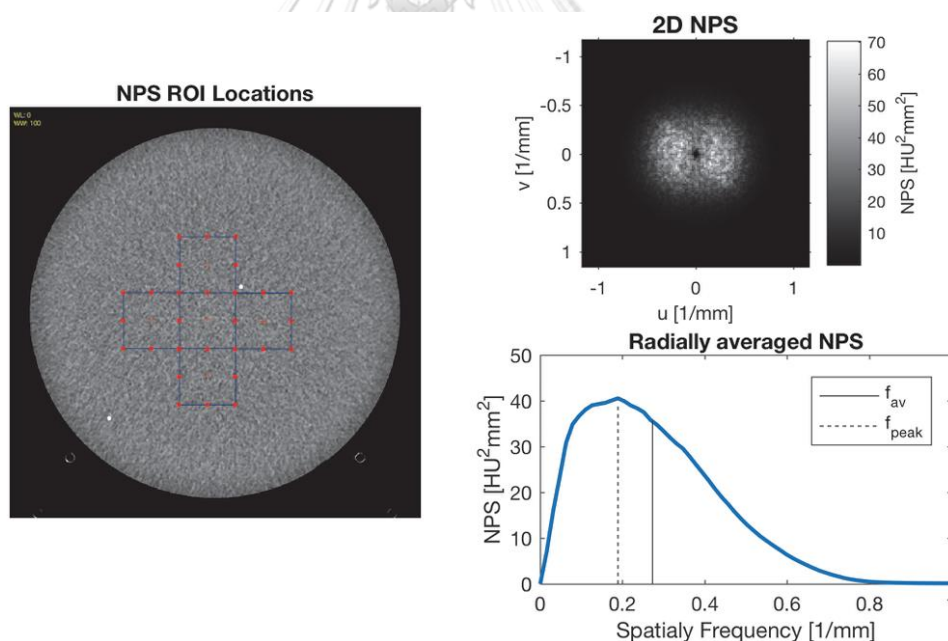


Figure 2.18 Noise texture analysis using the NPS.

The water phantom(s) or other uniform phantoms of relevant diameter to mimic the attenuation of a patient's body or head, should be scanned with sampling representative protocol and dose conditions of interest. For noise magnitude, the average pixel SD across a minimum of three images is used as the output. The three images could come

from repeated acquisitions or from slices (ideally non-consecutive) from the same acquisition. For noise texture, the peak frequency, $f_P$, and the average frequency, $f_A$ are reported as summary metrics, which describe the overall frequency content of the NPS as

$$f_p = arg\ max[NPS(f)] \tag{2.15}$$

and

$$f_A = \frac{\int f x NPS(f) df}{\int NPS(f) df} \tag{2.16}$$

Where $f$ is the radial spatial frequency (i.e., $f = \sqrt{f_x^2 + f_y^2}$ and NPS($f$) is the radially re binned/aver Figure 2.18.[29]

The formulation of the NPS assumes that the noise is wide-sense stationary within the ROI. This assumption may not be valid for very large ROIs due to the known global nonuniformity of CT noise. Ensure the areas sampled for noise determination represent predefined local areas void of artifacts and noise disparity.

### 2.1.3.C. Detectability index (d')

To characterize CT system performance in terms of a Fourier domain-task-based detectability index using the quasi-linear assumption of linear and wide-sense stationary system behavior within a local spatial, contrast, and noise domain. The underlying idea behind task-based image quality assessment is to quantify image quality by estimating how well a human or mathematical observer (i.e., reader) could perform some predefined task (e.g., detection of a subtle signal) on the images in question. Thus, a task-based image quality metric is more related to how well an image performs in delivering diagnostic information. As a result, task-based image quality metrics are well suited to characterize and/or compare image quality between imaging conditions in which noise magnitude, noise texture, and/or resolution might be variable.

CNR on the other hand is only useful as a very simple first-order approximation of low-contrast detectability under fixed noise texture and resolution conditions. In other words, it would not be appropriate to compare different reconstruction kernels or algorithms on the basis of CNR. Specifically, using CNR as the basis of estimating dose

reduction potential for iterative reconstruction algorithms (compared to FBP) or different kernels should not be done and could provide highly misleading and suboptimal results.

Detectability index (d') is a task-based detection performance metric (often referred to as d' or d-prime). Any task-based image quality assessment technique has three primary components: *(1)* a task to be performed (usually the detection of a subtle lesion/signal), *(2)* an observer to perform the task (typically a mathematical detection algorithm, sometimes a human reader), and *(3)* images to be assessed. Based on the foundational mathematics of signal detection theory, one can imagine an ensemble of images acquired under identical conditions, some with a target signal to be detected and some without. The observer processes the image data and outputs a scalar response variable for each image, proportional to the observer's confidence that a signal is present. This results in two distributions of the response variable (signal-present and signal-absent). The greater the separation between those distributions, the better the observer is at correctly detecting the signal. The detectability index, d', quantifies this degree of separation and is essentially the signal-to-noise ratio of the observer's response variable for the aforementioned signal-present and signal-absent distributions. Mathematically, the square of d' is the squared difference in the distribution means, divided by their average variances. One would expect a different d' for different tasks, different observers, and/or images acquired under different conditions. In this section, the task considered is the detection of a circular signal as defined by a task function ($W_{task}$, see below) and the mathematical observer used is a non-prewhitening matched filter (NPW, see below). It turns out that one can compute the detectability index, $d'_{NPW}$, for this observer in the Fourier domain based on measurements of system resolution (TTF), and noise (NPS) as shown below. To do this calculation, it is also necessary to define the properties (e.g., size, shape, contrast, and contrast-profile) of the signal be detected. These properties are encoded in the task function, $W_{task}$. The detectability index is interpreted as a metric of image quality due to its relation to low-contrast detectability (i.e., an increase in $d'_{NPW}$ implies the signal is easier to detect and thus image quality is better). Such Fourier-domain metrics have been shown to agree closely with human observer studies for linear shift-

invariant (LSI) systems and are being adapted for use in nonlinear systems that are evaluated in a quasilinear state (e.g., IR algorithms).

- Task Function ($W_{task}$): Fourier transform of the signal to be detected (e.g., a 10-mm circular lesion with a contrast of 10 HU). As mentioned above and described in detail below, measuring d' involves defining the properties (size, shape, contrast, and contrast-profile) of the signal to be detected. These properties can be encoded in this task function. Common task functions correspond to circular low-contrast signals having diameters between 1 to 10 mm. Suggested mathematical formulations are provided below.

- Non-prewhitening matched filter (NPW): this observer model compares the image of interest to a template consisting of the expected signal via cross-correlation. This model has been shown to correlate strongly with human performance for low-contrast detection tasks. The detectability index for this model, $d'_{NPW}$, can be computed in the Fourier domain for a given $W_{task}$ based on measurements of the system's TTF and NPS as shown below.

For each acquisition and phantom insert, estimate the TTF and then define a task function, $W_{task}$ by first synthesizing an ideal image of a signal to be detected. The $W_{task}$ is defined as the Fourier transform of this synthesized signal. As common approximations, the shape of the signal may be circular with either a rectangular or designer contrast-profile (Figure 2.19).[27] respectively, formulated as

$$c(r) = C \prod (rD/2), \text{ or } c(r) = C \left[ 1 - \left( \frac{2r}{D} \right)^2 \right]^n , \qquad (2.17)$$

where c is the value of the signal at a radial distance r, C denotes the peak contrast of the signal against the background in HU, $\prod$ is the rect function, D is the signal diameter, and n is a constant dictating the sharpness of the edge of the designer contrast-profile (as n decreases, edge sharpness increases, recommended value is 1, with alternative values ranging between 0.25 to 2). Note that in the designer profile equation, D denotes the diameter at which the contrast reaches zero. The apparent (i.e., visual) diameter of the signal might be lower than D depending on the chosen value of n. In some cases, it is

useful to parameterize the object's diameter by its full-width-at-half-maximum (FWHM), which can be computed as a function of D:

$$FWHM = D\sqrt{1 - 0.5^{1/2}} \tag{2.18}$$

Three diameters for the signals are recommended: large (10 mm), medium (5 mm), and small (1 mm). Note that the contrast, C, of the signal should roughly match the contrast of the insert used to measure the TTF. An ideal range is between 10 and 100 HU. Next calculate $W_{task}$ by taking the Fourier transform of the synthesized image. Finally calculate $d'_{NPW}$ as

$$d'^2_{NPW} = \frac{[\iint |W_{task}(u,v)|^2 x TTF^2(u,v) du dv]^2}{\iint |W_{task}(u,v)|^2 x \ TTF^2(u,v) x NPS(u,v) du dv}. \tag{2.19}$$

where u and v are the spatial frequencies corresponding to the x and y direction, respectively. This formulation of the detectability index, based on the non-prewhitening matched filter, assesses detection in two-dimensional images, thus using 2D integrals. Using the recommended protocols above, it is possible to assess image quality as a function of dose, tube potential, tube current modulation setting, phantom size, task size, task contrast, image thickness, reconstruction algorithm, and reconstruction kernel, thus offering a system characterization over a wide sampling of operational settings.

When creating $W_{task}$, be sure that the assumed contrast of the object to be detected and the insert used to measure the TTF are similar. Also be sure to report the contrast of the insert and noise conditions under which the TTF was measured.

Non-prewhitening matched filter is only one among many such observer models that can be used to integrate and extend the resolution and noise properties of an imaging system toward the performance for a defined task.[30] However, the use of this model (NPW) to standardize the process based on a model, has shown strong correlation with observer data.[31, 32]
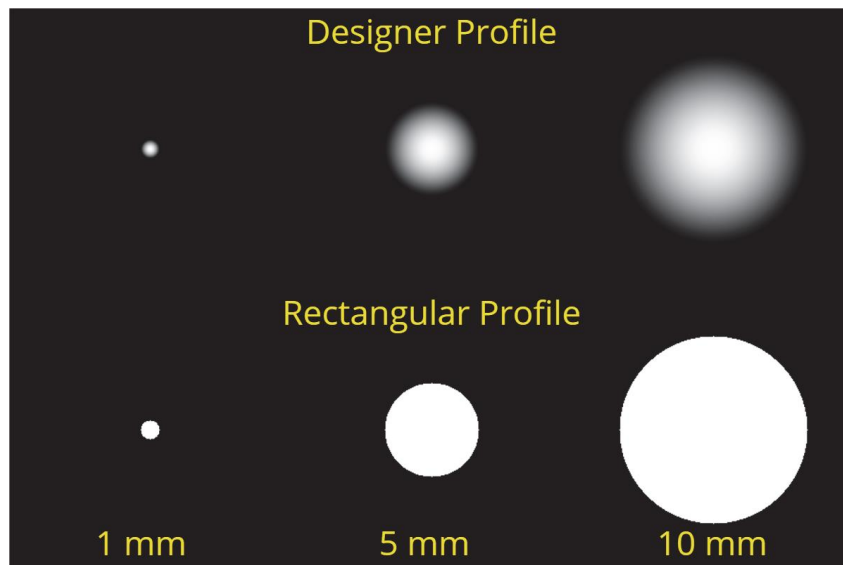
**Figure 2.19** Examples of the synthesized signals to be detected. The Fourier transform of such a signal is the task function, $W_{task}$, which is an important component of the detectability index calculation. Signals of three sizes are shown, with the top rows showing signals with a designer contrast profile and the bottom row with a rectangular contrast profile.[27]

### 2.1.4 Three-dimensional (3-D) Printing.

The three-dimensional (3D) printing technology was firstly invented in the early 1980s to fill the requirement for rapid engineering of design prototypes. The process, also known as "rapid prototyping (RP)" and "additive manufacturing (AM)," widely expanded in the fields of architecture and manufacturing in the 1990s. Today there is a multitude of diverse 3D printing technologies that can manufacture objects using a vast array of materials, from thermoplastics and polymers to metal, it is capable to fulfill most engineering and design needs.  This layer-by-layer production method provides greater flexibility and creativity in the design process.

The Standard Tessellation Language or, as also commonly referred to, the stereolithography file format, abbreviated as "STL.", is used to communicate with 3D printer. The STL format defines surfaces as a collection of triangles (called facets) that perfectly fit together without any gaps, like a jigsaw puzzle. 3D printers use data encoded in the STL file format to successively fuse or deposit thin layers of material.

3D-Printing technology has ability to produce three-dimensional (3D) objects and provides potential for developing reproducible and sophisticated physical phantoms. 3D printing technology can help rapidly develop relatively low-cost phantoms with appropriate complexities, which are useful in performance testing in imaging or dosimetry measurements.

### 2.1.4.A. Fused deposition modelling process

Fused deposition modelling (FDM) or Fused Filament Fabrication (FFF) is one of the most common techniques in additive manufacturing (AM) processes. This technique was developed by Scott Crump in 1989 and has been boosted throughout the subsequent years. In this technology, the filament is fed into one or more extruder. The gear mechanism in the extruder pulls the filament and pushes it down to the heater, where the filament gets melted. The melting temperature depends on the type of filament used and generally ranges from 190°C for PLA to 300°C for Polycarbonate. This melted filament then flows to the nozzle. The nozzle deposits the melt filament selectively on the print bed in the shape of the layer of the object being printed. The nozzle and/or the print bed move in the x–y plane in a path precomputed by the printer driver software to efficiently trace the shape of the printed object at each layer. After the first layer is printed, the print bed moves down (for some kinds of printer, the print bed is fixed, and the nozzle moves up) for a small distance (this distance is called layer thickness) to print the second layer. This time the first layer and the second layer are still hot and as a result, they fuse together for a strong bond. This process repeats and continues until the complete model is printed. Once extruded at each location occupied by the object, the material hardens by cooling. The material is typically a filament wound on a coil which is unreeled by motors feeding it to the extrusion head.
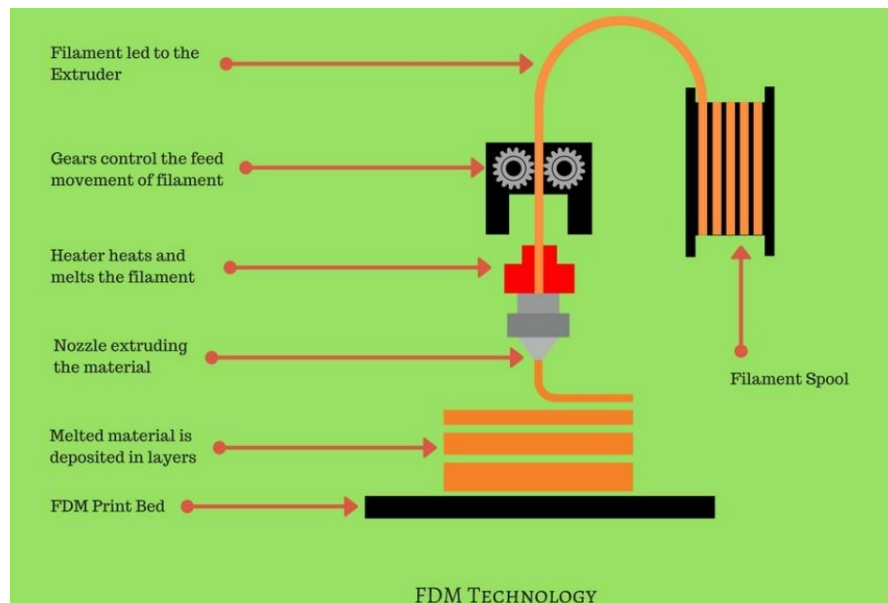
**Figure 2.20** Schematic of the FDM process. *(Available from: How FDM/FFF 3D Printing Technology Works? - Manufactur3D (manufactur3dmag.com))*

Various thermoplastics including Acrylonitrile butadiene styrene (ABS) and polylactic acid (PLA) plastics, and polymers including biocompatible polyether ether ketone (PEEK) and metals can be printed with FDM.

### *2.1.4.B. Fused deposition modelling process parameters.*[33]

In FDM, many parameters affect the surface quality and mechanical properties of the printed product. Therefore, the key to achieve high quality is to optimize the critical factors to minimize errors during the printing process. The main parameters which affect the final products are explained as follows:

- *Filling pattern* is an important factor that affects the mechanical properties and stiffness of fabricates. It comes in different shapes and geometries (Figure 3a). The percentage of infill controls the part shape, which can be either solid or hollow. The percentage of infill starts from 0% to 100%. The pattern shape is either cubic, linear, rectilinear, honeycomb or wiggle.

- *Nozzle temperature* is a vital factor, which changes from 170°C to 220°C based on the material melting point. The poor temperature in the nozzle affects layer adhesion and the printing process.

- *Bed temperature* is one element that use to control the melted material. The temperature range is from 0°C to 80°C, depending on material properties.

- *Nozzle diameter* affects the surface quality and mechanical properties of products. The size of the nozzles is from 0.2 mm to 0.8 mm., smaller nozzle diameter prints more precise products, but requires a longer time.

- *Build orientation* affect to mechanical properties and surface textures of printed product. Products can be printed at different angles (0° to 180°) and in x, y and z directions.

- *Air gap* is space between the adjacent raster and the beads of FDM on the same layer. Both air gap and orientation affect the tensile strength of the products. The negative air gap (-0.003) increased the strength and stiffness of 3D-printed products.

- *Layer thickness* or layer height is the thickness of the gap between the nozzle and bed, which explains the width of each layer. Thereby, setting the nozzle in the correct distance should be done as it directly correlates with the nozzle diameter. The value of layer thickness is from 0.06 mm to 0.6 mm. By decreasing the layer thickness, the quality of the product is increased while the printing time is maximized.

- *Raster width and raster angles* are the width of the material bead and raster pattern angle in the x-direction. Warping and shrinkage are due to these factors.

- *Printing Speed* is the speed of printing in the unit of mm/s. The printing speed can be varied depending on the material and can affect the quality of printed products. The high printing speed decreases the cooling time of the layers during printing. Therefore, printing speed should be chosen wisely to prevent defects.

## 2.2 Literature review

With technological advancement of dual-energy CT in abdominal imaging, the clinical studies demonstrated potential benefits of dual-energy virtual monochromatic images (VMIs) in improvement of the liver lesion conspicuity and reduced the beam hardening artifact has been conducted. Hanson et al.[9] performed qualitatively assessment between single-energy low tube potential (SE-LTP) and dual-energy virtual monochromatic (DE-VM) images in clinical CT images, by comparing the liver lesions conspicuity, artifacts, and radiologist preferences in dose-matched. Thirty-one patients with 72 proven liver lesions (21 benign, 51 malignant) underwent full-dose contrast enhanced DECT. Half-dose images were obtained using single tube reconstruction of the dual-source SE-LTP projection data (80 or 100 kV), and by inserting noise into dual-energy projection data, with DE-VM images reconstructed from 40 to 70 keV. The images were evaluated using multi-reader evaluation by qualitative scoring of lesion conspicuity, image noise, sharpness, and artifact. For the quantitative analysis, the liver to lesion CNR was calculated. The results showed that at the same applied dose level, liver lesions were more conspicuous using DE-VM compared to SE-LTP; however, SE-LTP images were preferred more than any single DE-VM energy level, likely due to lower noise and artifacts. In this study the lesions were identified prior to the reader study, therefore they solely compared lesion conspicuity but did not measure lesion detection and characterization to measure observer performance.

For the quantitatively assessment of lesion detectability, traditional image quality metrics, such as contrast-to-noise ratio, have become inadequate indicators of clinical imaging. In 2019, the report of American Association of Physicists in Medicine (AAPM) task group 233[25] recommend using advanced image quality matric(i.e., NPS, TTF) and task-based image quality (i.e., detectability index, d') that more directly reflect clinical performance. In addition, the concept have been investigated by *Cheng et.al.*[34] They conducted the study to extend and validate the assessment of detectability index for detection of hepatic metastasis in clinical abdomen CT images. Their study indicated that algorithmic assessment of lesion detection and perceptual quality can predict observer

assessment for detecting hepatic metastasis with strongly correlation. From their study, it can be concluded that the detectability index provides a robust reflection of overall image quality for detecting hepatic lesions under clinical CT imaging conditions. This demonstrates the concept of utilizing the measure to quantitatively assess the quality of the information content that different imaging conditions can provide for the same clinical imaging task, which enables targeted optimization of clinical CT systems to minimize clinical and patient risks.

There are studies used tasked-based image quality to evaluate the spectral performance of dual-energy CT (DECT) among the different dual energy technology. In 2021, Greffier, J., et al.[39] firstly reported the comparison of the spectral performance on four DECT platforms; fast kV-switching CT (KVSCT), split filter CT(SFCT),dual-source CT (DSCT), and dual-layer CT (DLCT), using task-based image quality assessment for abdominal imaging based on phantom data. The phantoms (ACR QA phantom (Gammex 464) and Multi-energy CT phantom model 1472 (Sun Nuclear)) were scanned using the classical parameters of abdomen-pelvic CT with the $CTDI_{vol}$ of 10 mGy. The virtual monochromatic images (VMIs) were created at 40 to 70 keV for the assessment of NPS and TTF. The d' were then computed to model the detection task of two contrast enhancement lesions (soft tissue and blood-mimicking iodine at 2 mg/cc and 4 mg/cc) as a function of keV. They reported that the noise magnitude decreases as increasing the keV from 40 to 70, and the highest noise magnitude values were found for KVSCT and SFCT and the lowest for DSCT and DLCT. The TTF values decreased with the increase of keV deteriorating the spatial resolution. Their results showed that among the different energy levels (40-70 keV) the higher detectability (d' value) was obtained at 40 keV for DLCT, DSCT, and SFCT but at 70 keV for KVSCT for both contrast enhancement lesions. The detectability tends to be higher in DLCT and DSCT platform compared to other platform and the highest d' was found for DLCT for the lowest energy levels (40 keV). The novelty of their study is that the task-based image quality assessment is firstly reported for DECT acquisitions to show the benefit of using low keV for the detection of contrast-enhanced lesions. However, the authors mentioned for several limitations in their study.

The image acquisitions were performed for only one dose level and a single standard soft tissue kernel for each platform is used. The impact of the choice of kVp pair for DECT platforms on spectral performance depending on the size of the patient have not been studied. Moreover, instead of using iterative reconstruction (IR), this study used the filtered-back projection method to reconstruct the images which may not reflect to the actual performance of current clinical protocols.

The authors, Greffier, J., et al.[35], also conducted the study on the impact of four kVp combinations 100/Sn150 kVp, 90/Sn150 kVp, 80/Sn150 kVp, and 70/Sn150 kVp available in a dual-source dual energy CT on spectral performance of abdominal imaging. Their study firstly assesses the noise magnitude (HU), noise texture ($f_{av}$), spatial resolution (TTF50%), and detectability (d') of two focal liver lesions (liver metastasis and HCC), in addition to the accuracy of iodine quantification. They concluded that for abdominal imaging and the lowest energy levels, the use of 70/Sn150 kVp presented the lowest image noise and the highest detectability of two small focal liver lesions in VMIs. However, using the 100/Sn150 kVp pair provides the better result on optimum image noise and detectability on mixed images and highest accuracy of iodine concentration. Again, the effect of dose level, difference in patient size, the use of iterative reconstruction or other kernel and variation of pitch have not been carried out. The study including these factors should be conducted to add the clinically relevant.

In addition to the improvement of lesion contrast from low keV-VMI, the dual energy CT-based iodine quantification (DECT-IQ) has been shown to improve lesion detection and characterization and to enable monitoring of tumor treatment response in oncologic imaging of the abdomen and pelvis CT. Several clinical studies demonstrated its capability to distinguish malignant from benign lesions as well as metastatic from non-metastatic lymph nodes. Recently, the potential for DECT-IQ as a predictive pre- and post-treatment imaging biomarker has been investigated. Therefore, there are many studies reported the accuracy of DECT-IQ and determine the minimum detectable different in iodine concentration in different dual energy CT. Euler et.al (41) investigated the impact of scan- and patient-related factors on the error and the minimum detectable difference

in iodine concentration among different generations of single-source (SS) fast kV-switching and dual-source (DS) dual-energy CT (DECT). In their study, a custom abdominal phantom was fabricated using a 3D-printer with additional peripheral ring to simulate medium and large size patient. There are 8 fillable cylinder rods, contain different iodine concentration solutions of 0.2, 0.4, 0.6, 0.8, 1.0, 1.2, 2.4, and 4 mgI/cc. The phantom was scan under different scanner condition and their results showed that the DECT-IQ error was significantly higher with increasing phantom size and decreasing radiation dose. In addition, the minimum detectable difference in iodine concentration depends on patient- and scan-related factors and ranged from 0.4 to 1.5 mgI/cc. These studies imply that the radiologists should be aware of the relatively high error ranges of DECT-IQ, especially in large-sized patients.

As mentioned earlier, to assess image quality and evaluate the performance of CT imaging, physical phantoms having the specific properties and lesions are highly desirable. The traditional techniques to construct the customized phantoms is high in costs and is limited to accommodate personalized patient's pathological features. Additive manufacturing, or three-dimensional (3-D) printing, has been widely used in industry and recently it has been applied in medicine. This layer-by-layer production method provides greater flexibility and creativity in the design process. Ma et.al.,(42) studied on the systematically testing and analysis of mechanical and medical imaging properties for three 3D printed materials of polylactic acid (PLA), polyamide 12 (PA12) and light curing resin (LCR). The mechanical and medical imaging properties of the three materials, such as elastic modulus, density, effective atomic number, X-ray attenuation coefficient, computed tomography (CT) number, and acoustic properties, were investigated. If we focused on the properties related to x-ray CT, their results showed that x-ray attenuation coefficient of materials decreased with increasing tube voltage (from 40–120kVp range) in the order of $\mu$(LCR) > $\mu$(PLA) > $\mu$(PA12). The difference of material color would not cause a significant change in $\mu$ value. For CT number, PLA and LCR were comparable with skeleton tissue when PA12 was close to adipose. The order of the density and the effective atomic number product ($\rho^* Z_{eff}$) agreed with the results obtained from

μ measurements. The $\rho Z_{eff}$ of LCR was similar to that of some bones; PLA and PA12 were close to some soft tissues. This can be summarized as 3D printed materials could be used as tissue equivalent materials to simulate some soft and bone tissues, when using 3D printing technology to construct a phantom. In addition, their results provided clear guidance in selecting materials suitable as fat, bone, and soft properties.

# CHAPTER 3

# RESEARCH METHODOLOGY

## 3.1 Research hypothesis

- The hepatic lesion detectability in abdomen dual energy CT is better than by 120 kVp single energy CT.

- The hepatic lesion detectability is affected by dual energy CT scan parameters, and patient characteristics.

## 3.2 Research questions

- What is hepatic lesion detectability on dual energy CT imaging?

- Which factors influence the hepatic lesion detectability on dual-energy CT imaging?

## 3.3 Research objectives

- To determine the hepatic lesion detectability in abdomen from various phantom sizes by dual-energy CT imaging.

- To investigate factors affecting the detectability of hepatic lesion in abdomen by dual-energy CT imaging.

## 3.4 Scope of work

This phantom study is performed to determine the hepatic lesion detectability in dual energy CT using dual source dual energy CT platform. The detectability was assessed by using mathematical model observer to quantify the detectability index for enhancing hepatic lesions on abdomen dual energy CT images.

## 3.5 Research design

Observational descriptive study.

## 3.6 Conceptual framework
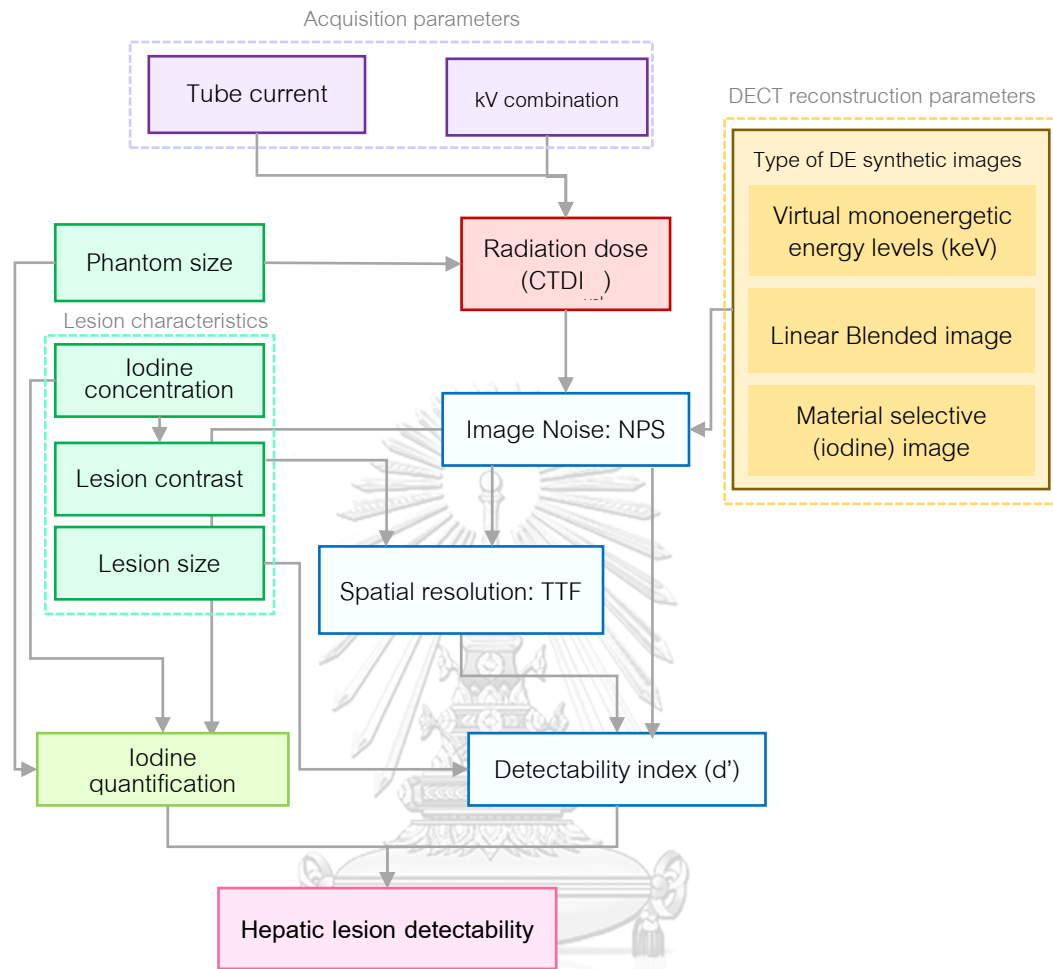
## 3.7 Research design model
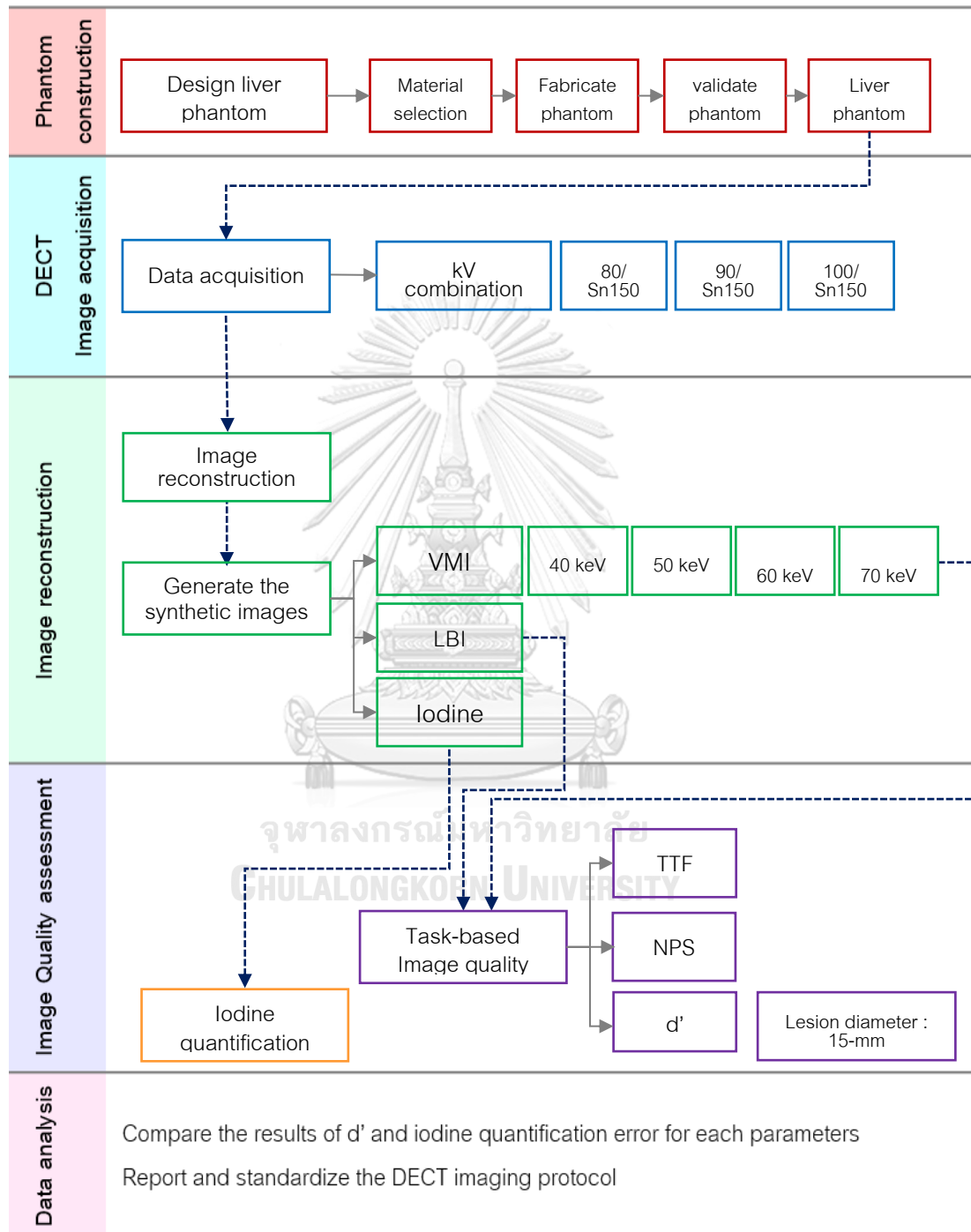
## 3.8 Expected benefit

- The abdomen dual energy CT protocols enhanced the low contrast hepatic lesion detectability.

## 3.9 Variable measurement

Independent variables are kV combination, virtual monoenergetic energy level (keV), iodine concentration, phantom size.

Dependent variable is detectability index and iodine quantification error for hepatic lesions.

## 3.10 Data collection

The QRM liver phantom was scanned using abdomen dual energy CT protocol with various acquisition and reconstruction parameters. The image data were sent to the computer workstation to generate the virtual monoenergetic images at different energy levels. The outcome images at different imaging condition were exported as DICOM file to be imported into image quality analysis software (ImQuest) to measure the TTF, NPS and then computed the detectability index of each imaging condition. The results were exported into comma separated values (.cvs) format and further used for data analysis. In addition, the data acquired from 3D printing liver nodule phantom were scanned with the same DECT acquisition parameters. The acquired DECT data set were also sent to the computer workstation using dual energy application to measure the iodine density compared to the true values. The data were recorded in Excel.

## 3.11 Data analysis

The obtained detectability index (d') from various imaging parameters were reported in tabulate format. In addition, the image quality data: contrast, TTF, and NPS were plotted against virtual monoenergetic energy levels to demonstrate the trend and the characteristic of d' as a function of acquisition and reconstruction parameters.

For the assessment of iodine quantification error, the measured values were compared to the true values and % deviation were also calculated.

The minimum and maximum were determined for both results to indicate the best and poor imaging conditions between various phantom size and lesion characteristics.

## 3.12 Outcome

The detectability index (d') and iodine quantification error for different phantom sizes, parameter settings in DECT were estimated. The impacts on acquisition and reconstruction DECT parameters to the d' and iodine quantification were investigated and reported.

## 3.13 Statistical analysis

The descriptive statistic of average, standard deviation minimum and maximum were analyzed using the Microsoft Excel program.

## 3.14 Ethical Consideration

This research was conducted in phantom; however, the research proposal had been submitted to the institutional review board (IRB) of Faculty of Medicine, Chulalongkorn University. According to the criteria, the research proposal has been categorized as "exemption for IRB" review and approved with the COE No. 012/2019 and IRB No. 260/62.
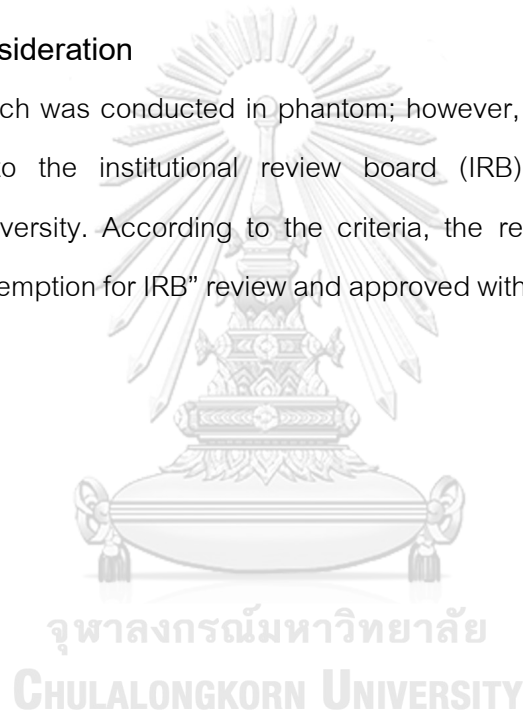
COE No. 012/2019

IRB No. 260/62

## INSTITUTIONAL REVIEW BOARD

### Faculty of Medicine, Chulalongkorn University

1873 Rama IV Road, Patumwan, Bangkok 10330, Thailand, Tel 662-256-4493

### Certificate of Exemption

The Institutional Review Board of the Faculty of Medicine, Chulalongkorn University, Bangkok, Thailand, has exempted the following study in compliance with the International guidelines for human research protection as Declaration of Helsinki, The Belmont Report, CIOMS Guideline, International Conference on Harmonization in Good Clinical Practice (ICH-GCP) and 45CFR 46.101(b)

Study Title : Hepatic Lesion Detectability on Dual Energy Computed Tomography Imaging: Phantom Study

Principal Investigator : Miss Hataipat Jantawong

Study Center : Department of Radiology, Faculty of Medicine, Chulalongkorn University.

Signature: ................................................ Signature: ................................................

(Emeritus Professor Tada Sueblinvong MD)

Chairperson

The Institutional Review Board

(Assistant Professor Prapapan Rajatapiti MD, PhD)

Member and Secretary

The Institutional Review Board

Date of Exemption : April 23, 2019

Note No continuing review report and final report when finish require

# CHAPTER 4

# MATERIALS AND METHODS

## 4.1 Materials

To simulate the patient attenuation for abdomen dual energy CT, two anthropomorphic liver phantoms had been used in this study. Those were QRM-Liver-Phantom for the lesion detectability study and the 3D printing phantom for the iodine quantification study.

### 4.1.1 Anthropomorphic abdomen phantom

Phantom model QRM Moehrendorf, Germany was used. The size of elliptical phantom is 300 mm x 200 mm x 100 mm in major-diameter x minor-diameter x thickness respectively with the weight of 4200 g. The phantom is designed in a modular construction principle and made up with three changeable parts: the anthropomorphic abdomen phantom body, the liver-insert, and the spleen-insert (Figure 4.1). The tissue equivalent plastic material was used for abdomen body with the CT No. of 35±5 HU at 120 kV, respect to the density and x-ray attenuation characteristics. In this study, only the body phantom and spleen insert part were used.
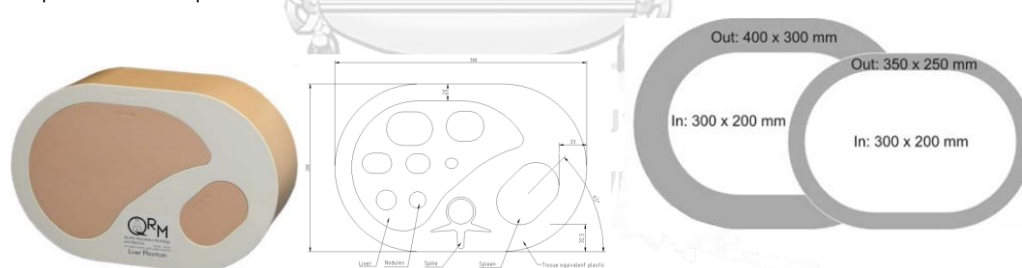


Figure 4.1 QRM-Liver-Phantom with exchangeable liver insert with liver nodules(left). The abdomen body part comprises of spleen insert and spine. The schematic drawing of the liver phantom is shown on the middle and the Two sizes of extension rings (M and L) to simulate the attenuation in larger patient shown on the right. Source: https://www.qrm.de/en/

For the liver insert, there are two types of nodules; Type 1 hypoattenuating (hypodense) nodule and Type 2 hyperattenuating (hyperdense) nodule which has a CT of 45 HU and 180 HU at 220 kVp respectively (Fig 4.2). In this study, the arterial phase

enhancement liver lesion is target lesion therefore the simulated hyperattenuating nodule (type2) was investigated.

To determine the influence of higher attenuation in larger patient size on image quality, the elliptical shape extension rings were used combining with the abdomen body phantom. The extension rings used in this study are produced with tissue-equivalent material (at 120 kVp) for medium size (M) with major and minor diameter of 350 mm x 250 mm and fat-equivalent material with major and minor diameter of 400 mm x 300 mm for large size (L) Figure 4.1.
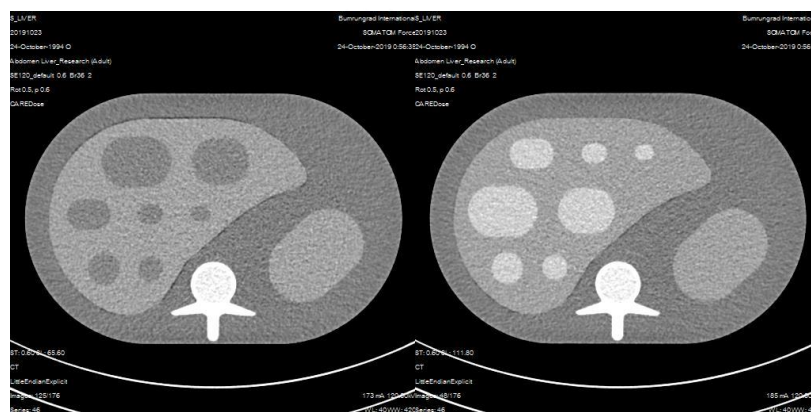


**Figure 4.2** CT image acquired at 120 kVp demonstrated Type1-hypodense liver nodules (45 HU) (left) and Type 2-hyperdense liver nodules (180 HU) (right).

### 4.1.2 3D-Printer

This study aims to investigate iodine quantification for hepatic lesion with different iodine concentrations, but the standard QRM liver nodule phantom contains only 2 concentrations therefore the customized liver phantom was made using 3D-printing technology. The ROKIT model INVIVO is 3D-bioprinting technology using fused deposition modelling (FDM) technique. The nozzle diameter is 0.2 mm with maximum printing speed of 20 mm/s and minimum layer thickness of 0.8 mm. The capable building size is 100x100x80 mm. The printer is compatible with a wide range of materials including standard materials such as thermoplastics (i.e., PLA, ABS) and Bio-ink/organic (i.e., biopolymer filaments, hydrogels). This printer was supported by M3D Laboratory Faculty of Engineering, Chulalongkorn University, Bangkok.

### 4.1.3 Printing Filament

The polylactic acid (PLA) material manufactured eSUN, is used as printing filament with the filament properties according to Table 4.1. The eSuN PLA plus has a high purity and nontoxic materials. The filament diameter is 1.75 mm (dimension accuracy at +/- 0.05mm). The extruder temperature of 210-230°C and bed temperature of 45-60°C are recommended. The filament properties and recommended printing parameters of eSuN PLA plus is shown in Table 4.1.

**Table 4.1** The filament properties and Recommended printing parameters of eSuN PLA plus.

| Filament properties | |
|---|---|
| 3D printing filament | PLA+ |
| Density (g/cm$^3$) | 1.23 |
| Heat Distortion Temp. (°C/MPa) | 53 |
| Melt Flow index (g/ mins) | 5 (190°C/2.16kg) |
| Tensile Strength (MPa) | 4 |
| Elongation at break (%) | 20 |
| Flexural Strength (MPa) | 74 |
| Flexural Modulus (MPa) | 1973 |
| Durability | 4/10 |
| Printability | 9/10 |
| Recommended printing parameters | |
| Extruder temperature (°C) | 210-230°C Recommended temperature: 210°C |
| Bed Temperature (°C) | 45-60°C |
| Fan speed | 100% |
| Printing speed | 40-100 mm/s |
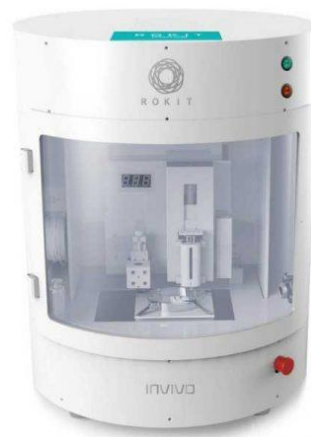
**Figure 4.3** The ROKIT INVIVO is a hybrid 3D bioprinter made by ROKIT, a manufacturer from South Korea. The INVIVO is suitable for biomedical applications.

*Source: https://www.aniwaa.com/product/3d-printers/rokit-3dison-invivo/*

### 4.1.4 Simulated liver nodules

The iodinated contrast media solution for injection, 300 mgI/cc of Iohexol (Omipaque®, GE Healthcare, Cork, Ireland) was diluted with sterile water to make a different iodine concentration solution for simulated liver nodules at 1.0, 2.0, 2.5, 3.0, 3.5 and 5.0 mgI/cc. The pipette ( BRAND® Transferpette® S) with a tip volume of 0.1 cc (1000 μL) was used as a high-quality liquid handling equipment to ensure the accuracy of pipetting.

### 4.1.5 Dual-energy CT System

The dual energy CT scanner used in this study is SIEMENS Somatom ® Force (Siemens Healthineers, Forchheim, Germany) installed at Bumrungrad International Hospital, Bangkok, Thailand in the year 2016 (Figure 4.4). This is the third-generation dual source dual energy CT system using two x-ray tubes and two corresponding detectors (A and B) offset within the gantry orthogonally at an angle of about 95°. Due to the specific design of the tube-detector configuration, when the dual energy acquisition is performed, the field of view (FOV) on detector A is fully at 500 mm but limited to 356 mm FOV on detector B. For the DECT acquisition, the kV combination is selected where tube "A" delivers a low-kVp beam and tube "B" delivers a high-kVp beam and the kV combination is noted by low-kVp/high-kVp. This generation had been introduced with a new high-kV

tube (tube B) operates at 150 kVp equipped with 0.6 mm tin filter, these new features enable an improvement of the material discrimination via increased spectral separation. The choices of kV combinations in this generation are generally at 80/Sn150, 90/Sn150, and 100/Sn150. In addition, the new powerful x-ray tube provides the higher x-ray tube current to overcome the limitation of maximum tube current at low kVp or ultra-high pitch settings. The technical specification of SIEMENS Somatom® Force was shown in Table 4.2.

The DECT synthetic images are generated using the image-based method by Syngo.via software (version VB30A_HF06) which is built on the client-server platformed. The images data from low and high kV are generally sent to the Dual energy application to create the different synthetic images or to perform the quantitative assessment (i.e., VMI, iodine quantification, liver fat, etc.) The Syngo.Via provides configurable, automatic mapping of the case-relevant Dual Energy applications based on the body region and the use of contrast medium, e.g., syngo.CT Virtual Unenhanced is selectable in the user interface (UI) if the case of contrast enhanced abdomen images is acquired.

Table 4.2 Technical Specifications of SIEMENS Somatom® Force.

| | |
|---|---|
| X-ray tubes | 2 x Vectron™ X-ray tubes |
| Detectors | 2 x Stellar[Infinity] detectors with anti-scatter 3D collimator grid |
| Number of acquired slices | 384 (2 × 192) slices |
| Rotation time | up to 0.25 s |
| Temporal resolution | up to 66 ms |
| Generator power | 240 kW (2 x 120 kW) |
| kV settings: SE mode | 70 – 150 kV, in steps of 10 kV |
| kV settings: DE mode | 80/Sn150, 90/Sn150, 100/Sn150 |
| Spatial resolution | 0.24 mm |
| Max. scan speed | 737 mm/s with Turbo Flash |
| Table load | up to 307 kg/676 lbs. |
| Gantry opening | 78 cm |

**Figure 4.4** SIEMENS Somatom ® Force (Siemens Healthineers, Forchheim, Germany) installed at Bumrungrad International Hospital, Bangkok, Thailand.



**Figure 4.5** The Syngo.Via software version VB30A_HF06.

### 4.1.6 Image quality assessment software

In this study, the tasked base image quality was assessed by using the imQuest software, version 7.1, it is an open-source software package developed by Duke Clinical Imaging Physics Group available at https://deckard.duhs.duke.edu/~samei/tg233.html (Figure 4.6). The software was used to assess spatial resolution using the task transfer function (TTF), noise magnitude and texture using the noise power spectrum (NPS), and to estimate the ability of radiologist to detect specific lesions by using detectability index (d').
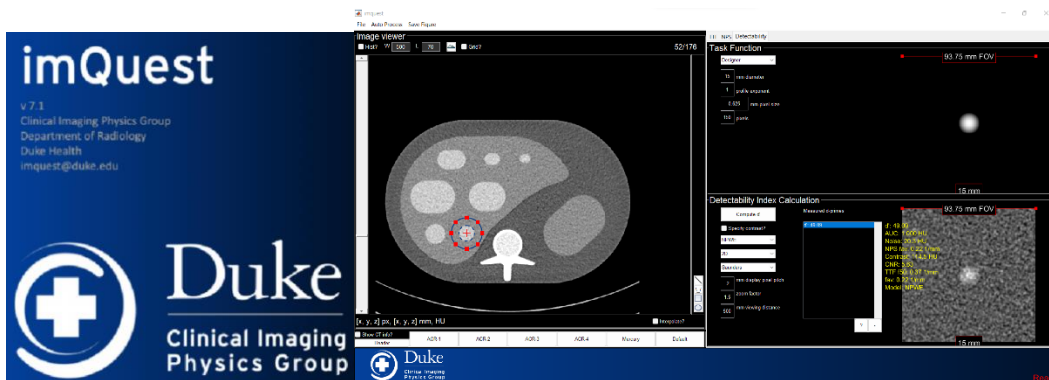
**Figure 4.6** The user interface of imQuest software developed by Duke Clinical Imaging Physics Group.

## 4.2 Methods

### 4.2.1 Liver nodule phantom design and construction

The phantom was designed and fabricated to have key characteristics as following:

- X-ray attenuation as the contrast enhancement liver tissue

- Homogeneous density in uniform parts

- Solid with no air gap inside the solid part

- Waterproof and no water leakage

- Accurate in size and geometry to fit with QRM body phantom and more accurate in results.

This process was conducted with helps and supports by the colleagues from M3D Laboratory, Faculty of Engineering, Chulalongkorn University, Bangkok, Thailand. The customized liver nodule insert was fabricated as following steps.

#### *4.2.1.A Phantom Design*

The QRM liver phantom was scanned by using CT scanner and the images were exported into DICOM files for images segmentation process to extract the actual shape and size of liver phantom. The liver phantom was then designed by using SOLIDWORKS software. Due to the limit of capable building size of the 3D printer that can print the maximum size of 100x100x80 mm, the phantom was designed to be separated into 3 smaller parts (Figure 4.7) where each part containing the holes for insertion of cylindrical

container of simulated liver nodules. The rods were designed to be in the cylindrical shape with 30 mm in diameter and 50 mm in height, there is a central rod with 15 mm diameter for filling the iodine solution.



Figure 4.7 The liver phantom was constructed as 3 separated small parts (a) each part consists of the empty holes for inserted removable cylindrical container with simulated liver nodule of 15 mm diameter inserted (c).

### *4.2.1.B Materials selection*

The available printing materials compatible to FDM 3D-printer were included and preliminary test by scanning with CT scanner. The CT No. of materials were measured and compared to the actual liver attenuation measure in clinical CT images. Finally, the PLA was selected as a printing material.

*4.2.1.C Printing parameter optimization*

The customized phantom was designed to produce the liver nodule insert rod that can contain the iodine liquid solution, therefore the key characteristics of printing phantom is watertight. The printing parameters were optimized for PLA with predefined printing parameter of the 100% infill, 0.4 mm line width, extruder temperature of 230°C and bed temperature of 60°C. The printing speed was varied from 30,40,60, and 70 mm/s and layer height of 0.1, 0.15, 0.2 mm. The test objects were printed into a square shape with the size of 15x15 mm and thickness of 5 mm, using the parameter described earlier and then was scanned by the DECT acquisition to investigate the impact of the printing parameter to the CT No. Finally, the printing parameters of 30 mm/s printing speed and 0.1 mm layer height were used in this study.

The 3D-printed phantom with simulated liver nodule inserted rods were placed appropriately into the QRM abdomen phantom and was used to scan for the study in part of dual energy iodine quantification (Figure 4.8).
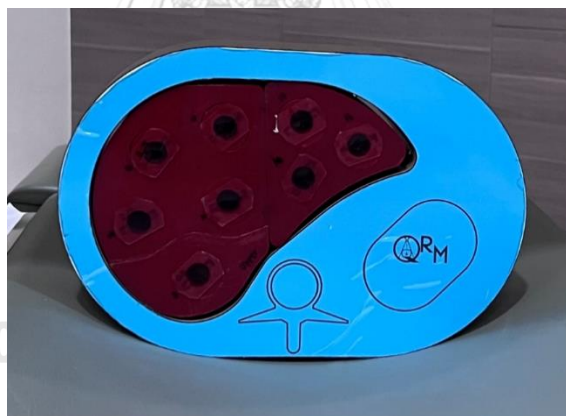


**Figure 4.8** The customized 3D-printed liver nodule phantom with the liver nodule inserted rods. The different iodine concentration was filled inside the rods.

### 4.2.2 Dual energy Image acquisition

The QRM and customized 3D printing liver phantoms were scanned under the abdomen DECT acquisition protocol with the following parameters: collimation of 128x0.6 mm, gantry rotation 0.5 sec, pitch of 0.6. To investigate the influence of the DECT acquisition parameters, the parameters were varied as following: 3 kV-combinations (80/Sn150, 90/Sn150, 100/Sn150). This study performed based on the clinical abdomen

protocol, the automatic tube current modulation (ATCM) was activated in all scans and the quality reference mAs was adjusted for tube A and automatically computed by the system for tube B, therefore they were adjusted as 400/200, 300/188 and 250/125 for 80/Sn150, 90/Sn150 and 100/Sn150 respectively.

Table 4.3 The summary of dual energy CT parameters used for each phantom scan.

| Acquisition mode | Dual energy (DE) | | |
|---|---|---|---|
| kVp setting | 80/Sn150 | 90/Sn150 | 100/Sn150 |
| Quality reference mAs*(A/B) | 400/200 | 300/188 | 250/125 |
| Rotation time | 0.5 s | | |
| Pitch | 0.6 | | |
| Slice acquisition | 128x0.6 mm | | |
| Reconstruction method | ADMIRE (2) | | |
| Reconstruction Kernel | Br36, Qr36 | | |
| DFOV (mm) | S: 320 | | |
| | M: 360 | | |
| | L: 420 | | |

*For DECT acquisition, Quality reference mAs is adjusted only for tube "A" and tube "B" will be automatically computed by the system.

Each phantom was placed at the center of CT gantry and was scanned three times with the same acquisition and reconstruction parameters for each protocol. Raw data were reconstructed by using level 2 (Strength 2) of advanced modeled iterative reconstruction (ADMIRE) using the standard soft tissue reconstruction kernel (Br36) in clinical practice for abdomen CT. The extension rings were added to the QRM abdomen liver phantom to simulate the higher patient attenuation for medium and large sizes and the scanned were repeated. The images were reconstructed with the slice thickness of 0.6 m (increment of 0.6 mm) for image quality assessment and 1.0 mm (increment of 1.0 mm) for iodine quantification analysis. The reconstructed displayed field of view (DFOV) was defined to fit to the phantom size, the values of 320, 360, and 420 mm were

reconstructed for small, medium, and large phantoms respectively. The summary of acquisition and reconstruction parameters were shown in Table 4.3.

### 4.2.3 Image reconstruction

The reconstructed images for low-and high-kV of QRM liver phantom from DECT data were transferred to vendor specific software (Syngo.viao software (Version VB30A), SIEMENS, Healthineer). The virtual monoenergetic images (VMI) were generated at 40, 50, 60, and 70 KeV using the "Monoenergentic+" function which is based on the image-based algorithm in Syngo Dual Energy application (Fig 4.9).



|  |  |  |
|---|---|---|
| (a) 80 kV image | (b) Sn150 kV image | (c) LBI |



|  |  |  |  |
|---|---|---|---|
| (d) 40 keV-VMI | (e) 50 keV-VMI | (f) 60 keV-VMI | (g) 70 keV-VMI |
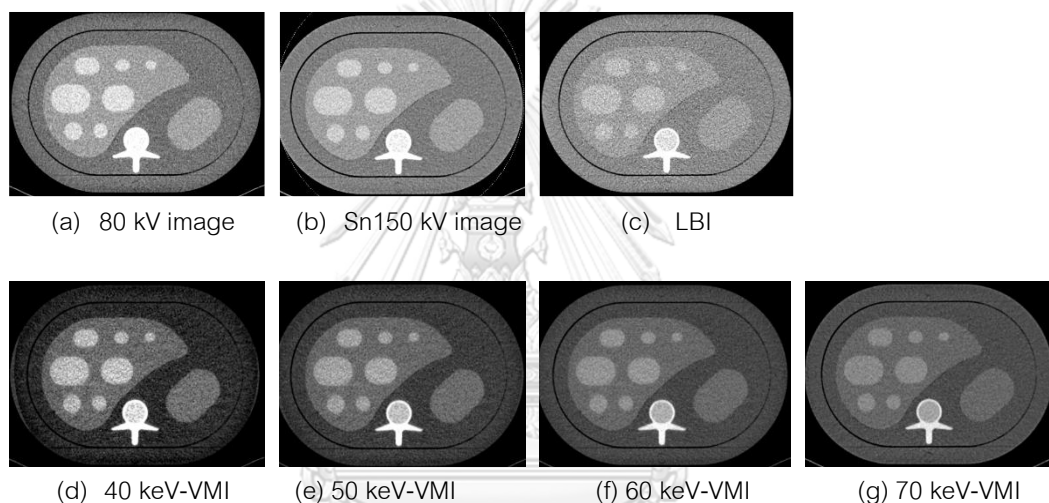
**Figure 4.9** The axial images of (a) 80 kV,(b) Sn150 kV, were used to generate the synthetic CT images of (c) linear blended images (LBI) and virtual monoenergetic images at (d) 40 kwV, (e) 50 keV, (f) 60 keV and (g) 70 keV.

The customized phantom with simulated liver nodule with different iodine concentrations were also sent to Syngo.Via to generate the material selective(iodine) images (Figure 4.10) using Liver VNC application profile and was further used for iodine quantification analysis.

**Figure 4.10** The material selective(iodine) image were reconstructed using Liver VNC application profile on Syngo.Via software.

### 4.2.4 Task-based image quality assessment

In this study, the task based image quality was assessed by using the imQuest software, version 7.1, designed by Duke Clinical Imaging Physics Group (Duke University).[25] The software assessed spatial resolution using the task transfer function (TTF), noise magnitude and texture using the noise power spectrum (NPS), and estimated the ability of radiologist to detect specific lesions by using detectability index (d'). The specific clinical task in this study is to detect the small hepatocellular carcinoma (HCC) which is the hyperattenuating lesions in liver.

The TTF was assessed by placing the circular ROI on 20 mm hyperdense liver nodule in phantom image (Figure 4.11). According to the methodology,[25] 5 consecutive slices of axial image were used to compute the edge spread function (ESF) and then Line spread function (LSF). Finally, by taking the Fourier Transform (FT) of LSF the TTF curve can be plotted. Like the modulation transfer function (MTF), the TTF curves can be summarized by the spatial frequencies at which the TTF reaches 50%, denoted as $f_{50}$.

The NPS was computed by placing four-square ROIs on the uniform area of liver region in phantom images (Figure 4.12). The NPS curve were generated with the following equation: [36]

$$NPS_{2D}(f_x, f_y) = \frac{\Delta_x \Delta_y}{L_x L_y} \frac{1}{N_{ROI}} \sum_{i=1}^{N_{ROI}} |FT_{2D}\{ROI_i(x,y) - \overline{ROI_i}\}|^2$$

where $\Delta_x$ and $\Delta_y$ are the pixel sizes in the x- and y- dimension, $L_x$ and $L_y$ are the ROI's lengths in pixel for both x- and y-dimensions, $N_{ROI}$ is the number of ROIs used, $\overline{ROI_i}$ is

the mean pixel value averaged from $ROI_i(x, y)$. The NPS curves obtained from the measurement were used to quantify the noise magnitude by taking a square root of the area under the NPS curve, the noise texture by reporting the peak frequency, $f_P$, and the average NPS spatial frequency, $f_{av}$.

Combining the resolution (TTF) and noise (NPS) properties of the image with the predefined clinical imaging task (W) together, the detectability index (d') was then computed (Figure 4.13). The detectability index based on non-prewhitening observer model with eye filter (d'$_{NPWE}$) was computed for a predefined clinical task as follows:

$$d'^2_{NPWE} = \frac{[\iint |W_{task}(u,v)|^2 \cdot TTF^2(u,v) \cdot E(u,v)^2 dudv]^2}{\iint |W_{task}(u,v)|^2 \cdot TTF^2(u,v) \cdot NPS(u,v) \cdot E(u,v)^4 dudv}$$

where u and v are the spatial frequencies in the x-and y-directions, E the eye filter that models the human visual system sensitivity to different spatial frequencies, and W(u,v) the task function. The detection of small HCC task was assumed to represent the circular signal with 15 mm diameter. The software computed the d' under the interpretation condition of 1.5 zoom factor and a viewing distance of 500 mm.
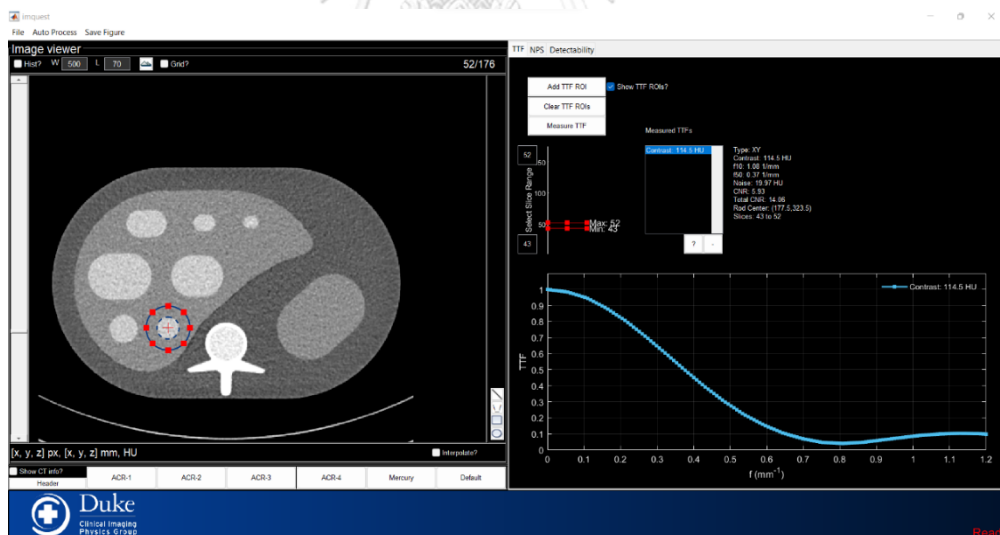


**Figure 4.11** The measurement of TTF from QRM liver nodule phantom image using imQuest software.
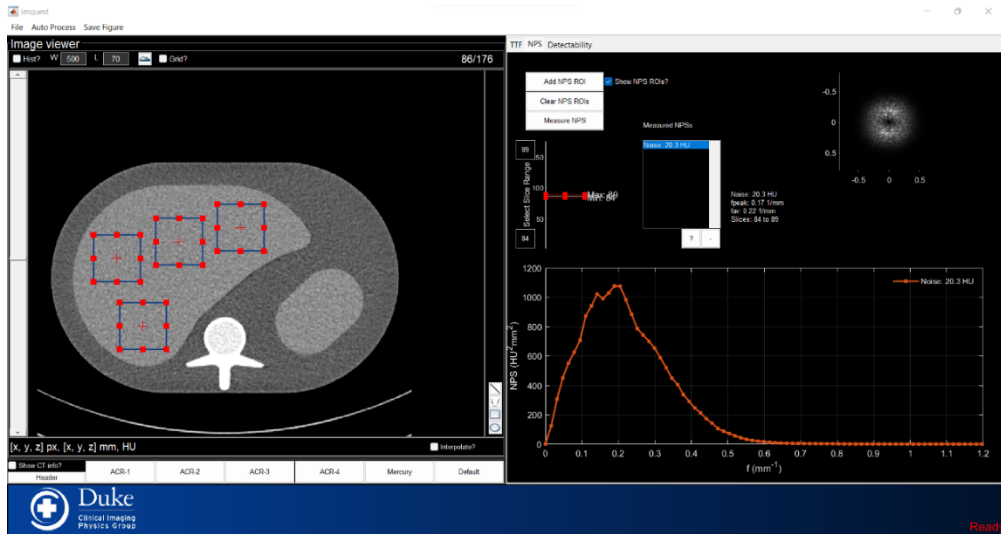
**Figure 4.12** The measurement of NPS from QRM liver nodule phantom image using imQuest software.
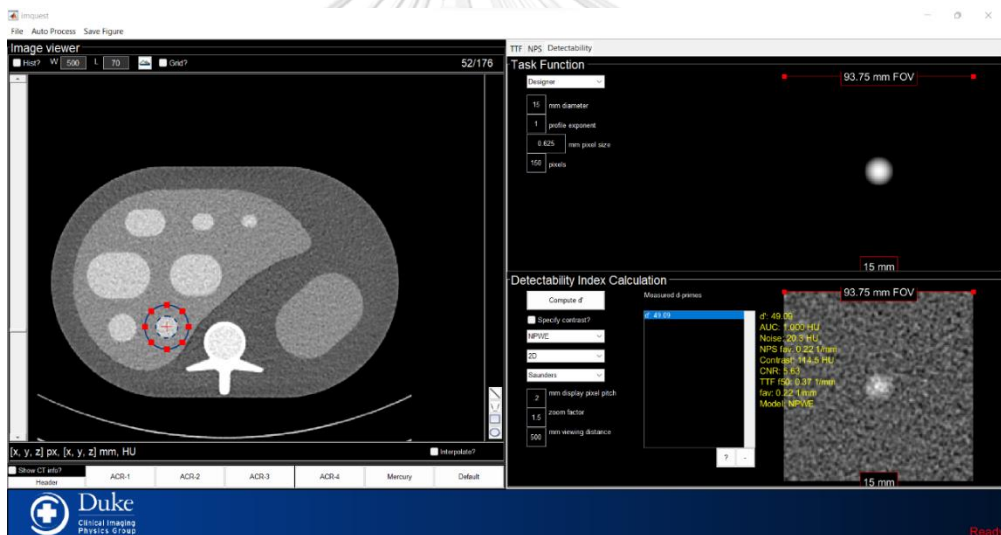


**Figure 4.13** The obtained d' from QRM liver nodule phantom image using imQuest software.
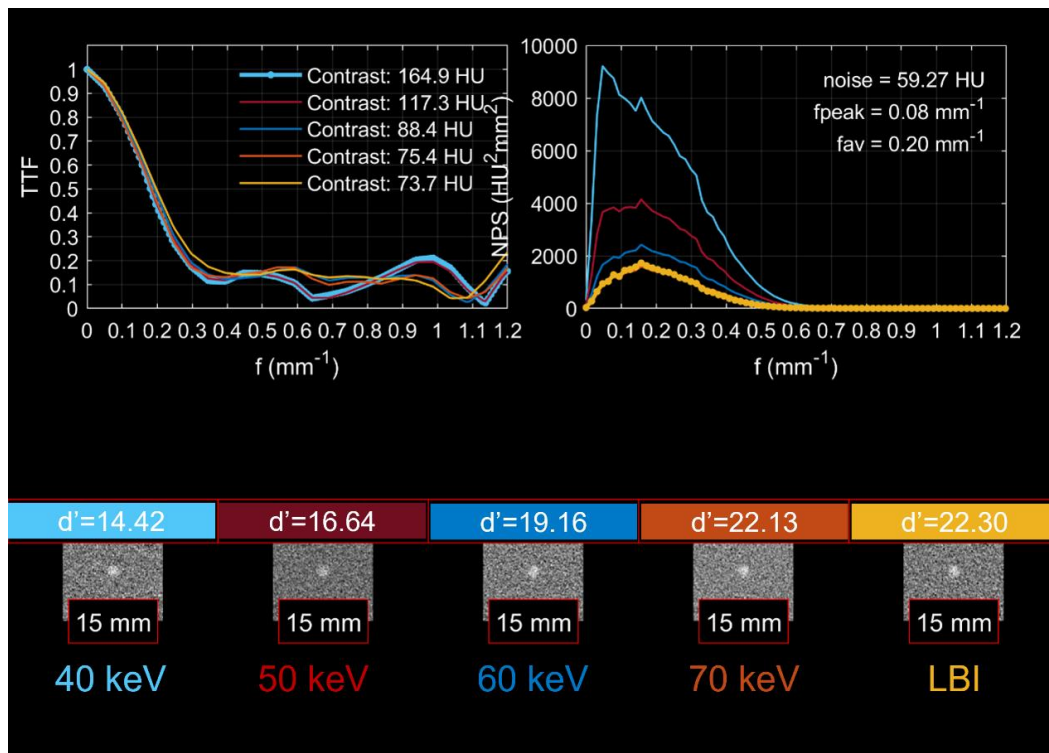
**Figure 4.14** The example of the TTF, NPS and d' summary result by imQuest software, measured at VMI 40-70 keV-VMI and LBI generated from 90/Sn150 DECT acauisition at pitch of 0.6 in large phantom.

### 4.2.5 Iodine quantification

The iodine concentration was quantified by using Liver VNC application profile in Dual Energy application in Syngo.Via software. The circular dual energy ROIs were drawn within the iodine regions on phantom images to measure the iodine concentration (mgI/cc) (Figure 4.15). The absolute value of subtraction between measured iodine concentration and true iodine concentration indicates the absolute iodine quantification error as follow:

$$\text{absolute iodine quantification error} = |\text{measured value} - \text{true value}|$$

and the percentage of iodine quantification error is equal to :

$$\text{percentage of iodine quantification error} = \left[\frac{\text{measured value} - \text{true value}}{\text{true value}}\right] \times 100$$

These were computed among the different parameter settings.

**Figure 4.15** The measurement of iodine concentration from iodine images in DECT using Liver VNC in Dual Energy application on Syngo.Via software.

### 4.2.6 Determination of hepatic lesion detectability in DECT

The obtained task-based image quality metric (NPS, TTF, d') and iodine quantification error for different acquisition parameters and various lesion and phantom sizes were reported in tabulate form. In addition, the obtained results were also plotted to demonstrate which factors influence the hepatic lesion detectability on dual-energy CT imaging. The minimum and maximum lesion detectability for each phantom size in accordance with different factors were reported.

# CHAPTER 5
# RESULTS

The task-based image quality and CNR for 40-70 keV-VMI and LBI acquired from DECT with varying the kV combinations; 80/Sn150,90/Sn150 and 100/Sn150 kVp were obtained for various size of phantom under tube current modulation are shown in Table 5.1.

**Table 5.1** The summary of task-based image quality; NPS, TTF at 50% ($f_{50}$), $d'$ and conventional image quality metric (contrast to noise ratio: CNR), obtained from 40-70 keV-VMI and LBI acquired from DECT with varying the kV combinations in small, medium, and large phantom sizes.

| Phantom size | IQ -metric | kV combination | VMI-DECT (keV) | | | | LBI | 120 kVp SECT |
|---|---|---|---|---|---|---|---|---|
| | | | 40 | 50 | 60 | 70 | | |
| Small | Noise Magnitude (HU) | 80/Sn150 | 39.81 | 28.77 | 22.14 | 18.11 | 18.25 | 18.56 |
| | | 90/Sn150 | 42.99 | 30.98 | 23.78 | 19.41 | 19.04 | |
| | | 100/Sn150 | 45.85 | 33.04 | 25.32 | 20.63 | 20.18 | |
| | $f_{av}(mm^{-1})$ | 80/Sn150 | 0.212 | 0.219 | 0.224 | 0.226 | 0.212 | 0.227 |
| | | 90/Sn150 | 0.216 | 0.223 | 0.229 | 0.231 | 0.220 | |
| | | 100/Sn150 | 0.217 | 0.225 | 0.231 | 0.234 | 0.215 | |
| | $f_{peak}(mm^{-1})$ | 80/Sn150 | 0.110 | 0.173 | 0.173 | 0.173 | 0.157 | 0.173 |
| | | 90/Sn150 | 0.110 | 0.189 | 0.205 | 0.205 | 0.173 | |
| | | 100/Sn150 | 0.157 | 0.157 | 0.157 | 0.157 | 0.142 | |
| | $f_{50}(mm^{-1})$ | 80/Sn150 | 0.215 | 0.217 | 0.224 | 0.233 | 0.333 | 0.298 |
| | | 90/Sn150 | 0.266 | 0.263 | 0.267 | 0.274 | 0.306 | |
| | | 100/Sn150 | 0.233 | 0.253 | 0.267 | 0.284 | 0.364 | |
| | $d'$ | 80/Sn150 | 30.63 | 33.90 | 35.96 | 36.41 | 29.10 | 40.88 |
| | | 90/Sn150 | 27.96 | 30.54 | 32.19 | 32.29 | 32.16 | |
| | | 100/Sn150 | 26.43 | 27.78 | 30.35 | 30.56 | 25.45 | |
| | CNR | 80/Sn150 | 5.04 | 5.05 | 4.87 | 4.68 | 3.97 | 4.55 |
| | | 90/Sn150 | 4.41 | 4.41 | 4.32 | 4.20 | 4.16 | |
| | | 100/Sn150 | 4.51 | 4.00 | 3.77 | 3.52 | 3.09 | |
| Medium | Noise Magnitude (HU) | 80/Sn150 | 47.69 | 34.38 | 26.44 | 21.55 | 21.42 | 24.41 |
| | | 90/Sn150 | 51.08 | 36.54 | 27.82 | 22.55 | 22.48 | |
| | | 100/Sn150 | 52.67 | 37.73 | 28.74 | 23.27 | 22.48 | |

|  | | | | | | | | |
|---|---|---|---|---|---|---|---|---|
| | $f_{av}$(mm$^{-1}$) | 80/Sn150 | 0.199 | 0.206 | 0.213 | 0.215 | 0.203 | 0.223 |
| | | 90/Sn150 | 0.199 | 0.208 | 0.215 | 0.218 | 0.206 | |
| | | 100/Sn150 | 0.203 | 0.212 | 0.218 | 0.221 | 0.206 | |
| | $f_{peak}$(mm$^{-1}$) | 80/Sn150 | 0.079 | 0.094 | 0.142 | 0.157 | 0.126 | 0.173 |
| | | 90/Sn150 | 0.063 | 0.157 | 0.157 | 0.157 | 0.157 | |
| | | 100/Sn150 | 0.079 | 0.157 | 0.157 | 0.173 | 0.157 | |
| | $f_{50}$(mm$^{-1}$) | 80/Sn150 | 0.223 | 0.233 | 0.232 | 0.239 | 0.300 | 0.330 |
| | | 90/Sn150 | 0.200 | 0.205 | 0.211 | 0.218 | 0.266 | |
| | | 100/Sn150 | 0.186 | 0.191 | 0.197 | 0.204 | 0.266 | |
| | $d'$ | 80/Sn150 | 17.14 | 18.94 | 22.19 | 22.00 | 21.93 | 29.81 |
| | | 90/Sn150 | 18.09 | 19.85 | 21.34 | 21.36 | 22.94 | |
| | | 100/Sn150 | 21.79 | 25.35 | 29.35 | 30.69 | 22.94 | |
| | CNR | 80/Sn150 | 3.38 | 3.29 | 3.40 | 3.22 | 3.13 | 3.40 |
| | | 90/Sn150 | 3.53 | 3.39 | 3.22 | 3.04 | 3.12 | |
| | | 100/Sn150 | 4.40 | 4.25 | 4.08 | 3.89 | 3.12 | |
| Large | Noise Magnitude (HU) | 80/Sn150 | 52.54 | 37.73 | 28.82 | 23.41 | 23.65 | 27.60 |
| | | 90/Sn150 | 56.07 | 39.98 | 30.30 | 24.43 | 23.57 | |
| | | 100/Sn150 | 57.15 | 40.74 | 30.86 | 24.85 | 23.58 | |
| | $f_{av}$(mm$^{-1}$) | 80/Sn150 | 0.184 | 0.192 | 0.199 | 0.202 | 0.197 | 0.217 |
| | | 90/Sn150 | 0.188 | 0.196 | 0.203 | 0.206 | 0.199 | |
| | | 100/Sn150 | 0.184 | 0.194 | 0.203 | 0.207 | 0.195 | |
| | $f_{peak}$(mm$^{-1}$) | 80/Sn150 | 0.063 | 0.094 | 0.157 | 0.157 | 0.142 | 0.173 |
| | | 90/Sn150 | 0.063 | 0.079 | 0.142 | 0.142 | 0.142 | |
| | | 100/Sn150 | 0.063 | 0.063 | 0.126 | 0.126 | 0.142 | |
| | $f_{50}$(mm$^{-1}$) | 80/Sn150 | 0.219 | 0.223 | 0.228 | 0.248 | 0.201 | 0.250 |
| | | 90/Sn150 | 0.063 | 0.079 | 0.142 | 0.142 | 0.235 | |
| | | 100/Sn150 | 0.063 | 0.063 | 0.126 | 0.126 | 0.257 | |
| | $d'$ | 80/Sn150 | 12.05 | 13.94 | 15.69 | 16.22 | 22.31 | 20.30 |
| | | 90/Sn150 | 15.59 | 16.51 | 18.74 | 19.38 | 21.01 | |
| | | 100/Sn150 | 11.52 | 14.13 | 17.49 | 20.34 | 19.25 | |
| | CNR | 80/Sn150 | 2.83 | 2.88 | 2.86 | 2.71 | 3.42 | 2.48 |
| | | 90/Sn150 | 3.54 | 3.31 | 3.39 | 3.31 | 3.42 | |
| | | 100/Sn150 | 2.99 | 3.09 | 3.17 | 3.26 | 3.21 | |

## 5.1 Task Transfer Function (TTF)

For the liver nodule inserted, the TTF curves were computed for different energies of VMI, LBI and 120 kVp SECT images as a function of kV combinations and phantom sizes (small, medium, and large), were demonstrated in Figure 5.1. The results showed that as increased the energy level from 40 to 70 keV, most of the TTF values increased except for 100/Sn150 scan at large phantom. In addition, when compared to the reference values at 120 kVp SECT scan (black dot line), the TTF values were comparable or less dependency at 90/Sn150 in small and large phantom size and at 100/Sn150 in large phantom size. For the small phantom size with 80/Sn150 and medium phantom size at all kV combinations the TTF curves from VMI were lower than 120 kVp SECT scan. The linear blended images acquired at 80/Sn150 and 100/Sn150 kVp exhibited the higher TTF values compared to the 120 kVp SECT at small phantom size while the comparable values were found at 90/Sn150 kVp in small phantom, 80/Sn150 kVp in medium phantom and 90/Sn150 and 100/Sn150 kVp in large phantom.

The spatial frequency at 50%TTF or $f_{50}$ (mm$^{-1}$) were extracted from TTF curve and plotted against the various parameters. For the different energy level of VMI, our results showed that the maximum $f_{50}$ values were highest at 70 keV for all kV combinations and all phantom sizes except for 100/Sn150 kV combination scan in large phantom which the highest $f_{50}$ was found at 40 keV-VMI. The $f_{50}$ shifted to higher frequency as increasing the energy level of VMI images, except for the using of 100/Sn150 at large phantom size that $f_{50}$ slightly shifted to lower frequency as increased the energy level.

The effects of the kV combinations in DECT to the TTF were also demonstrated in Figure 5.3. The results showed that using the using, the $f_{50}$ has mild degree of size dependence by small reduction of $f_{50}$ when increases the phantom sizes, but there was a size dependent to the TTF in 90/- and 100/Sn150 kV combinations. In addition to the TTF, the contrast (HU) between lesion to liver background from QRM liver nodule phantom was also reported from TTF measurement. The result demonstrated the contrast improvement in low keV VMI images as contrast increases when VMI energy decreased (Figure 5.3).
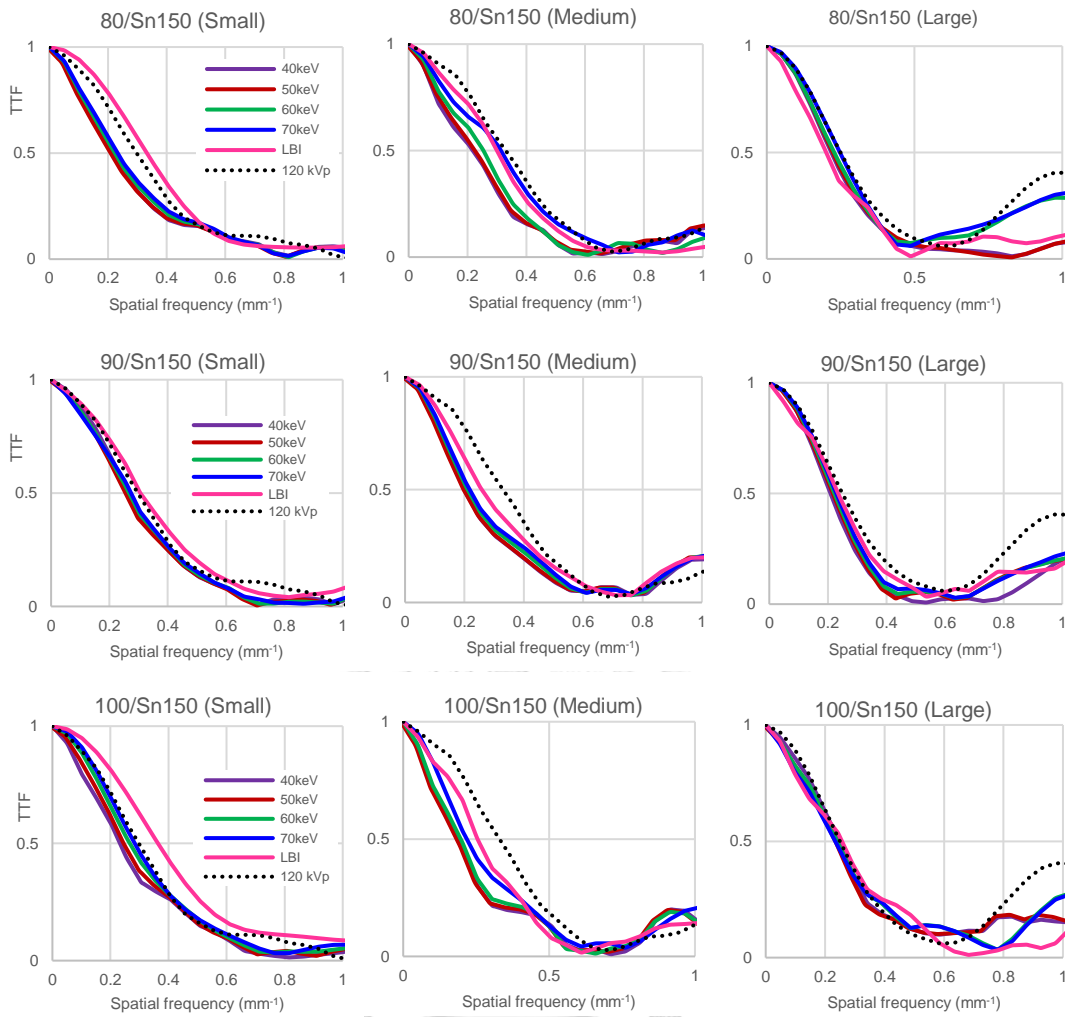
Figure 5.1 The TTF curves measured from different type of images; VMI at 40-70 keV, LBI, obtained from DECT acquisition with different kV combination settings for small, medium, and large phantom.
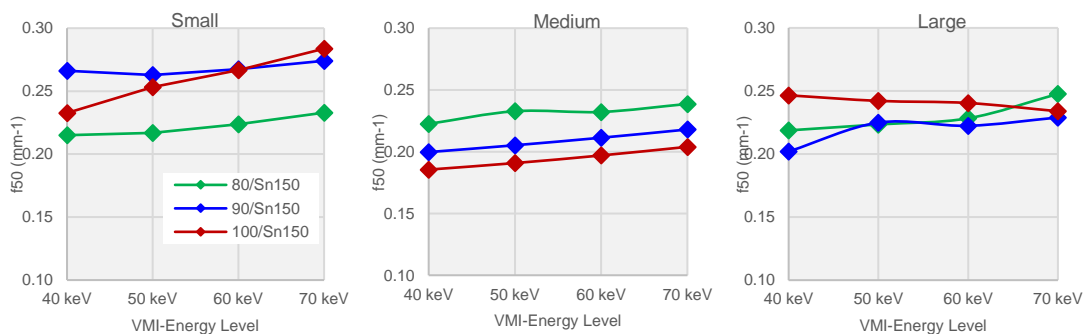


Figure 5.2 The $f_{50}$ values were plotted for different energy level of VMI for 80/Sn150, 90/Sn150 and 100/Sn150 in small medium and large phantom.

| 80/Sn150 | 90/Sn150 | 100/Sn150 |
| (a) | (b) | (c) |



| (d) | (e) | (f) |
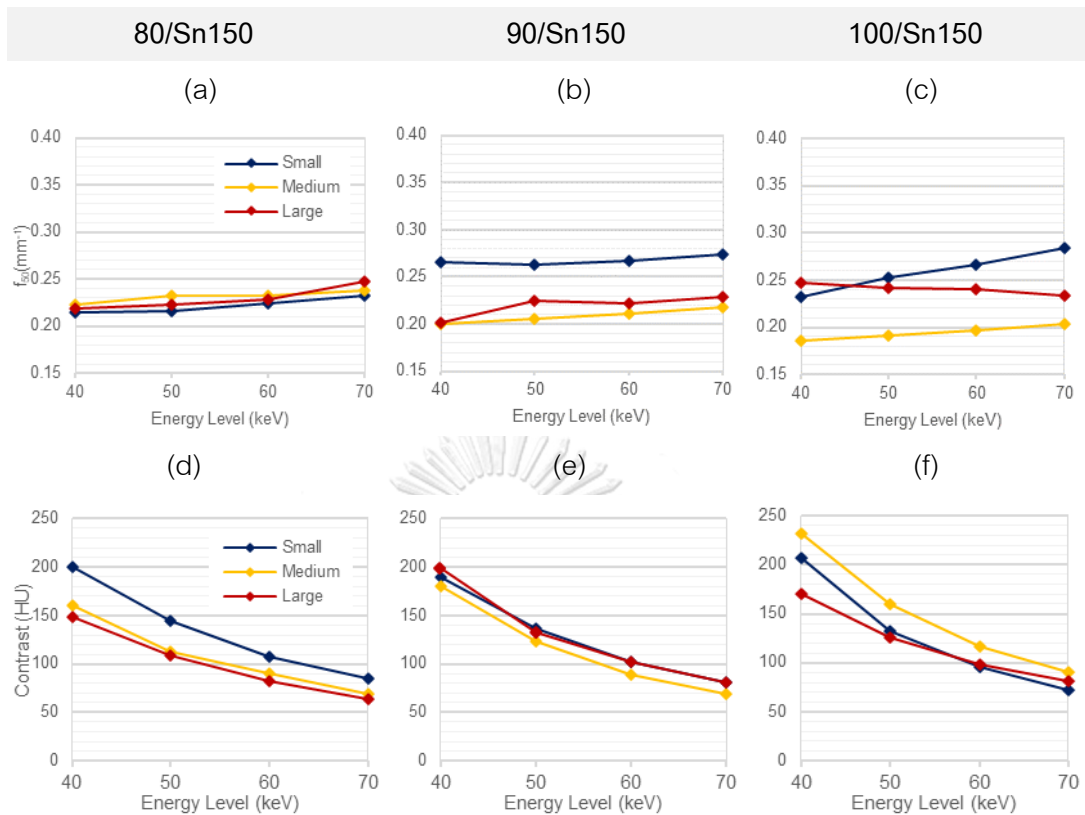


**Figure 5.3** The obtained 50%TTF ($f_{50}$) values (top row) and contrast (HU) ( bottom row ) were plotted against the different energy levels of VMI in DECT generated from three kVp combinations of 80/Sn150 (a), 90/Sn150 (b) and 100/Sn150 (c) for various phantom sizes (small, medium, and large).

The TTF of different synthetic image types from DECT were also investigated by comparing the $f_{50}$ from 70 keV-VMI and LBI to 120 kVp SECT. The results showed in Figure 5.4 where the black dot line represents 120 kVp SECT, blue line represents 70 keV VMI and pink line represents LBI. This study showed that the LBI was superior in spatial resolution (higher $f_{50}$) to the 120 kVp SECT in small phantom size for all kV combinations .whereas the 70 keV-VMI has inferior in spatial resolution compared to 120 kVp SECT image and LBI , except at 80/Sn150 for large phantom size.

**Figure 5.4** The 50%TTF ($f_{50}$) values for two type of synthetic images (70 keV-VMI and LBI) generated from DECT acquisition using 80/-,90/- and 100/Sn150 kV combinations; compared to 120 kVp SECT in small, medium, and large phantom.
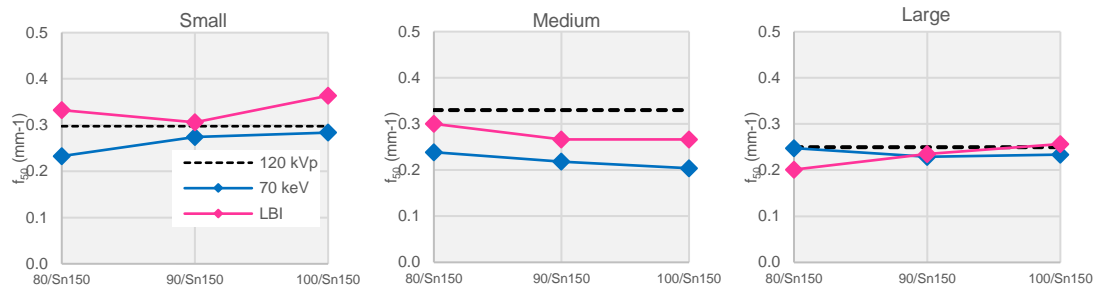
## 5.2 Noise power spectrum (NPS)

The magnitude of noise (HU) as a function of keV for each kV combination were demonstrated in Figure 5.5. The noise magnitude increased as increase the phantom size and decreasing the VMI-energy from 70 to 40 keV. The effect of kVp combination was reported as increasing the kV on tube A (low kV) from 80 to 100 kV the noise magnitude increased for all phantom size. The highest noise magnitude of VMI was found at 40 keV obtained from 100/Sn150 kV in large phantom and the lowest was found at 70 keV obtained from 80/Sn150 in small phantom.

The average NPS spatial frequency (mm$^{-1}$) values shifted to higher frequency as increasing the energy level from 40 to 70 keV. Lowering the kV on an x-ray tube A (low kV) from 100 to 80 kV the $f_{av}$ of VMI shifted to lower frequencies in all VMI energy levels and all phantom sizes (Figure 5.5). The $f_{av}$ shifted to lower frequency was also found when increasing the phantom size.
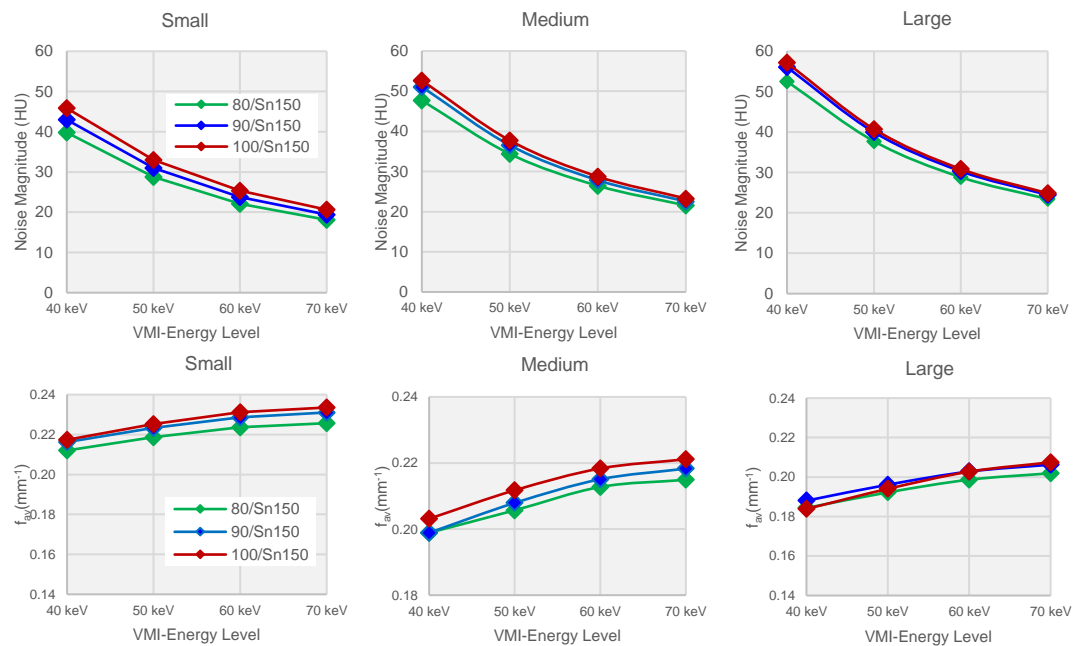
**Figure 5.5** Noise magnitude (HU) obtained in the 40-70 keV-VMI from 80-/90- and 100/Sn150 kVp combinations in DECT for small, medium, and large phantom (top row). The average NPS spatial frequency ($f_{av}$) obtained in the 40-70 keV VMI from 80-/90- and 100/Sn150 kVp combinations in DECT for small, medium, and large phantom (bottom row).

The characteristic of NPS among the different types of synthetic image from DECT were depicted in Figure 5.6. The lower noise magnitude in 70 keV- VMI and LBI compared to 120 kVp SECT images was found in medium and large phantom sizes but the slightly higher of noise magnitude was found in small phantom with 90/- and 100/Sn150 kV scan whereas the comparable noise magnitude was found in small phantom size at 80/Sn150 kV scan. In part of average NPS spatial frequency (mm$^{-1}$) values that indicated the noise texture, as compared to 120 kVp scan, the $f_{av}$ of 70 keV-VMI were slightly higher than that in 120 kVp scan for small phantom size at 90/- and 100/Sn150 kV but for the medium and large phantom size the $f_{av}$ shifted to the lower frequency compared to 120 kVp scan in all kV combinations. The linear blended images (LBI) shifted the $f_{av}$ of NPS to the lower frequency in all phantom sizes and kV combinations compared to 120 kVp image and 70 keV-VMI.
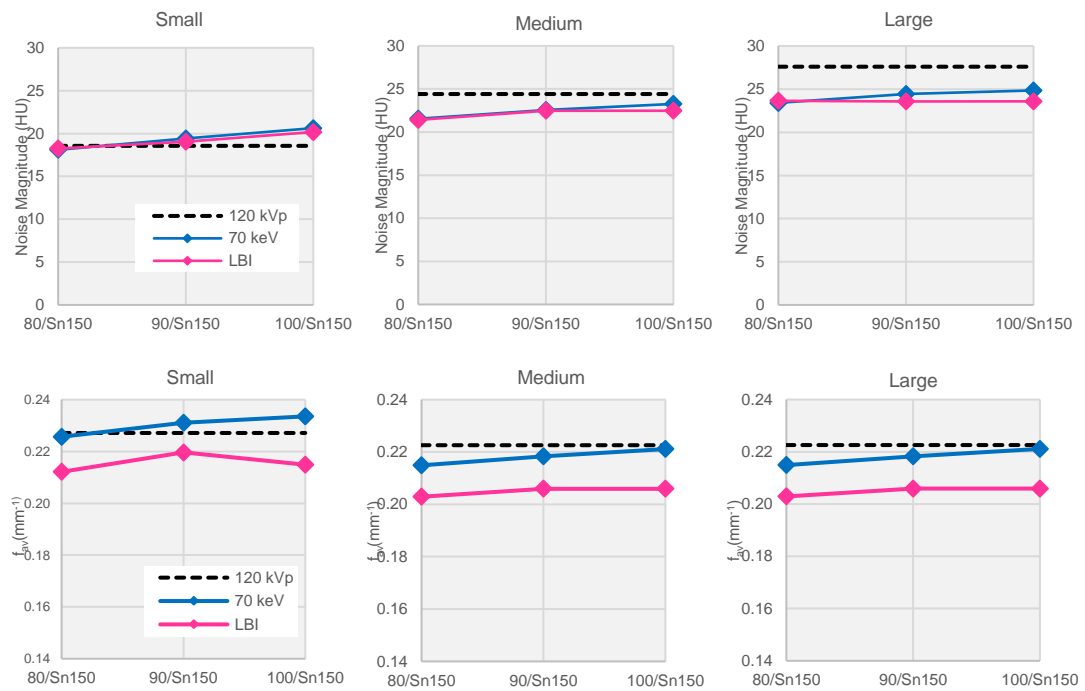
**Figure 5.6** The noise magnitude (top row) and average NPS spatial frequency ($f_{av}$) (bottom row) values for two type of synthetic images (70 keV-VMI and LBI) generated from DECT acquisition using 80/-,90/- and 100/Sn150 kV combination; compared to 120 kVp SECT in small, medium, and large phantom.

## 5.3 Detectability index (d')

The detectability index (d') was computed based on the detection task of 15 mm hyper-attenuated liver lesion. The d' estimated for virtual monoenergetic images at low energy level from 40 to 70 keV acquired under three kV combinations settings for all phantom sizes, the obtained d' values were shown in Figure 5.7 (top row). The results showed that the d' decreased with increased phantom sizes. The effect of energy level of VMI was demonstrated as increased of d' as the increased energy level of VMI. This results to the highest d' at 70 keV in all phantom sizes and all kV combinations. For small phantom size, the DECT acquired under 80/Sn150 kV provided the highest d' in VMI and highest under 100/Sn150 in medium phantom size. In the large phantom size using 90/Sn150 seem to yield the highest d' along with the VMI energy levels however at 70 keV, the used of 100/Sn150 provide the slightly higher d'.

The results of conventional metric as a contrast to noise ratio (CNR) were also computed and shown in Figure 5.7 (bottom row). The CNR behaved inversely to the d', as increasing the energy level from 40 to 70 keV the CNR decreased, except only at 100/Sn150 kV acquisition in large phantom.
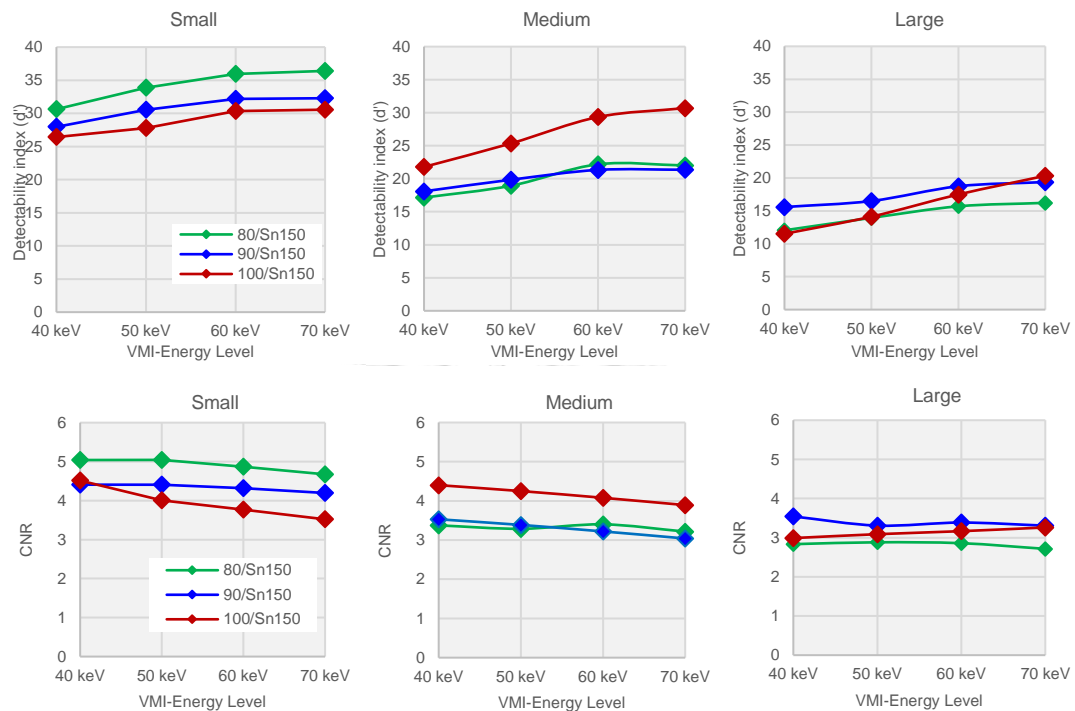


**Figure 5.7** The detectability index (d') obtained in the 40-70 keV-VMI from 80-/90- and 100/Sn150 kVp combinations in DECT for small, medium, and large phantom (top row). The contrast to noise ratio obtained in the 40-70 keV VMI from 80-/90- and 100/Sn150 kVp combinations in DECT for small, medium, and large phantom (bottom row).

The detectability index and CNR for the different image types were shown in Figure 5.8. Although the synthetic images from DECT showed inferior result of d' compared to the 120 kVp SECT scan in almost scanning conditions but for a large phantom size the LBI provide the comparable results in using of 90/- and 100/Sn150 kV and mild improved result in using of 80/Sn150 kV combination. The contrast to noise ratio showed some different results. The LBI and 70 keV-VMI provided the higher CNR than in 120 kVp SECT for large phantom size at all kV combinations, while the 70keV-VMI provides

the higher CNR than in 120 kVp SECT at the 80/Sn150 kV and 100/Sn150 kV combination in small and medium phantom respectively.
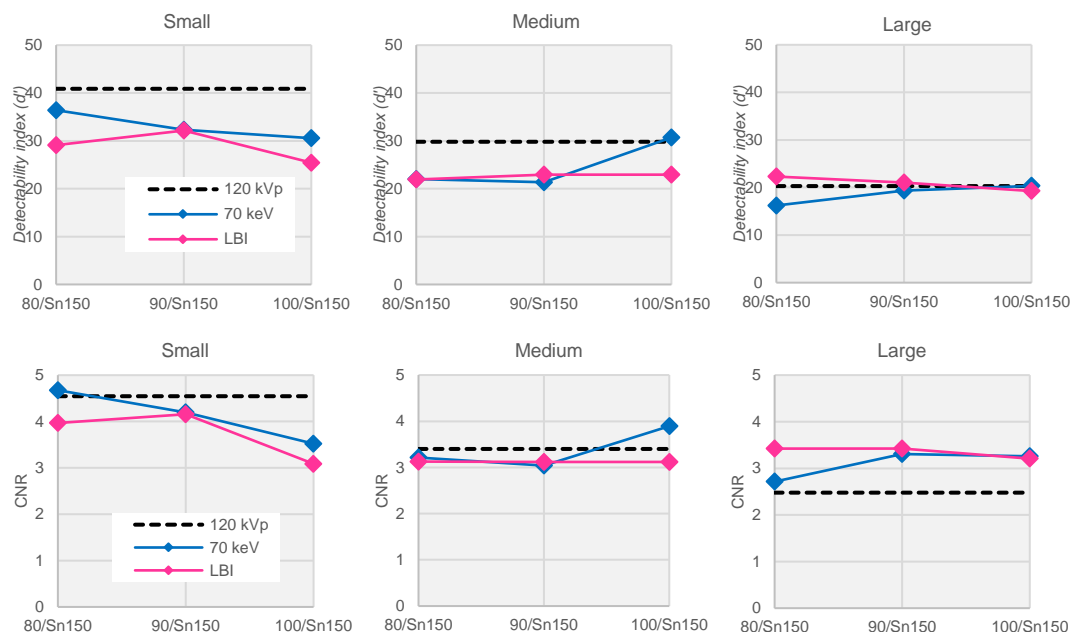


**Figure 5.8** The detectability index (top row) and contrast to noise ratio (bottom row) values for two type of synthetic images (70 keV-VMI and LBI) generated from DECT acquisition using 80/-,90/- and 100/Sn150 kV combination; compared to 120 kVp SECT in small, medium, and large phantoms.

## 5.4 Iodine quantification error

The measured iodine concentrations with DECT were strongly correlated with the true concentrations along the different iodine density in all kV combinations (Figure 5.9). The median, mean, standard deviation, minimum and maximum of the absolute iodine quantification error and percentage of iodine quantification error for different kV combinations were shown in Table 5.2. A comparison of absolute iodine quantification error (within a range of 1.0-5.0 mgI/cc) among different kV combinations showed that the absolute error at 80/Sn150 kV was lowest and error seem to increase as increasing the kV in low energy X-ray tube (tube A) from 80 to 100 kV but there is no significant difference of absolute iodine quantification error among the different kV combinations (P>0.05). In addition, the absolute iodine quantification error was no significant difference among different iodine concentration (P>0.05) (Table 5.3). For the results of normalized the iodine

quantification error shown as the percentage of iodine quantification error were not significant different among the different kV combinations (P>0.05). However, the percentage of error was found to be significant difference among the different iodine concentrations (P<0.05). However, when the iodine concentration at 1.0 mgI/cc was excluded, there was no significant difference of percentage of iodine quantification error among the different iodine concentrations.

To assess the reproducibility of measurement, the three scans were performed for each scan condition, the deviation of iodine concentration measurement bias ranged within 0.0-0.4 mgI/cc for 80/Sn150 kV, -0.3-0.3 mgI/cc for 90/Sn150 and -0.3-0.5 mgI/cc for 100/Sn150 kV combination (Figure 5.10). The limit of blank was also indicated by the maximum value of iodine concentration measured in a blank sample (0.0 mgI/cc), in our study these values were 0.4,0.3 and 0.3 mgI/cc for 80/-,90/-, and 100/Sn150 kV combination respectively. These results corresponding to the normalized percentage of iodine quantification error were shown in Figure 5.11, within the range of iodine concentration of 1.0-5.0 mgI/cc, the percentage of error tended to increase as decreasing the iodine concentration. The iodine quantification deviated within ±20% for concentration at 2.0-5.0 mgI/cc in all kV combinations. The highest percentage was found at 1.0 mgI/cc acquired from 100/Sn150 kV combination.

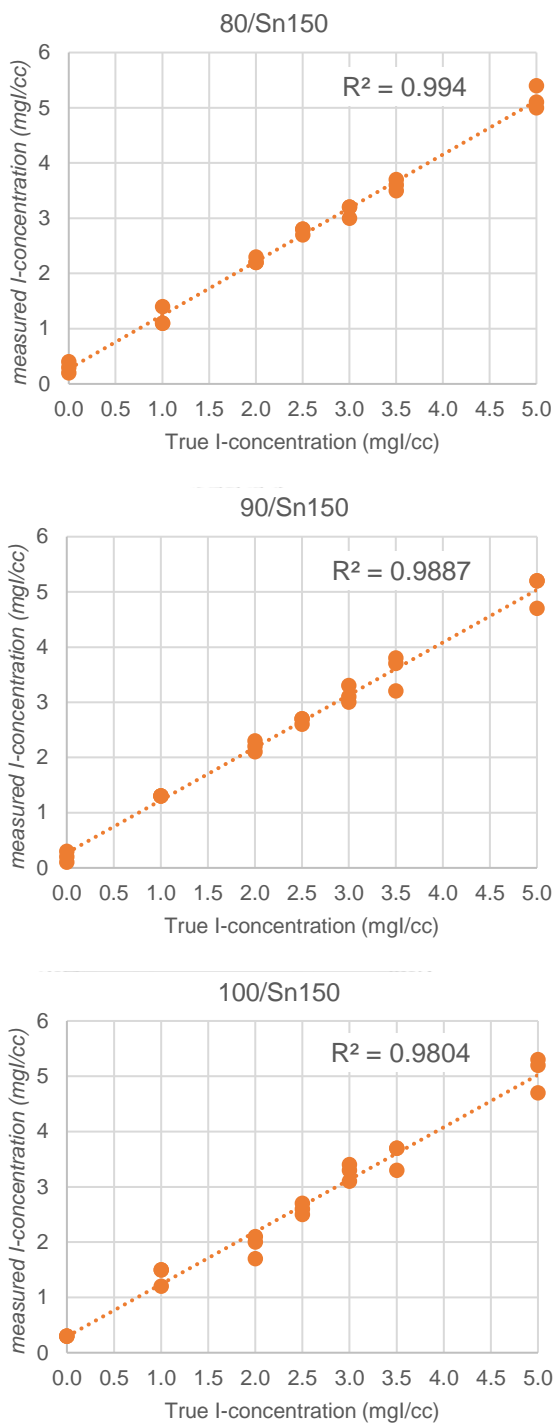**Figure 5.9** Scatterplots of measured iodine concentration (y-axis) versus the true concentrations (x-axis) in different kV combinations. The orange circles represent the observations, the lines represent a linear regression.

**Table 5.2** Absolute and percentage of iodine quantification error for low iodine concentration (1.0-5.0 mgI/cc) calculated in DECT images acquired with 3 kV-combinations.

| | Absolute iodine quantification error | | | | | | Percentage of iodine quantification error | | | | | |
|---|---|---|---|---|---|---|---|---|---|---|---|---|
| kV combination | median | mean | SD | min | max | p-value | median | mean | SD | min | max | P-value |
| 80/Sn150 | 0.20 | 0.18 | 0.125 | 0 | 0.4 | 0.619 | 8% | 8.8% | 0.090 | 0% | 40% | 0.999 |
| 90/Sn150 | 0.20 | 0.22 | 0.092 | 0 | 0.3 | | 7% | 8.9% | 0.111 | -9% | 30% | |
| 100/Sn150 | 0.20 | 0.23 | 0.145 | 0 | 0.5 | | 5% | 8.8% | 0.168 | -15% | 50% | |

**Table 5.3** Absolute and percentage of iodine quantification error from DECT acquisition for 1.0-5.0 mgI/cc iodine concentrations.

| | Absolute iodine quantification error | | | | | | Percentage of iodine quantification error | | | | | |
|---|---|---|---|---|---|---|---|---|---|---|---|---|
| Iodine Concentration | median | mean | SD | min | max | P-value | median | mean | SD | min | max | P-value |
| 1.0 mgI/cc | 0.30 | 0.30 | 0.150 | 0.1 | 0.5 | 0.440 | 30.0% | 30.0% | 0.150 | 10% | 50% | 0.001 |
| 2.0 mgI/cc | 0.20 | 0.19 | 0.105 | 0.0 | 0.3 | | 10.0% | 6.1% | 0.093 | -15% | 15% | |
| 2.5 mgI/cc | 0.20 | 0.18 | 0.097 | 0.0 | 0.3 | | 8.0% | 7.1% | 0.039 | 0% | 12% | |
| 3.0 mgI/cc | 0.20 | 0.18 | 0.139 | 0.0 | 0.4 | | 6.7% | 5.9% | 0.046 | 0% | 13% | |
| 3.5 mgI/cc | 0.20 | 0.19 | 0.093 | 0.0 | 0.3 | | 5.7% | 2.2% | 0.059 | -9.0% | 9.0% | |
| 5.0 mgI/cc | 0.20 | 0.22 | 0.120 | 0.0 | 0.4 | | 4.0% | 1.8% | 0.049 | -6.0% | 8.0% | |
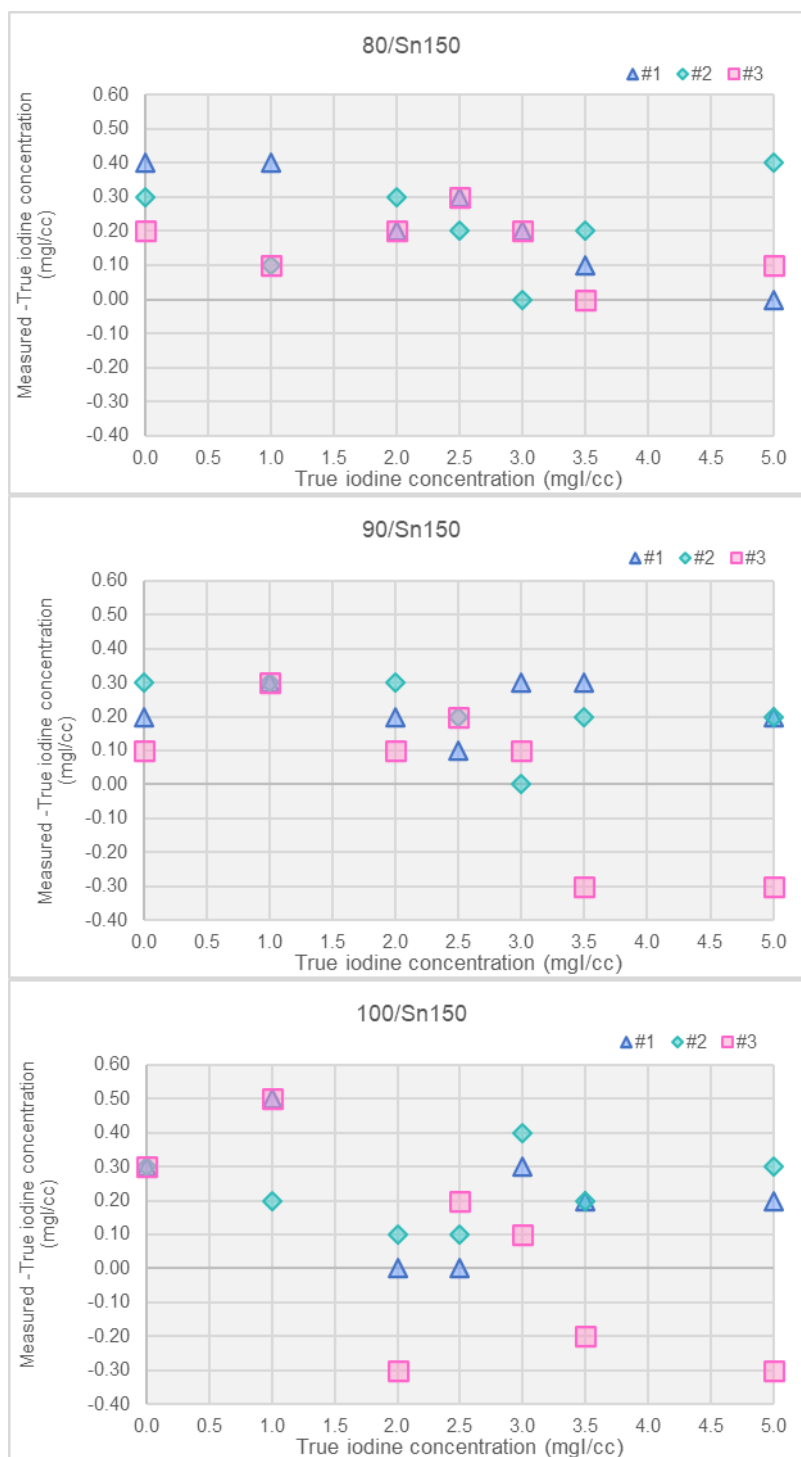
**Figure 5.10** Scattered plot of the difference between the DECT-measured Iodine concentrations and the true concentrations versus the true concentrations for 3 measurements (#1, #2, and #3 measurements) made in 0.0, 1.0, 2.0, 3.0, 3.5, and 5.0 mgI/cc).
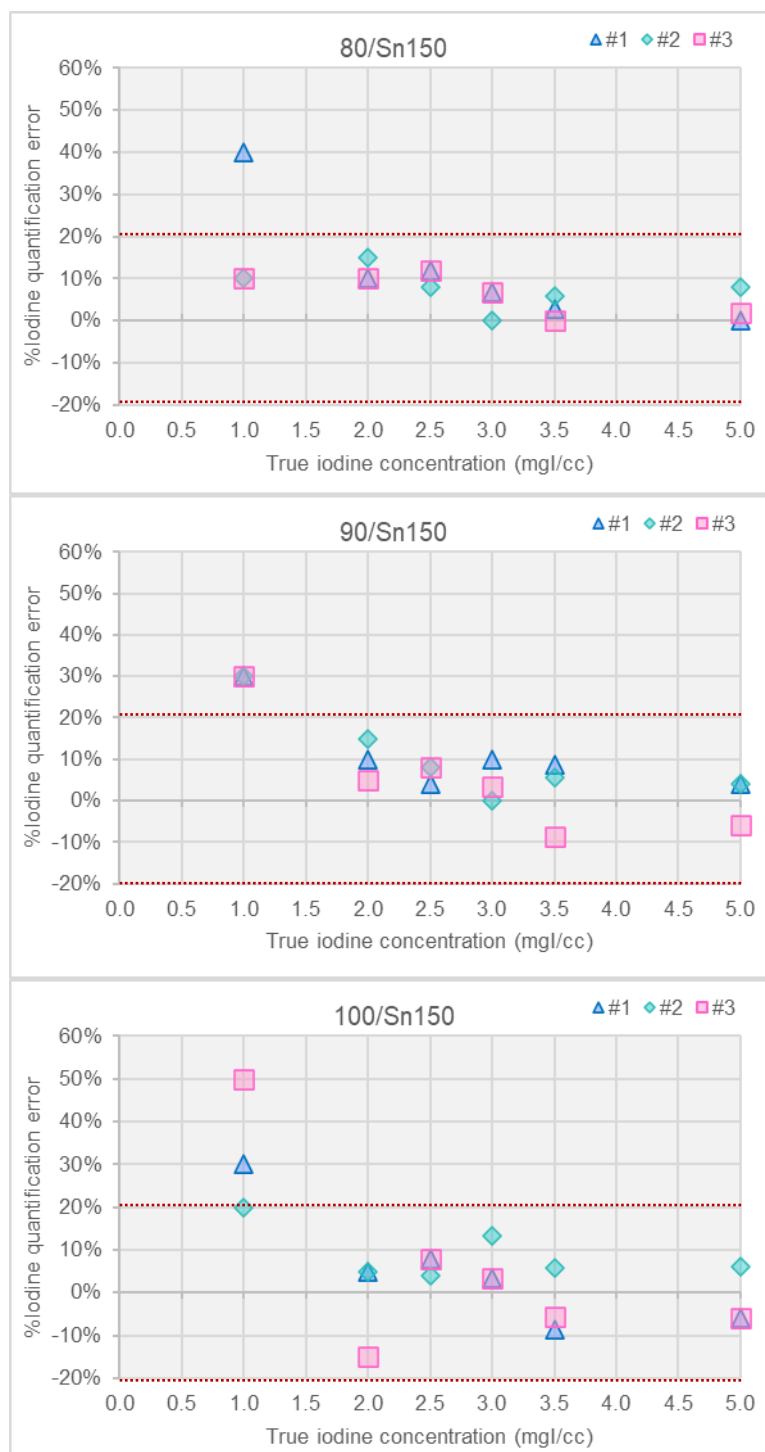
**Figure 5.11** Scattered plot of the percentage of iodine quantification error versus the true concentrations for 3 measurements (#1, #2, and #3 measurements) made in 0.0, 1.0, 2.0, 3.0, 3.5, and 5.0 mgI/cc. The red dot line indicates the range of error within ±20%.

# CHAPTER 6

# DISCUSSION

The utilizing the DECT in abdomen CT has been increasing in clinical practice with the expectation in improving of the detection and characterization of low contrast lesion especially in liver tumor imaging, compared to the conventional single energy scan. There are many clinical studies emphasized on the benefits of using DECT on lesion conspicuity and iodine quantification [9-12, 37, 38] in liver lesion and implemented them in the clinical abdomen DECT protocol in their centers. Typically, the radiologist utilized the different types of images for interpretation viewing with linear blended images (LBI) or 70 keV-VMI as the simulating of 120 kVp SECT, the low keV-VMI images (between 40-50 keV) to enhancing the contrast on lesions and improve lesion detection, and the material selective (iodine) image for the iodine quantification to characterize types of visualized tumor.

The study had been conducted to determine the clinically benefits on hepatic lesion detectability from different types of images (VMI and LBI) generated from abdomen DECT acquisition based on phantom study using the advance task-based image quality metrices of TTF, NPS and detectability index (d'). The detectability index is a method of non-pre-whitening observer model with eye filter (NPWE) that incorporate the spatial resolution, noise texture, diagnostic task, and 2D viewing conditions, changes of one of these factors influenced the d'. The factor affecting the hepatic lesion detectability was also performed to investigate the influence of DECT parameters (i.e., kVp combination, energy levels of VMI) to the lesion detection, along with the diversity of patient sizes.

The TTF was computed to assess the spatial resolution as a function of energy levels of VMI and kVp combination in various anthropomorphic abdomen phantom sizes. The result in this study showed that the spatial frequency at 50%TTF or $f_{50}$ of low keV (40-70 keV) virtual monoenergetic images shifted to higher frequency, improving the spatial resolution, as increasing the energy level from 40 to 70 keV. This result was different from the study of Greffier et al,[35] which the $f_{50}$ shifted toward lower frequencies with increasing energy level and the values were highest at 40 keV in dual source-DECT. Although, the

increasing of contrast between the simulated circular liver nodule and liver background as reducing the keV could improve the TTF results at low keV-VMI, but this study showed different findings. These were probably related to the dramatically increased of noise in low keV images deteriorating the edge sharpness of simulated circular liver nodule introduced the declining of ESF curve and shifted the TTF curve to the lower frequency. The deterioration of circular edge sharpness was demonstrated in Figure 6.1. Furthermore, this study used the IR techniques to reconstruct the images and the ATCM was activated for all acquisition protocols while the study of Greffier et al. did not.
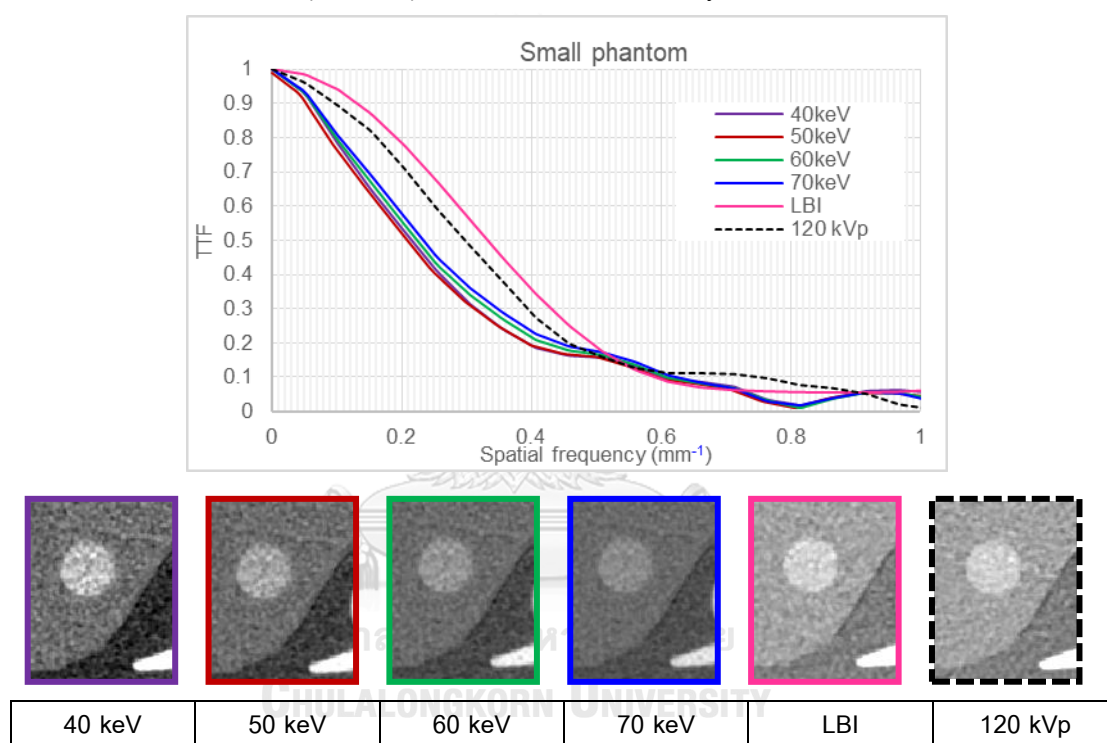


Figure 6.1 The obtained TTF curve for 40-, 50-,60-,70- keV, Linear blended image acquired from DECT with 80/Sn150 kV combination and 120 kVp SECT for small phantom size. The images of circular liver nodule insert for different images type and scanning acquisition used in the TTF calculation are displayed under the TTF curves.

In this study, the NPS was measured in different imaging conditions, our results demonstrated the increase of noise magnitude was found when lowering the VMI-energy level, increasing the kV on tube A and increasing the phantom size as previously reported in many phantom study.[35, 39, 40] The dual source dual energy CT used image based

method to reconstruct the virtual monoenergetic images using linear combination of two basis materials. The increase of noise magnitude in low keV-VMI was associated with a low signal-to-noise ratio on the photoelectric basis material images. This may be explained by the fact that the photoelectric attenuation is mainly determined by low energy photons which is more attenuated by the body, increasing the body thickness increases the low energy photon attenuation resulting to poor SNR and high noise even though the automatic tube current modulation is used to compensate for larger patient size (Figure 6.2).
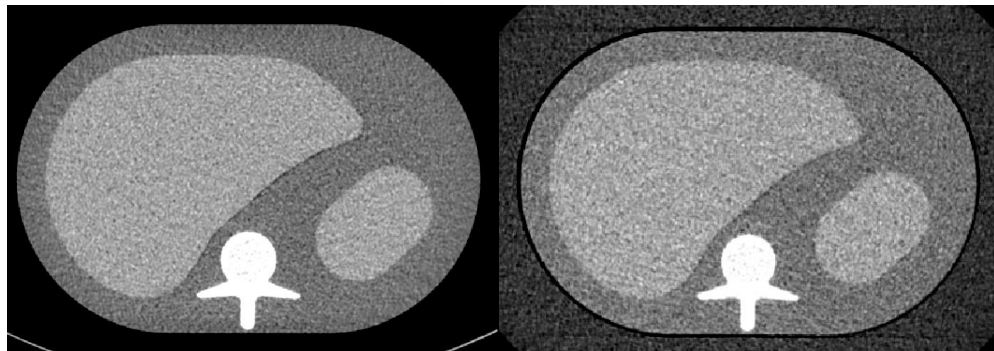


Figure 6.2 The 80-kV image obtained in small phantom (left) and 80-kV image obtained in large phantom (right) with increased the image noise.

The average spatial frequency of the NPS curves ($f_{av}$) shifted toward a lower frequency was observed in this study when imaged the phantom at lower kV on tube A and increased the phantom size as well as when decreased the VMI energy level from 70- to 40-keV. As previously published in several studies comparing the performance of iterative reconstruction algorithm, a shifted toward a lower frequency resulting in the modification of image texture to smoothen the images. The modifications of noise texture as a function of VMI energy level are illustrated in Figure 6.3.

The abdominal CT examination implies relatively low contrast diagnostic task compared to other organ pathology and sometime challenged with small focal lesions. Several studies selected conventional contrast-to-noise ratios (CNR) as a surrogate metric for low-contrast detectability. However, this first-order statistical metric could provide misleading results because it does not take into account on lesion size and contrast as well as noise texture.

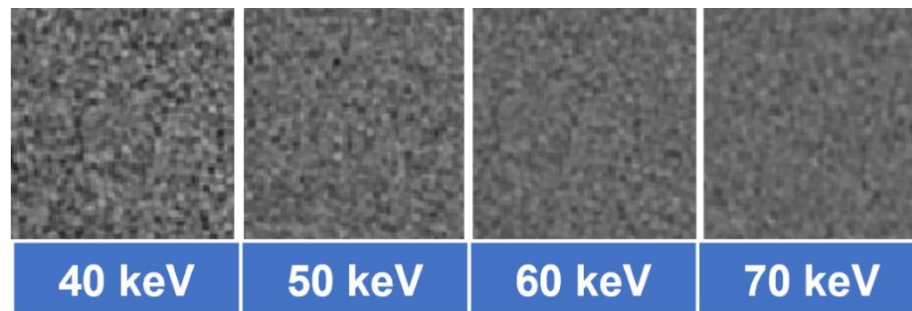**Figure 6.3** The crop of uniformed area in QRM liver phantom for each VMI energy levels.

The mathematical model observer had been used in this study to evaluate the small hepatic lesion detectability by quantifying the detectability index (d'). The detectability index estimates the radiologist's ability to perform clinical task, in this study the clinical task is the detection of a 15 mm hyperattenuating hepatic lesion which is the typical lesion size that small HCC is usually detected in CT examination [9, 10] and this size is in a range of clinically important to an effective treatment outcomes of HCC. [3, 14] The computation of d' strongly depends on signal magnitude and contrast, system resolution and human visual system and viewing conditions. The previous image quality metrics and their characteristics can be integrated into mathematical model observers, such as the non-prewhitening observer model with eye filter ($d'_{NPWE}$), to compute an overall detectability index. These model observers demonstrated a stronger correlation with human observer performance compared to CNR. As shown in Figure 5.7, the CNR behaves opposite to the d' that the highest CNR was found at 40 keV VM images whereas the highest d' was found at 70 keV images. The human observer study as performed by Hanson et al. [9] confirmed this finding that CNR was highest at 40 keV and yielded the highest conspicuity rank from radiologist but these images were not preferred for radiologist interpretation due to significant reduction in image quality, increase of noise and overall reader preference.

In this study, the highest d' was found at 70 keV-VMI acquired under 80/Sn150 for small phantom size reflecting to the imaging condition with lower images noise and high-resolution were obtained, even though the contrast was not so high as in lower keV images. Increasing the phantom size, the highest d' was found with the use of higher kV in tube A, in the setting of 100/Sn150 kV combination, provides the significant higher d'

compared to other kV combination in medium phantom size. This result related to the increased average beam energy when the kV in tube A was increasing, the penetration power of x-ray beam increased and therefore the noise was reduced and TTF was improved. In addition, the contrast for medium phantom was significant high at 100/Sn150 compared to other kV combination. Altogether, at all DECT imaging conditions, d' values were mostly influenced by the variation in contrast and NPS outcomes. Interestingly, for the large phantom size the highest d' was found at 90/Sn150 kV combination. This result demonstrated that the kV combination used for a phantom size affect to the d' nonlinearly. This can be explained by the different of mAs ratios between tube "A" and tube "B" defined by the manufacturer for each kV combination. Base on the quality reference mAs defined for abdomen DECT protocol in table 4.3, the mAs used for tube A was 2.0 times 80/Sn150 and 100/Sn150, and 1.5 times for 90/Sn150. This different mAs ratio affects to image quality, under the ATCM condition, lowering these ratio increases the proportion of high energy photon resulting in more penetrating photon in the beam and greater photon statistic in images, reducing the noise magnitude , photon starvation artifact and beam hardening effects, especially in large phantom size.

To link the physical phantom study to the clinical practice, the obtained $CTDI_{vol}$ for each phantom were preliminary matched to the clinical CT data from patient and the phantom size small, medium, and large were matched to the patient body weight of 60-, 75-, and 115-kg respectively. The result of this study could be implied that under the ATCM is activated ,changing the phantom size from small to large or double the patient size, the d' reduced by -55%, -40% and -33% for 80/-, 90/- and 100/Sn150 kV combination respectively. Therefore, selection of 100/Sn150 kV combination with increasing of quality reference mAs for larger phantom size may be required if deterioration of image quality or d' is unacceptable (i.e., detection of subtle or small hepatic lesion) is clinically important in obese patient, however the process should be optimized with careful consideration on dose reference levels among the medical physicist, technologist, and radiologist before implementation.

The characteristics of the 70 keV-VMI, and LBI had been investigated in this study which had been regularly used in clinical practice to simulate the 120 kVp image. According to our results, at 80/Sn150 kV, the d' at 70 keV-VMI was higher than LBI in small phantom, equivalent in medium phantom and become lower in the large phantom sizes. For the 90/Sn150 kV, this scanning condition showed the equivalent of d' between these two image types. However, when the 100/Sn150 kV was used, the 70 keV-VMI show superior on d' in all size of phantom, due to the significant increase of image contrast obtained in 70 keV-VMI than in LBI while the NPS value was not different between these two types of images.

Many previous studies performed the measurement of d' or iodine quantification error using the circular shape of phantom or with single standard size, [35, 37, 38, 40] while this study used the anthropomorphic phantom in the elliptical shape, with another two sizes of extension ring. This includes more clinical relevance from these results.

The DECT offers a method of quantifying the iodine concentration in mgI/cc. This application is additional benefit to assess the viability of tissue. This has been shown to improve lesion detection, their characterization and enable monitoring tumor treatment response in oncological imaging. [12, 41-43] This study aimed to evaluate the accuracy of iodine quantification based on the clinical application of HCC detection. Therefore, the low iodine concentration was analyzed with the range of concentration between 1.0-5.0 mgI/cc. The iodine quantification error was performed only for a single phantom size (small) as the preliminary study by including the variation on the kV combinations of 80/-, 90/-, and 100/Sn150 kV. In comparison between different kV combinations, within the range of 2.0-5.0 mgI/cc, the percentages of iodine quantification error were within ±20% for all kV combinations. However, at very low concentration at 1.0 mgI/cc, the use of 80/Sn150 kV provided better results compared to others. This is in accordance with Pelgrim et al.[44], who showed that larger photon energy separation leads to more accurate iodine quantification. However, the phantom study by Marin et al.[45] and Euler et al. [46] showed that the optimal voltage setting is dependent on phantom size. Therefore, the further study should be performed to cover the diversity in clinical practice such as more

phantom sizes, more iodine concentrations with variations of DECT scan and reconstruction parameters. This study performed the preliminary study on the accuracy of iodine quantification, the iodine solution was diluted using micropipette to create into different iodine concentrations. However, the accuracy of the series of dilution, which values was considered as the true iodine concentrations, has not been confirmed by any biochemical measurement method.

The limitations from this study are the acquisitions performed under automatic tube current modulation (ATCM) with only one quality reference mAs, and a single standard soft tissue reconstruction kernel was used. Additionally, the use of other parameter combinations may show different results. The clinical task in this study is to detect a single sized 15 mm diameter in circular, hyperattenuating hepatic lesion which is the typical detection task of HCC. The inclusion of more lesion sizes should be conducted, such as creating more difficult task by reducing the target diameter from 15 mm to 10 mm and investigate the d' results, to increase the clinically benefits and relevant.

## CHAPTER 7

## CONCLUSION

This study was conducted to determine the hepatic lesion detectability on abdomen dual energy CT for various phantom sizes and the investigation of factors affecting the detectability of hepatic lesion in abdomen dual energy CT imaging.

The mathematical model observer was employed to compute the detectability index (d') for a 15 mm circular hyperattenuating lesion reflecting to the clinical task of HCC detection. The results showed that the hepatic lesion detectability is dependent on phantom sizes and kVp combinations as well as the energy levels of virtual monoenergetic images and the results are different in linear blended images. For small phantom the imaging conditions yielded the highest detectability index at:  the acquisition with 80/Sn150 kV by utilizing the 70 keV VMI. For medium and large phantom size, utilizing the 70 keV VMI acquired from 100/Sn150 kV yields the highest detectability index. The additional benefits of DECT acquisition related to the hepatic lesion detection is the iodine quantification. Based on our preliminary result on small phantom size, the percentage of iodine quantification error in the range of 2.0-5.0 mgI/cc were within ±20% in all kV combination settings.

The detectability index incorporates the noise texture, spatial resolution, contrast, diagnostic task, and 2D viewing conditions. Change in any of these factors influences the d'. Under the same diagnostic task and viewing condition, the change of kVp combinations and energy levels of VMI along with the different phantom sizes impact the detectability index outcome, resulting to affect the hepatic lesion detectability in abdomen DECT.

# REFERENCES

1.      Sung H, Ferlay J, Siegel RL, Laversanne M, Soerjomataram I, Jemal A, et al. Global Cancer Statistics 2020: GLOBOCAN Estimates of Incidence and Mortality Worldwide for 36 Cancers in 185 Countries. CA Cancer J Clin. 2021;71(3):209-49.

2.      Primary Liver Cancer. 1 ed. Wu GY, editor: Humana Totowa, NJ; 2012. XII, 296 p.

3.      Thun M, Linet MS, Cerhan JR, Haiman CA, Schottenfeld D. Cancer epidemiology and prevention: Oxford University Press; 2017.

4.      Moon AM, Singal AG, Tapper EB. Contemporary Epidemiology of Chronic Liver Disease and Cirrhosis. Clin Gastroenterol Hepatol. 2020;18(12):2650-66.

5.      Haj-Mirzaian A, Kadivar A, Kamel IR, Zaheer A. Updates on Imaging of Liver Tumors. Curr Oncol Rep. 2020;22(5):46.

6.      Solomon J, Ba A, Bochud F, Samei E. Comparison of low-contrast detectability between two CT reconstruction algorithms using voxel-based 3D printed textured phantoms. Medical Physics. 2016;43(12):6497-506.

7.      Solomon J, Marin D, Choudhury KR, Patel B, Samei E. Effect of Radiation Dose Reduction and Reconstruction Algorithm on Image Noise, Contrast, Resolution, and Detectability of Subtle Hypoattenuating Liver Lesions at Multidetector CT: Filtered Back Projection versus a Commercial Model-based Iterative Reconstruction Algorithm. Radiology. 2017;284(3):777-87.

8.      Viry A, Aberle C, Racine D, Knebel JF, Schindera ST, Schmidt S, et al. Effects of various generations of iterative CT reconstruction algorithms on low-contrast detectability as a function of the effective abdominal diameter: A quantitative task-based phantom study. Phys Med. 2018;48:111-8.

9.      Hanson GJ, Michalak GJ, Childs R, McCollough B, Kurup AN, Hough DM, et al. Low kV versus dual-energy virtual monoenergetic CT imaging for proven liver lesions: what are the advantages and trade-offs in conspicuity and image quality? A pilot study. Abdom Radiol (NY). 2018;43(6):1404-12.

10.	Shuman WP, Green DE, Busey JM, Mitsumori LM, Choi E, Koprowicz KM, et al. Dual-energy liver CT: effect of monochromatic imaging on lesion detection, conspicuity, and contrast-to-noise ratio of hypervascular lesions on late arterial phase. AJR Am J Roentgenol. 2014;203(3):601-6.

11.	Muenzel D, Lo GC, Yu HS, Parakh A, Patino M, Kambadakone A, et al. Material density iodine images in dual-energy CT: Detection and characterization of hypervascular liver lesions compared to magnetic resonance imaging. Eur J Radiol. 2017;95:300-6.

12.	Kaltenbach B, Wichmann JL, Pfeifer S, Albrecht MH, Booz C, Lenga L, et al. Iodine quantification to distinguish hepatic neuroendocrine tumor metastasis from hepatocellular carcinoma at dual-source dual-energy liver CT. European Journal of Radiology. 2018;105:20-4.

13.	Trevisani F, Cantarini M, Wands J, Bernardi M. Recent advances in the natural history of hepatocellular carcinoma. Carcinogenesis. 2008;29(7):1299-305.

14.	Choi JY, Lee JM, Sirlin CB. CT and MR imaging diagnosis and staging of hepatocellular carcinoma: part I. Development, growth, and spread: key pathologic and imaging aspects. Radiology. 2014;272(3):635-54.

15.	Genant HK, Boyd D. Quantitative bone mineral analysis using dual energy computed tomography. Investigative radiology. 1977;12(6):545-51.

16.	Di Chiro G, Brooks RA, Kessler RM, Johnston GS, Jones AE, Herdt JR, et al. Tissue signatures with dual-energy computed tomography. Radiology. 1979;131(2):521-3.

17.	Avrin DE, Macovski A, Zatz L. Clinical application of Compton and photo-electric reconstruction in computed tomography: preliminary results. Investigative radiology. 1978;13(3):217-22.

18.	Millner MR, McDavid WD, Waggener RG, Dennis MJ, Payne WH, Sank VJ. Extraction of information from CT scans at different energies. Medical physics. 1979;6(1):70-1.

19.	Kelcz F, Joseph PM, Hilal SK. Noise considerations in dual energy CT scanning. Medical physics. 1979;6(5):418-25.

20.     Flohr TG, McCollough CH, Bruder H, Petersilka M, Gruber K, Süβ C, et al. First performance evaluation of a dual-source CT (DSCT) system. European radiology. 2006;16(2):256-68.

21.     Johnson TR, Krauss B, Sedlmair M, Grasruck M, Bruder H, Morhard D, et al. Material differentiation by dual energy CT: initial experience. European radiology. 2007;17(6):1510-7.

22.     McCollough CH, Boedeker K, Cody D, Duan X, Flohr T, Halliburton SS, et al. Principles and applications of multienergy CT: Report of AAPM Task Group 291. Medical Physics. 2020;47(7):e881-e912.

23.     Lehmann L, Alvarez R, Macovski A, Brody W, Pelc N, Riederer SJ, et al. Generalized image combinations in dual KVP digital radiography. Medical physics. 1981;8(5):659-67.

24.     Hubbell JH, Seltzer SM. Tables of X-ray mass attenuation coefficients and mass energy-absorption coefficients 1 keV to 20 MeV for elements Z= 1 to 92 and 48 additional substances of dosimetric interest. National Inst. of Standards and Technology-PL, Gaithersburg, MD (United …; 1995.

25.     Samei E, Bakalyar D, Boedeker KL, Brady S, Fan J, Leng S, et al. Performance evaluation of computed tomography systems: summary of AAPM task group 233. Medical physics. 2019;46(11):e735-e56.

26.     Solomon J, Wilson J, Samei E. Characteristic image quality of a third generation dual‐source MDCT scanner: Noise, resolution, and detectability. Medical physics. 2015;42(8):4941-53.

27.     Chen B, Christianson O, Wilson JM, Samei E. Assessment of volumetric noise and resolution performance for linear and nonlinear CT reconstruction methods. Medical physics. 2014;41(7):071909.

28.     Richard S, Husarik DB, Yadava G, Murphy SN, Samei E. Towards task‐based assessment of CT performance: system and object MTF across different reconstruction algorithms. Medical physics. 2012;39(7Part1):4115-22.

29.     Solomon JB, Christianson O, Samei E. Quantitative comparison of noise texture across CT scanners from different manufacturers. Medical physics. 2012;39(10):6048-55.

30.     Barrett HH, Myers KJ, Hoeschen C, Kupinski MA, Little MP. Task-based measures of image quality and their relation to radiation dose and patient risk. Physics in Medicine & Biology. 2015;60(2):R1.

31.     Christianson O, Chen JJ, Yang Z, Saiprasad G, Dima A, Filliben JJ, et al. An improved index of image quality for task-based performance of CT iterative reconstruction across three commercial implementations. Radiology. 2015;275(3):725-34.

32.     Solomon JB, Samei E. Correlation between human detection accuracy and observer model-based image quality metrics in computed tomography. Journal of Medical Imaging. 2016;3(3):035506.

33.     Dezaki ML, Ariffin MKAM, Hatami S. An overview of fused deposition modelling (FDM): Research, development and process optimisation. Rapid Prototyping Journal. 2021.

34.     Cheng Y, Smith TB, Jensen CT, Liu X, Samei E. Correlation of algorithmic and visual assessment of lesion detection in clinical images. Academic radiology. 2020;27(6):847-55.

35.     Greffier J, Frandon J, Sadate A, Akessoul P, Belaouni A, Beregi JP, et al. Impact of four kVp combinations available in a dual-source CT on the spectral performance of abdominal imaging: A task-based image quality assessment on phantom data. Journal of applied clinical medical physics. 2021;22(8):243-54.

36.     Verdun F, Racine D, Ott J, Tapiovaara M, Toroi P, Bochud F, et al. Image quality in CT: From physical measurements to model observers. Physica Medica. 2015;31(8):823-43.

37.     Wichmann JL, Hardie AD, Schoepf UJ, Felmly LM, Perry JD, Varga-Szemes A, et al. Single-and dual-energy CT of the abdomen: comparison of radiation dose and image quality of 2nd and 3rd generation dual-source CT. European radiology. 2017;27(2):642-50.

38.     Voss BA, Khandelwal A, Wells ML, Inoue A, Venkatesh SK, Lee YS, et al. Impact of dual-energy 50-keV virtual monoenergetic images on radiologist confidence in detection of

key imaging findings of small hepatocellular carcinomas using multiphase liver CT. Acta Radiologica. 2021:02841851211052993.

39.     Greffier J, Si-Mohamed S, Dabli D, de Forges H, Hamard A, Douek P, et al. Performance of four dual-energy CT platforms for abdominal imaging: a task-based image quality assessment based on phantom data. European Radiology. 2021;31(7):5324-34.

40.     Cester D, Eberhard M, Alkadhi H, Euler A. Virtual monoenergetic images from dual-energy CT: systematic assessment of task-based image quality performance. Quantitative Imaging in Medicine and Surgery. 2022;12(1):726.

41.     Martin SS, Weidinger S, Czwikla R, Kaltenbach B, Albrecht MH, Lenga L, et al. Iodine and fat quantification for differentiation of adrenal gland adenomas from metastases using third-generation dual-source dual-energy computed tomography. Investigative Radiology. 2018;53(3):173-8.

42.     Mulé S, Pigneur F, Quelever R, Tenenhaus A, Baranes L, Richard P, et al. Can dual-energy CT replace perfusion CT for the functional evaluation of advanced hepatocellular carcinoma? European Radiology. 2018;28(5):1977-85.

43.     Ascenti G, Sofia C, Mazziotti S, Silipigni S, D'Angelo T, Pergolizzi S, et al. Dual-energy CT with iodine quantification in distinguishing between bland and neoplastic portal vein thrombosis in patients with hepatocellular carcinoma. Clinical Radiology. 2016;71(9):938. e1-. e9.

44.     Pelgrim GJ, van Hamersvelt RW, Willemink MJ, Schmidt BT, Flohr T, Schilham A, et al. Accuracy of iodine quantification using dual energy CT in latest generation dual source and dual layer CT. European radiology. 2017;27(9):3904-12.

45.     Marin D, Pratts-Emanuelli JJ, Mileto A, Husarik DB, Bashir MR, Nelson RC, et al. Interdependencies of acquisition, detection, and reconstruction techniques on the accuracy of iodine quantification in varying patient sizes employing dual-energy CT. European radiology. 2015;25(3):679-86.

46.     Euler A, Solomon J, Mazurowski MA, Samei E, Nelson RC. How accurate and precise are CT based measurements of iodine concentration? A comparison of the

minimum detectable concentration difference among single source and dual source dual energy CT in a phantom study. European radiology. 2019;29(4):2069-78.

# APPENDIX I

# QUALITY CONTROL OF COMPUTED TOMOGRAPHY

Quality Control Report

| Site | Bumrungrad International Hospital |
|------|-----------------------------------|
| Manufacturer | SIEMENS |
| Model | Somatom Force |
| S/N | 75712 |
| Performed date | 8 Nov 2021 |

## 1. CT alignment Light

The CT alignment lights accuracy test shows the congruence of the scan localization light and the X ray field tomographic plane to confirm that the internal and external alignment lights are properly aligned with CT gantry and couch

a) To determine z-axis misalignment, measure the distance (d) between center of the ramp and center of the images. Multiply distance (d) by 0.42 to calculate z-axis misalignment.
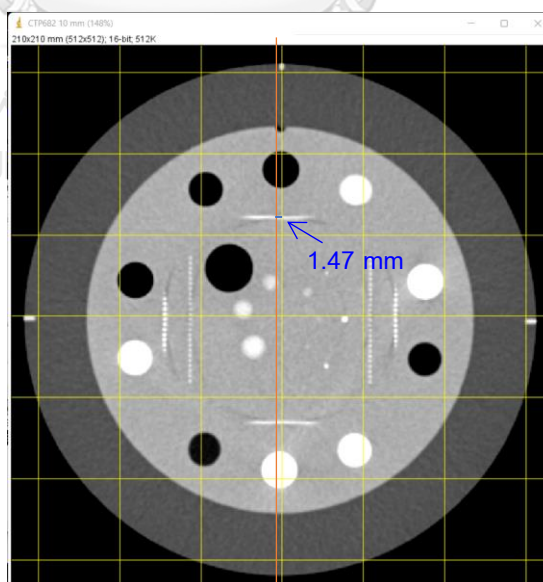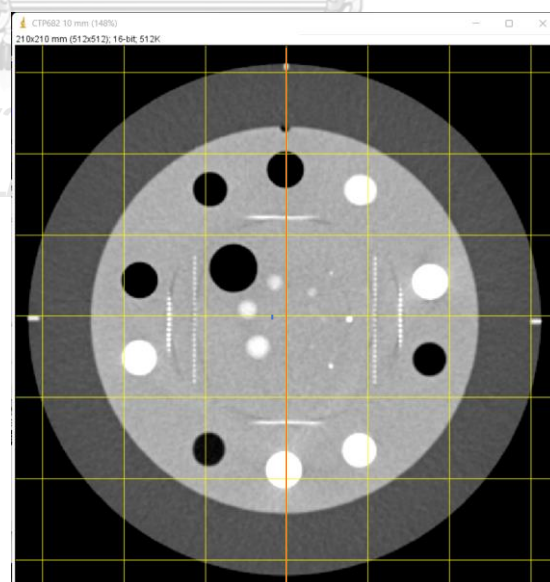


z-axis misalignment = 1.47 x 0.42= 0.285 mm

b) To determine x-axis misalignment, measure the distance (d) between center of the scanned field and center of the phantom in the x-direction. Multiply distance (d) by 0.42 to calculate x-axis misalignment.
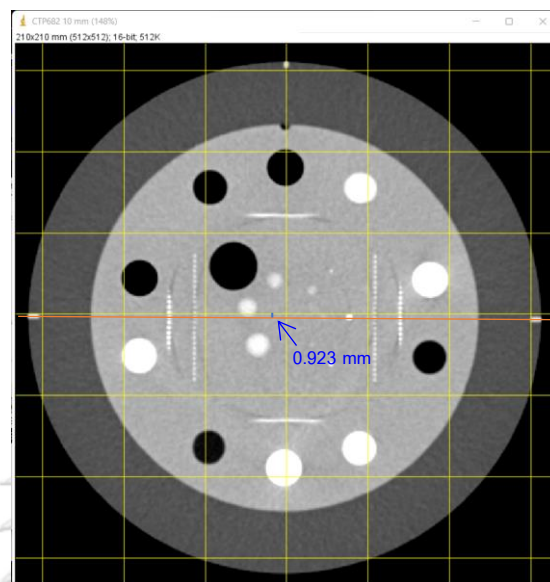


x-axis misalignment = 0.923 x 0.42= 0.387 mm

c) To determine y-axis misalignment, measure the distance (d) between center of the scanned field and center of the phantom in the y-direction. Multiply distance (d) by 0.42 to calculate x-axis misalignment.



y-axis misalignment = 0.0 x 0.42= 0.0 mm

Results:

| Test quantity | Test measurement | Acceptable | Test Result |
|---|---|---|---|
| z-axis misalignment | 0.285 mm | ± 5 mm | PASS |
| x-axis misalignment | 0.387 mm | ± 5 mm | PASS |
| y-axis misalignment | 0.0 mm | ± 5 mm | PASS |

## 2. Table Incrementation

The CT table incrementation accuracy test performed by scan the section and increment the table 30mm in and out of the gantry and scan again. The ramp centers should be the same on both images.



Table incrementation =
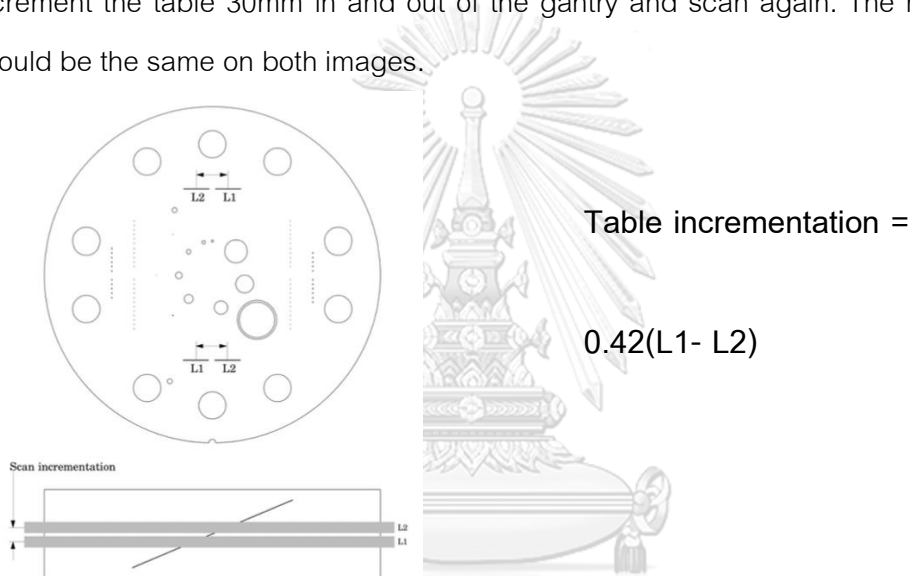
0.42(L1- L2)
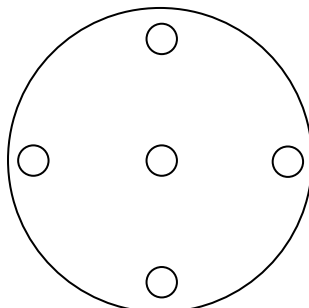
Result:

L1 = 12.1 mm          L2= 12.0 mm

Scan increment error = 0.42x |L1-L2| =0.42 x |L1-L2| = 0.042 mm

| Test quantity | Test measurement | Acceptable | Test Result |
|---|---|---|---|
| Table Increment error | 0.042 mm | ± 2 mm | PASS |

## 3. CT Number (HU) Accuracy

### a)    Water phantom



Water phantom (16 cm diameter) **(120 kVp, 350 mAs)**

Result :

| Test quantity | Test measurement | Acceptable | Test Result |
|---|---|---|---|
| Deviation of CT No. | | | |
| • Center | -1.5 HU | | |
| • 12 o'clock | -1.4 HU | ± 5 HU | PASS |
| • 3 o'clock | -1.5 HU | | |
| • 6 o'clock | -1.4 HU | | |
| • 9 o'clock | -1.9 HU | | |

*CT No. of water is 0.0 HU

### b) Catphan Phantom
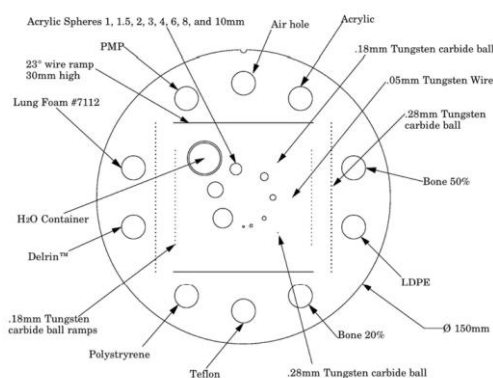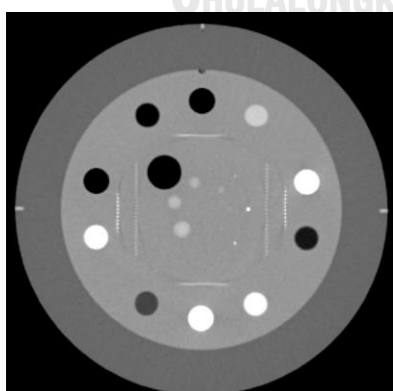


Catphan Phantom  **(120 kVp, 350 mAs)**

**Result :**

| Test quantity | Test measurement | HU range | | Test Result |
|---|---|---|---|---|
| CT No.of Material | | Min | Max | |
| • Air | -993.36 | -1046 | -986 | |
| • Acrylic | 121.86 | 92 | 137 | |
| • Bone 50% | 668.69 | 667 | 783 | |
| • LDPE | -95.27 | -121 | -87 | |
| • Bone 20% | 222.123 | 211 | 263 | PASS |
| • Teflon | 940 | 941 | 1060 | |
| • Polystyrene | -38.902 | -65 | -29 | |
| • Delrin | 344 | 344 | 387 | |
| • Lung Foam | -818.72 | -925 | -810 | |
| • PMP | -184.26 | -220 | -172 | |

## 4. Position Dependence of CT Numbers

Position the Catphan head phantom centered in the gantry.   Using 10 mm slice thickness , obtain one scan using typical head technique.   Select  a circular region  of interest of approximately 400  sq. mm. And record the mean CT number and standard deviation for each of the positions   1 through 5.
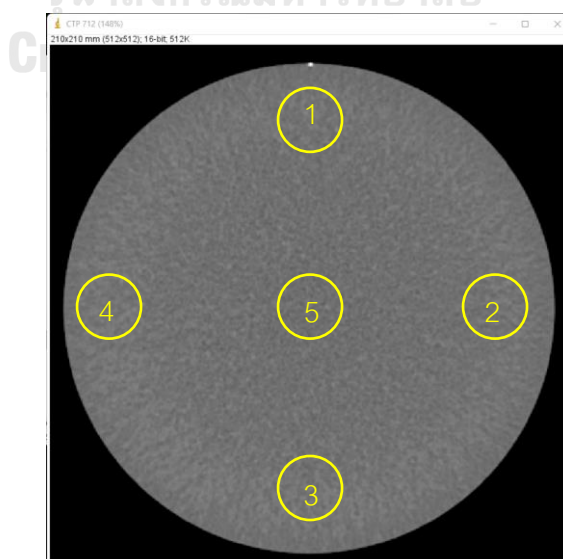
| Position | Mean CT No. (HU) | SD (HU) | CV |
|---|---|---|---|
| 1 | 17638.2 | 50.49 | 0.0029 |
| 2 | 17637.6 | 51.407 | 0.0029 |
| 3 | 17652.5 | 49.878 | 0.0028 |
| 4 | 17654.7 | 49.682 | 0.0028 |
| 5 | 17599.6 | 49.076 | 0.0028 |

The coefficient of variation should be less than 0.2.

Results: PASS

## 5. Low contrast resolution

To examine the low contrast resolution in CT image. Perform by using Catphan700 phantom at the foot end of the table following the instruction Perform  helical scan using typical head technique 120 kVp 300 mAs with 5 mm slice thickness. Select image at section CTP515 Low Contrast Module with Supra-slice and Subslice Contrast Targets. Adjust appropriate window and level for the best visualization of the test objects and zoom as necessary. Record the smallest test object visualized on the monitor.



Result:
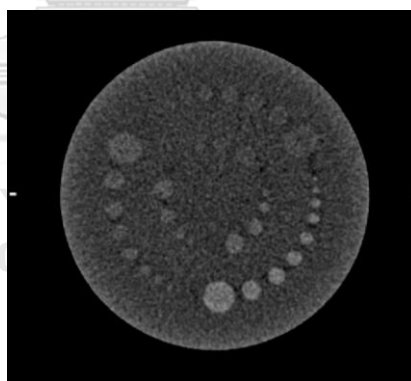
| Test quantity | | Acceptable | Test Result |
|---|---|---|---|
| Contrast | Smallest diameter | | |
| 1.0 % | 2 mm | | |
| 0.5 % | 3 mm | 4 mm* | PASS |
| 0.3 % | 5 mm | | |

*The diameter hole 4 mm or less (7 holes) should be seen at 0.5% contrast

# 6. High Contrast resolution

To examine the high contrast resolution in CT image. Perform by using Catphan700 phantom at the foot end of the table following the instruction Perform helical scan using typical head technique 120 kVp 300 mAs with 5 mm slice thickness. Select image at section CTP714 High Resolution Module with 1-30 line-pair/cm Gauges. Adjust appropriate window and level for the best visualization of the test objects and zoom as necessary. Record the smallest test object visualized on the monitor.
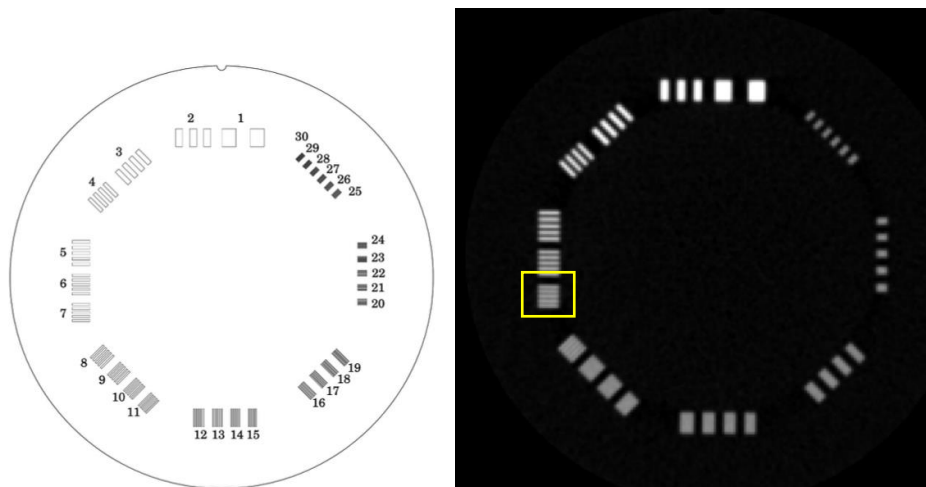


| Line Pair/cm | Gap Size | Line Pair/cm | Gap Size | Line Pair/cm | Gap Size |
|---|---|---|---|---|---|
| 1 | 0.500 cm | 11 | 0.045 cm | 21 | 0.024 cm |
| 2 | 0.250 cm | 12 | 0.042 cm | 22 | 0.023 cm |
| 3 | 0.167 cm | 13 | 0.038 cm | 23 | 0.022 cm |
| 4 | 0.125 cm | 14 | 0.036 cm | 24 | 0.021 cm |
| 5 | 0.100 cm | 15 | 0.033 cm | 25 | 0.020 cm |
| 6 | 0.083 cm | 16 | 0.031 cm | 26 | 0.019 cm |
| 7 | 0.071 cm | 17 | 0.029 cm | 27 | 0.0185 cm |
| 8 | 0.063 cm | 18 | 0.028 cm | 28 | 0.0178 cm |
| 9 | 0.056 cm | 19 | 0.026 cm | 29 | 0.0172 cm |
| 10 | 0.050 cm | 20 | 0.025 cm | 30 | 0.0167 cm |

Results :

| Test quantity | Test measurement | Acceptable | Test Result |
|---|---|---|---|
| Spatial resolution | 7 lp/cm | 5 lp/cm | PASS |

## 7. Reconstruction Slice thickness

To verify accuracy of slice thickness and post patient collimator which process from image reconstruction. This test use Catphan700 phantom at the foot end of the table following the instruction; perform helical scan using typical head technique with different reconstruction slice thickness under the same parameters.

**Analysis:**

Select image at section CTP682 Geometry and Sensitometry Module to calculate the actual reconstructed slice width as following:

i. Draw ROI to identify mean CT number of the area adjacent to the wire ramp for define as "Background"

ii. Adjust window width to 1

iii. Move window level to the point where the wire ramp disappears.

iv. Determine window level at this position is "Maximum value"

v. Define the half maximum CT by:

    a) Net peak CT = Maximum value – Background

    b) 50% Net peak CT = Net peak CT/2

    c) Half maximum CT = 50% Net peak CT + Background

vi. Adjust window level to be equal at half maximum CT

vii. Draw line along the ramp that show length of each ramp

viii. Average length of 4 wire ramp as FWHM.

ix. Slice width = FWHM x 0.42 mm

**Results :**

| Recon. Slice Thickness | Measured Slice Thickness | Deviation | Acceptable | Test Result |
|---|---|---|---|---|
| 1 mm | 1.32 mm | 0.32 mm | ±0.5 mm | PASS |
| 2 mm | 2.39 mm | 0.39 mm | ±1.0 mm | PASS |
| 3 mm | 3.36 mm | 0.36 mm | ±1.0 mm | PASS |
| 5 mm | 4.89 mm | -0.11 mm | ±1.0 mm | PASS |
| 10 mm | 10.19 mm | 0.19 mm | ±1.0 mm | PASS |

## 8. Radiation dose

Volumetric computed tomography dose index: $CTDI_{vol}$ measurement in PMMA phantom. This measurement was carried out to verify the displayed $CTDI_{vol}$ (mGy) values versus the measure values.

Technique : 120 kVp    mA 300                              Rotation time 1.0 sec

Collimation:  57.6 mm (96*0.6 mm)                         SFOV 250 mm

| Position | Measured $CTDI_{100}$ (mGy) | |
|----------|------------------------------|--|
| Center | $CTDI_{100,c}$= 36.75 mGy | |
| 12 o'clock | 36.28 | |
| 3 o'clock | 42.93 | $CTDI_{100,p}$ = |
| 6 o'clock | 40.16 | 40.185 mGy |
| 9o'clock | 41.37 | |

*Calculation of $CTDI_{vol}$ (mGy)*

$$CTDI_w = \frac{1}{3}CTDI_{100,C} + \frac{2}{3}CTDI_{100,periphery} \text{ mGy}$$

$$CTDI_w = \frac{1}{3}36.75 + \frac{2}{3}40.185 \text{ mGy}$$

$$CTDI_w = 39.04 \text{ mGy}$$

$$CTDI_{vol} = 39.04/1 = 39.04 \text{ mGy}$$

Result:

| Measured $CTDI_{vol}$ (mGy) | Displayed $CTDI_{vol}$ (mGy) | % Difference | Acceptable | Test Result |
|-----------------------------|------------------------------|--------------|------------|-------------|
| 39.04 | 42.47 | 8.08% | ±20% | PASS |

# REFERENCES

VITA

NAME                    Hataipat  Jantawong

DATE OF BIRTH           07 June 1982

PLACE OF BIRTH          Nakhon Pathom

INSTITUTIONS ATTENDED   Medical Physics Program, Department of Radiology, Faculty
                        of Medicine, Chulalongkorn University

HOME ADDRESS            842/196 Rama 9 Soi 2 , Bangkapi, Hauy Kwang, Bangkok,
                        10310

AWARD RECEIVED          Best Oral Presentation Award in  the 3rd PIT-FMB and the
                        17th SEACOMP, Indonesia

จุฬาลงกรณ์มหาวิทยาลัย
CHULALONGKORN UNIVERSITY